UNIVERSITY OF TURIN

Department of Clinical and Biological Sciences

Doctoral School of Life and Health Sciences

PhD in Experimental Medicine and Therapy

Cycle XXXVIII

Immuno-metabolic modulation in cancer cachexia: novel therapeutic strategies to fight an old enemy

Supervisor:

Prof. Paola Costelli

PhD Student:

Giacomo Rubini

Co-Supervisor:

Prof. Fabio Penna

PhD Coordinator:

Prof. Pasquale Pagliaro

2022 – 2025

MED/04

TABLE OF CONTENTS

1. ABSTRACT

Background: Cancer cachexia is a complex syndrome characterized by body weight loss and muscle wasting. It affects 50-80% of cancer patients, significantly reducing quality of life, anticancer treatment tolerance and efficacy, and survival rates, yet it lacks effective treatments. Multiple mechanisms are involved, including systemic inflammation, mitochondrial dysfunction, metabolic alterations, immune dysregulation, and oxidative stress. Previous studies showed that interleukin-4 (IL4) administration to tumor-bearing (TB) mice improves muscle mass and function, myogenesis, and survival. Additionally, IL4 and IL4 receptor are upregulated in the skeletal muscle in response to exercise.

Objective: This study aimed to investigate the effects of IL4 on skeletal muscle and systemic metabolism, as well as its impact on the immune response in TB animals.

Methods: C26 TB male mice were treated daily with IL4 by intraperitoneal injection. Muscle strength was assessed by grip strength test. The plasma was used to assess circulating cytokine and chemokine levels by bead-based multiplex assays. Immunophenotype analysis on isolated splenocytes was performed by flow cytometry. The tumor was analyzed by single nuclei RNA sequencing. The skeletal muscle was used to assess hexokinase II activity, mitochondrial proteins (western blotting) and respiration (high-resolution respirometry). Metabolomic and lipidomic analyses were performed on skeletal muscle and liver. Subsequently, C26 TB male mice were treated daily with febuxostat (FBX) by oral gavage. The skeletal muscle was used to assess *ex vivo* contractility and markers of inflammation, proteostasis and mitochondrial homeostasis (western blotting).

Results: IL4 treatment counteracted the loss of body weight, muscle mass and strength in the C26 TB mice. Cancer-induced dysregulations in the circulating cytokine and chemokine profile were corrected as well, including a partial reduction towards control levels of IL6 and TNFα. In addition, IL4 improved the immune response in the C26 hosts, significantly counteracting cancer-induced systemic immunosuppression. Conversely, IL4 promoted an immunosuppressive tumor microenvironment (TME), increasing the proportion of M2 macrophages and malignant cells, despite comparable gross tumor mass between treated and untreated mice. As for the skeletal muscle, IL4 treatment in the C26 hosts improved energy metabolism, as shown by the improved hexokinase II activity, mitochondrial homeostasis and

respiration. This was confirmed by metabolomic and lipidomic analyses, thereby demonstrating a broad metabolic rescue induced by IL4 involving several pathways and lipid classes in both skeletal muscle and liver. Interestingly, IL4 failed to prevent C26-induced uric acid elevation in the skeletal muscle, a typical trait of xanthine oxidase-dependent oxidative stress. However, xanthine oxidase inhibition via FBX failed to prevent C26-induced body weight loss or muscle wasting. In the skeletal muscle of the C26 hosts, while favorably modulating the inflammatory and proteostasis signaling, FBX treatment significantly exacerbated cancer-induced mitochondrial alterations.

Conclusion: Treatment with IL4 improves the immune response, while mimicking the effects of exercise by improving muscle-specific and systemic metabolism in the C26 TB mice. Collectively, these results demonstrate that IL4 is an immuno-metabolic modulator that successfully counteracts cancer cachexia. The inability of FBX to prevent cachexia by targeting a single pathway further supports the potential of the pleiotropic activity of IL4. While the effects of IL4 on the TME warrant caution, the results presented in this work demonstrate the potential of this cytokine for the treatment of cancer cachexia, likely in combination with anticancer drugs.

2. INTRODUCTION

2.1. The skeletal muscle

Muscle tissue can be subdivided in three main groups: smooth, cardiac, and skeletal muscle. The skeletal muscle is responsible for voluntary movement and accounts for up to 40% of the total body mass. The skeletal muscle serves to the body several functions, ranging from mechanics to metabolism. From the mechanical point of view, this tissue generates force, and is fundamental for the movement of the body[1,2]. The skeletal muscle also has a critical role in terms of whole-body energy metabolism. Specifically, it produces heat, which is fundamental for the body to maintain its thermostasis. It is also one of the main tissues responsible for glucose uptake and storage, as well as being a reservoir of amino acids. While being a site where several metabolites are stored, it also consumes them, together with oxygen, during muscle contraction for energy production, such as during physical activity[3]. However, the mobilization of functional metabolites can also occur during starvation, in order to maintain the correct blood glucose levels and fuel other vital organs, such as the heart and the brain[1,2]. Overall, the skeletal muscle has a central role in the regulation of systemic metabolism and homeostasis in the organism. Hence, the preservation of its mass and function is fundamental for preserving health, quality of life, and preventing disease[1,2].

2.1.1. Structure and function of the skeletal muscle

The skeletal muscle structure follows a specific hierarchical organization. The entire muscle is surrounded by a connective tissue sheath called epimysium. The epimysium encloses many muscle fascicles, which are in turn surrounded by a connective tissue layer called perimysium. Each muscle fascicle is composed of many muscle cells, also known as myofibers. Each muscle fiber is surrounded by another layer of connective tissue, the endomysium, where blood capillaries, nerves and proprioceptors are located. Myofibers are the largest cells in the body and are multinucleated, reaching up to 100-200 nuclei in each cell[4]. The cell membrane of myofibers is called sarcolemma, and it plays a central role in the muscle functionality of the whole tissue. In fact, the sarcolemma contains the dystrophin complex, a protein complex that connects the extracellular matrix to the internal myofilament structure. The connection of the sarcolemma to the extracellular matrix is fundamental for achieving muscle contraction, as it conducts the energy of all the working myofibers[5]. Each myofiber contains numerous repeating

units called sarcomeres. Sarcomeres are arranged in a striated pattern of protein filaments (myofilaments), and constitute the basic contractile units of the skeletal muscle[1,2]. The two main myofilaments are actin (thin filament) and myosin (thick filament). These two protein filaments run parallel to the myofiber axis and are essential components of the contraction machinery[1,2] (Figure 1).

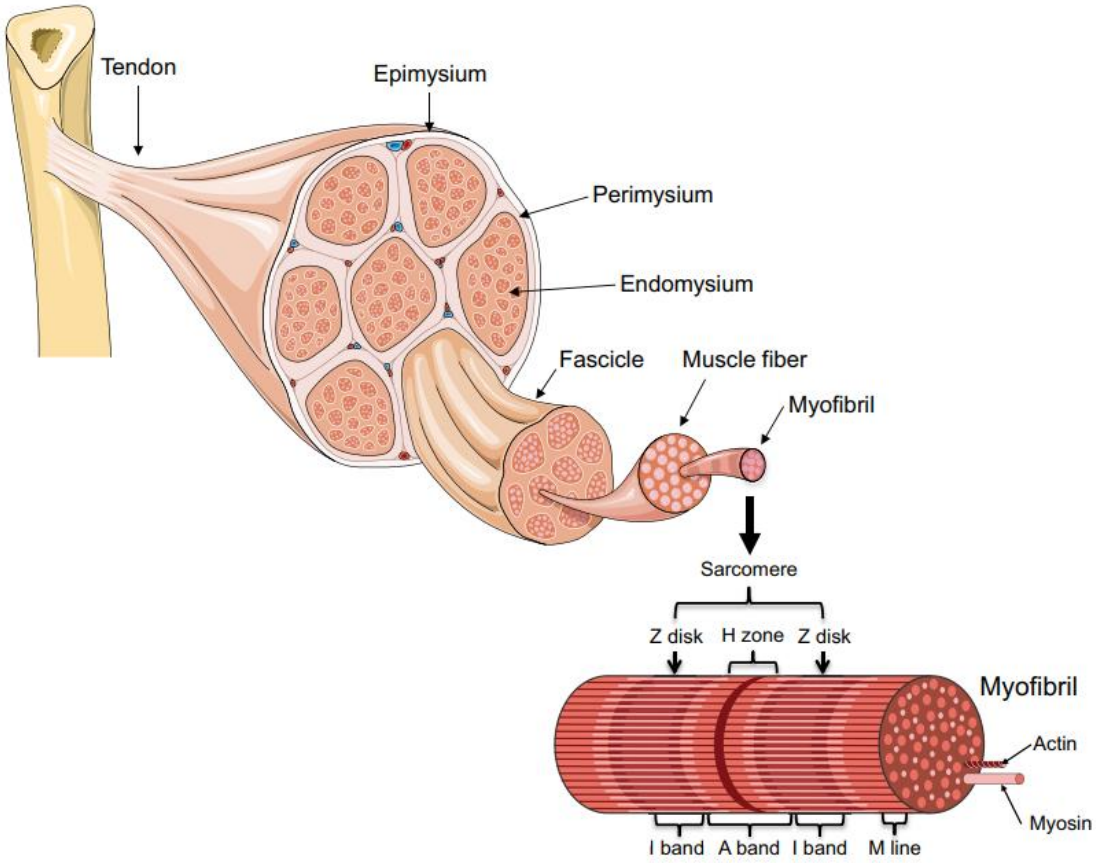

Figure 1. Structure of the skeletal muscle[6].

The skeletal muscle contraction is initiated by an increase in cytosolic calcium concentration. This increase in cytosolic calcium depends on the calcium release by the sarcoplasmic reticulum through the ryanodine receptors, a process controlled by the central nervous system. In fact, muscle contraction is activated by motoneurons, somatic efferent neurons that are intimately associated with the sarcolemma at specialized regions called neuromuscular junctions (NMJ). Each motoneuron, together with the specific myofibers that it innervates, defines the motor unit. When the motoneuron is activated by the central nervous system, it releases acetylcholine into the NMJ. This neurotransmitter travels from the motoneuron, across the synaptic space, to the

myofiber membrane, where it binds specific receptors, triggering the release of calcium[7] (Figure 2).

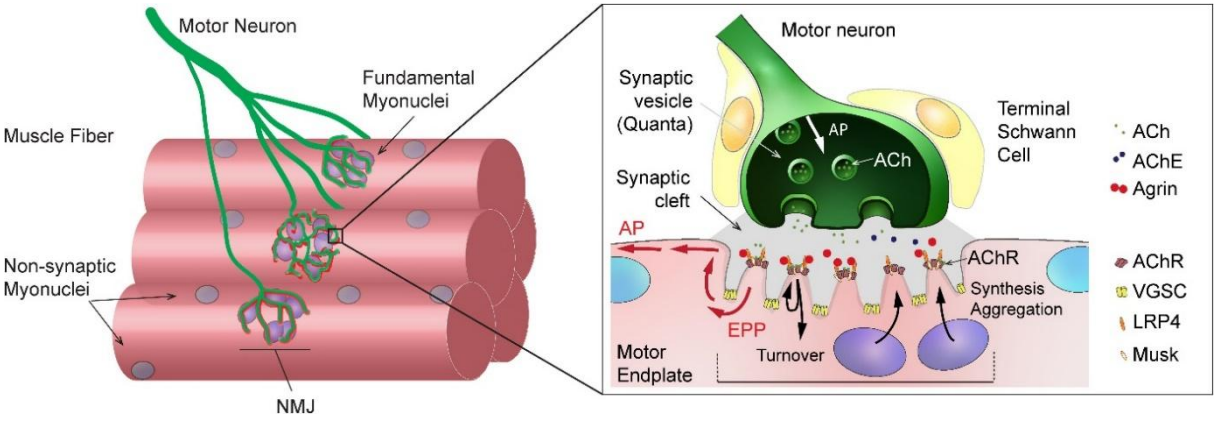

Figure 2. Representation of the motor unit and the neuromuscular junction[8].

In the myofiber, the released cytosolic calcium binds troponin C. This binding leads to a positional shift of the troponin complex on the actin myofilaments, which in turn expose the myosin binding sites. Myosin, bound by ADP and inorganic phosphate, interacts with actin. The release of ADP and inorganic phosphate produces a power stroke, by which actin filaments slide past myosin filaments. The resulting shortening of the muscle represents contraction. Subsequently, the binding of ATP to myosin determines the release of myosin from actin. Finally, myosin hydrolyzes ATP so that the contraction process can be repeated[9] (Figure 3).

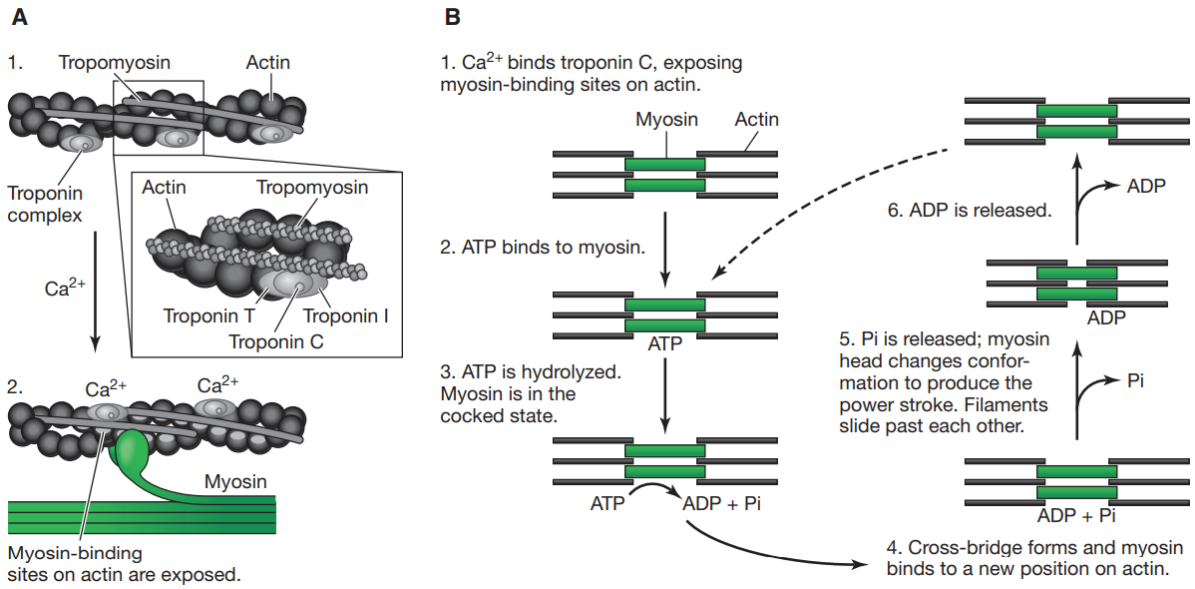

Figure 3. Detailed representation of myosin-actin interaction (*A*) and of the contraction cycle (*B*)[9].

Myofibers of the same muscle are closely associated, but can display distinct morphological and molecular features. Specific traits change depending on the type of contractile function performed. Adult mammalian skeletal muscle can express different types of myosin heavy chain: a slow isoform (MHC-I) and three fast isoforms (MHC-IIA, -IIX, and -IIB). Depending on the MHC isoform they express, myofibers are in turn classified as type I, IIA, IIX, and IIB, all having unique molecular and metabolic features[10]. The specific molecular and metabolic traits confer specific functional competences to each myofiber type. In particular, type I myofibers are highly resistant to fatigue, while type IIB myofibers are specialized for short activities demanding a high peak force.

In a muscle, the relative proportion of myofiber types depends on the species and the anatomical site[11]. These different myofiber types possess distinct structural and metabolic adaptations, which are driven by the activation of different signaling pathways that initiate specific genetic programs. Overall, this implies that the basal molecular scenario differs among myofiber types. This underlying diversity makes each myofiber type behave differently to external stimuli and renders them differentially susceptible to specific pathologies[12] (Figure 4).

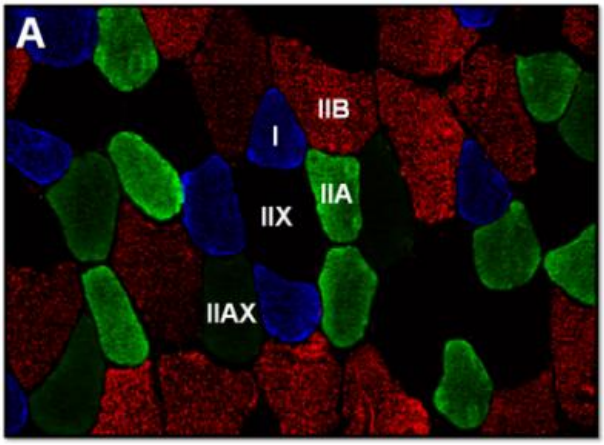

Figure 4. Immunostaining of different MHC isoforms, highlighting different myofiber types in rat tibialis anterior muscle[10].

2.1.2. Skeletal muscle metabolism

The process of muscle contraction requires the release of energy derived from the breakdown of ATP to ADP and inorganic phosphate. Briefly, these include membrane excitability, sarcoplasmic reticulum calcium handling, and myofilament cross-bridge cycling, all processes associated with ATPase activity. However, the skeletal muscle is able to store relatively small amounts of ATP (5-8 mmol/kg wet muscle), which are insufficient to support extended periods of contractile activity. This represents a critical challenge that muscle cells face by using other mechanisms to produce ATP at a rate that matches the demand[13–15]. To meet this challenge, the skeletal muscle has a unique capacity to rapidly adjust its metabolic rate in response to the energetic needs[3,15]. The main metabolic pathways that replenish ATP are glycolysis (carbohydrate catabolism) and β-oxidation (lipid catabolism), which produce pyruvate and/or acetyl-CoA. When oxygen is present, these intermediates are further processed through the tricarboxylic acid (TCA) cycle in the mitochondria, producing NADH, H^+, and CO_2. These products are then used by the mitochondrial electron transport chain (ETC), that produces ATP through oxidative phosphorylation (OXPHOS), a process also known as mitochondrial respiration[15]. The fact that glycolytic byproducts, including pyruvate and NADH, enter the mitochondria and fuel mitochondrial respiration, underlines a close connection between these two metabolic pathways. However, they significantly differ in their substrates, oxygen requirements, ATP production capacity, and contribution to fatigue. Briefly, glycolysis is a series of ten enzymatic reactions that occur in the cytoplasm. It starts with the phosphorylation

of glucose by hexokinase, that catalyzes the first committed step of glucose catabolism, and ends with the production of pyruvate, alongside ATP and NADH. Glucose breakdown via glycolysis represents the fastest pathway to restore the ATP reservoir of the cell, and it's able to respond immediately to energy demands, without requiring oxygen. By contrast, mitochondrial respiration is an oxygen-dependent process that resynthesizes ATP to meet elevated and sustained energy demands that can occur during activities such as endurance exercise[13,15,16]. Beyond processing carbohydrates and lipids, the skeletal muscle also provides a crucial protein reserve of amino acids, which can be catabolized as a last resort during energy shortfalls or starvation[3]. In skeletal muscle pathophysiology, several disorders are associated with metabolic alterations. These latter can be caused indirectly by disease-induced anorexia, or directly by disease-related metabolic dysregulations, as occurring during muscular dystrophies, sarcopenia and cancer cachexia[3,14]. Preserving skeletal muscle mass during illness is therefore critical, both for regulating inter-organ metabolism and for providing a mobilizable protein reserve that can be used for energy production[3,15].

2.1.3. Mitochondria in the skeletal muscle

Mitochondria are the double-membrane organelles of eukaryotic cells that serve as the primary site of cellular energy production. In other words, mitochondria are the powerhouse of the cell. They produce energy in the form of ATP, in a process that consumes oxygen and several metabolic substrates, while producing reactive oxygen species (ROS). Their functional role, however, extends well beyond ATP production and includes calcium homeostasis, thermogenesis, intracellular signal transduction, oxidative stress management, and apoptosis[17]. Mitochondria are characterized by their highly dynamic nature, showing significant plasticity when responding to both physiological and pathological stresses, such as exercise, disuse, aging, and disease[18,19]. More in detail, to meet fluctuating energy demands and adapt their morphology to the cellular environment, mitochondria can continuously modulate their function, structure, and volume. This modulation occurs through four key processes that collectively represent mitochondrial dynamics: biogenesis, fission, fusion, and autophagy (or mitophagy)[17–19]. For instance, endurance exercise training can induce an increase in mitochondrial biogenesis, which leads to increased mitochondrial content. By contrast, a decline in mitochondrial content and oxidative metabolism is frequently occurring during aging, obesity and diabetes[18]. In physiological conditions and in the absence of stressor stimuli,

instead, the mitochondrial content in the cell is stable. This mitochondrial content stability, a crucial aspect of mitochondrial homeostasis, is achieved thanks to a strictly regulated quality control system that finely tunes and balances the rates of mitochondrial biogenesis and disposal[17–19].

As previously mentioned, a central function of mitochondria is to produce energy for the cell in the form of ATP, a process that involves the electron transport chain (ETC). Specifically, the ETC consists of four protein complexes (I-IV) that are found embedded in the inner mitochondrial membrane (IMM). These protein complexes receive electrons from the TCA-derived NADH and $FADH_2$. The electrons then move sequentially through the ETC reaching complex IV, where oxygen is used as the final electron acceptor. The movement of the electrons through the ETC, which follows a gradient of increasing reduction potential, releases energy that determines the translocation of hydrogen ions (H^+) from the mitochondrial matrix to the intermembrane space. This proton gradient across the IMM determines an electrochemical gradient and a membrane potential, collectively known as the proton motive force. This force is then used by complex V for the production of ATP. Specifically, complex V, or ATP synthase, uses the movement of protons back to the mitochondrial matrix to convert ADP and inorganic phosphate to ATP, as the final step of the process collectively named oxidative phosphorylation (OXPHOS)[17,20] (Figure 5).

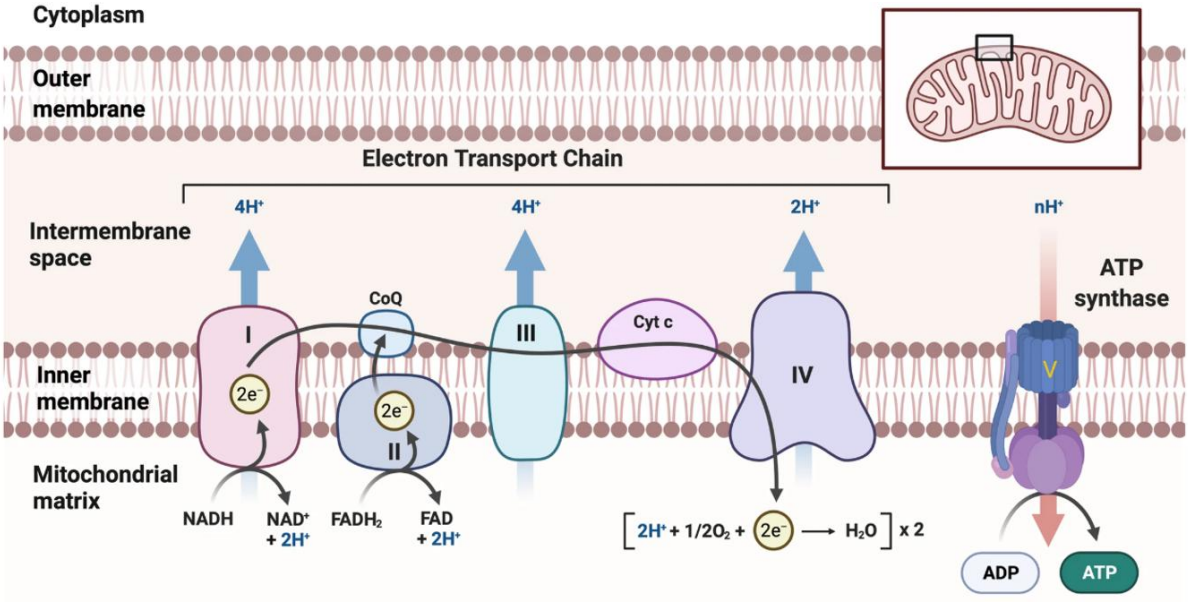

Figure 5. Schematic representation of mitochondrial oxidative phosphorylation (modified)[21].

Mitochondrial health is strictly related to the correct functionality of the processes associated with mitochondrial homeostasis. In this context, the peroxisome proliferator-activated receptor-gamma coactivator 1 alpha (PGC-1α) plays a central role. PGC-1α is a coactivator of peroxisome proliferator-activated receptor (PPAR) gamma, a member of the of the PPAR family of nuclear receptors critical for the regulation of muscle energy homeostasis, energy metabolism, and, importantly, mitochondrial biogenesis and function. Specifically, PGC-1α is a highly inducible and ubiquitous transcriptional coregulator that regulates cellular energy metabolism, and mitochondrial biogenesis and function, hence representing a central player in mitochondrial homeostasis[18,22,23]. Along this line, it is essential for adaptation to aerobic (endurance) exercise, as it promotes muscle remodeling towards a more oxidative fiber-type, angiogenesis, overall enhancing fatigue resistance. PGC-1α also plays an important metabolic role, as it is involved in the regulation of lipid and carbohydrate metabolism. Accordingly, its transcription is induced during states requiring substrate mobilization and energy production, including caloric restriction and physical exercise[22]. Conversely, the loss of PGC-1α leads to reduced expression of ETC- and OXPHOS-related genes, thus reduced mitochondrial respiration and impaired exercise performance[17]. Altogether, correct PGC-1α functioning and, in general, the maintenance of mitochondrial homeostasis are fundamental aspects of skeletal muscle pathophysiology. Parallelly to biogenesis, the preservation of mitochondrial health relies on several processes, including fission, fusion, and mitophagy[24]. Of these, fission and fusion, collectively termed mitochondrial dynamics, are key players in mitochondrial quality control[25]. For these processes, several proteins located on the inner and outer mitochondrial membranes (OMM and IMM) are involved. Key mediators of mitochondrial fusion are Mitofusin (Mfn) 1 and 2, located on the OMM, and optic atrophy 1 (OPA1), located on the IMM. The process of mitochondrial fission, instead, involves mitochondrial fission 1 protein (Fis1), dynamin-related protein 1 (Drp1), mitochondrial fission factor (Mff), and mitochondrial dynamic proteins 49 and 51[24,26] (Figure 6).

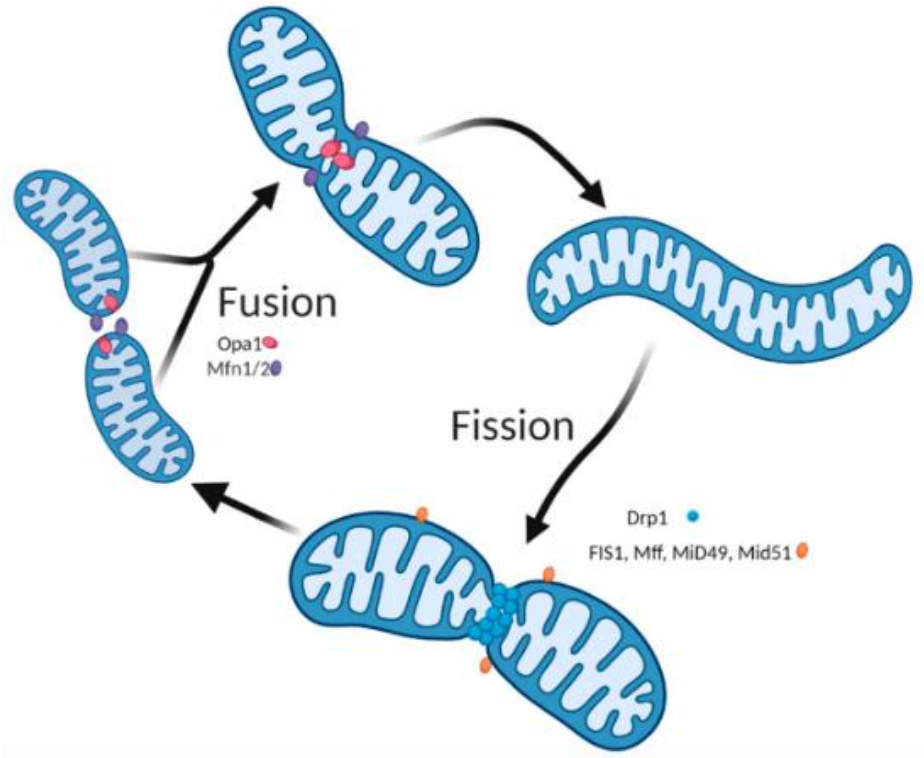

Figure 6. Schematic representation of mitochondrial fusion and fission[24].

A parallel and fundamental mechanism for regulating mitochondrial quality and quantity is mitophagy. The balance between mitochondrial biogenesis and disposal is necessary for mitochondrial health[25]. Mitophagy is a selective form of autophagy, specifically responsible for removing excessive or dysfunctional mitochondria. It is a highly conserved, genetically programmed process in mammalian cells[19,24,26]. Briefly, the process involves sequestering the targeted mitochondria within autophagosomes, double-membrane structures that then fuse with lysosomes degrading their content[19,26]. Two distinct pathways are involved in mitophagy. The first is the PINK1/Parkin-mediated pathway. This pathway begins with the loss of mitochondrial membrane potential, which causes PINK1 (PTEN-induced kinase 1) to accumulate on the OMM, and consequently to its activation by phosphorylation. Activated PINK1 then recruits and activates the E3 ubiquitin ligase Parkin. Subsequently, Parkin ubiquitinates OMM proteins, which attracts p62 to the ubiquitin chains. Then, p62 binds to microtubule-associated protein 1A/1B-light chain 3 (LC3) lipidated and active form (LC3-II) on the autophagosome. This binding allows the targeted mitochondria to be enclosed in the autophagosome. The process ends with the degradation of the autophagosome content following to fusion with lysosomes[19,24] (Figure 7).

As mentioned above, mitophagy can also be driven by another pathway, which involves BCL2 interacting protein 3 (BNIP3)[24]. Normally, BNIP3 is present in the cytosol as an inactive monomer. In response to stress signals, BNIP3 is upregulated, and anchors to the OMM forming a homodimer[19,26]. In the homodimerized form, BNIP3 can interact with LC3-II[19] (Figure 7).

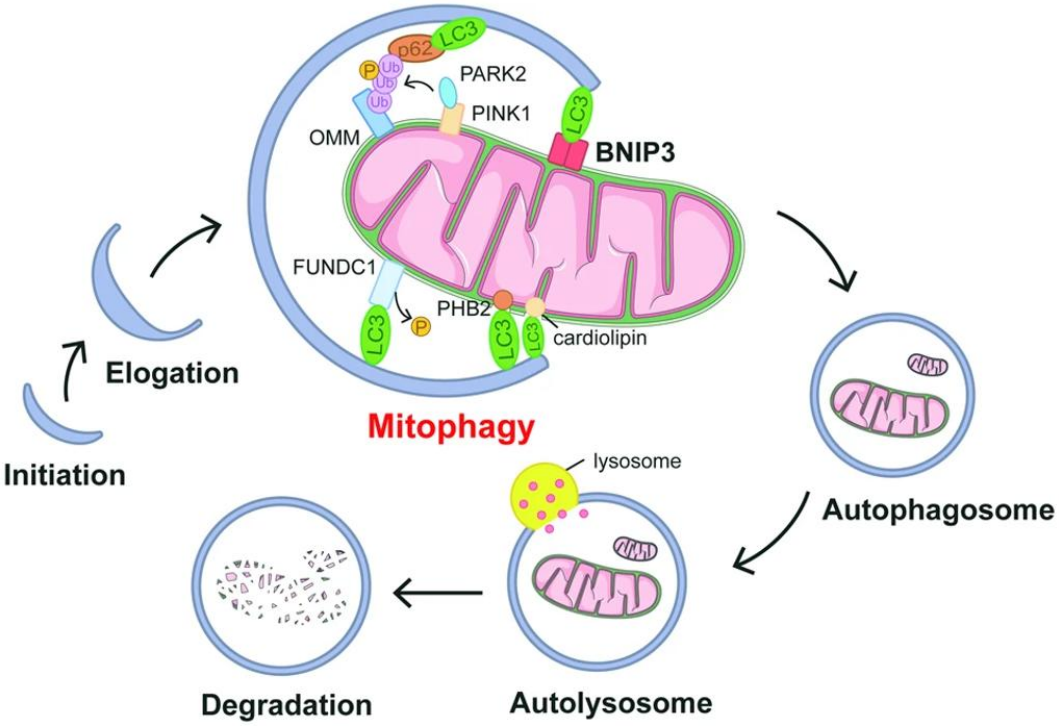

Figure 7. Schematic representation of mitophagy (modified)[27].

Overall, mitochondria are dynamic organelles able to respond to physiological and pathological stimuli by remodeling and modulating their content. Correct quality and quantity are fundamental for the execution of their function, and are achieved by the correct tuning of mitochondrial biogenesis, fusion, fission, and mitophagy, whose balance is fundamental for mitochondrial homeostasis and health (Figure 8).

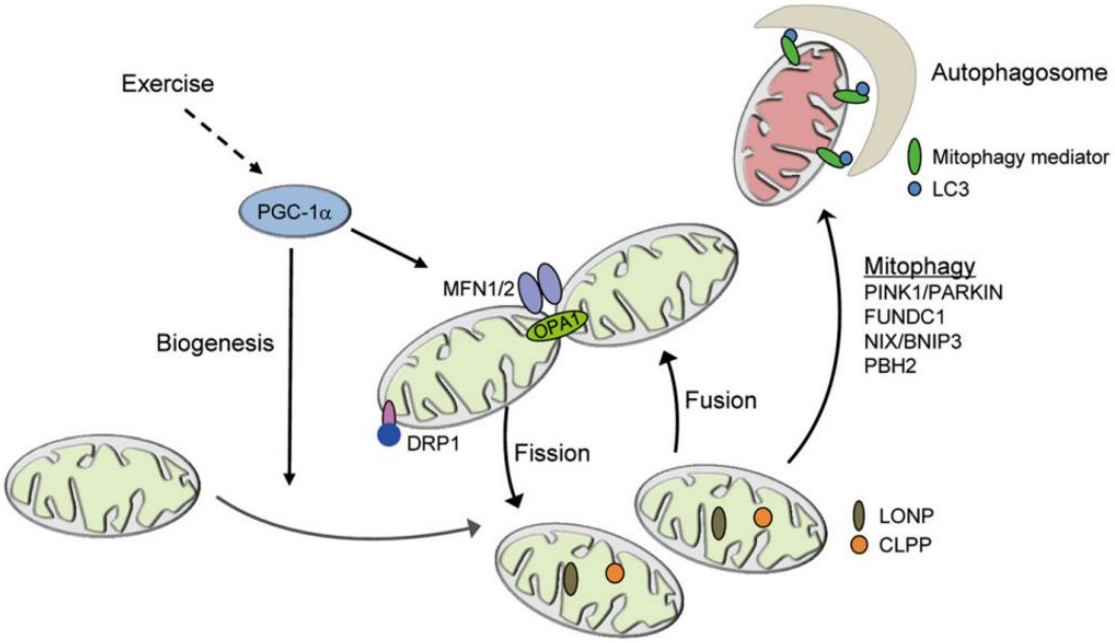

Figure 8. Overview of mitochondrial homeostasis (modified)[18].

2.2. Cancer cachexia

Cancer cachexia is a complex multifactorial syndrome characterized by involuntary loss of body weight and skeletal muscle, with or without fat mass depletion[28,29]. It affects 50-80% of cancer patients, leading to reduced quality of life, tolerance to anticancer treatments, and is directly responsible for up to 30% of cancer deaths[30–32]. Despite its clear relevance for the clinical settings, effective therapies are not available, depicting cancer cachexia as an unmet medical need[29]. The lack of effective treatments partially depends on the difficulty in finding a consensus on the definition and diagnosis of this syndrome. Only in recent times, cancer cachexia was defined as a "complex metabolic syndrome associated with an underlying illness and characterized by loss of muscle with or without loss of fat mass. Anorexia, inflammation, insulin resistance and increased muscle protein breakdown are frequently associated with wasting disease"[33]. Three progressive phases of cancer cachexia were recognized: pre-cachexia, cachexia and refractory cachexia. Early diagnosis is critical, and is based on the identification of 5% of body weight loss in the previous 12 months, alongside fatigue, decreased muscle strength, anorexia and abnormal biochemistry[33,34]. As patients progress through these phases, a process that depends on several extrinsic and intrinsic factors, treatment efficacy and survival

dramatically drop[33]. The scenario is further complicated by anticancer treatment toxicity, that can significantly contribute to the severity of cachexia[30] (Figure 9).

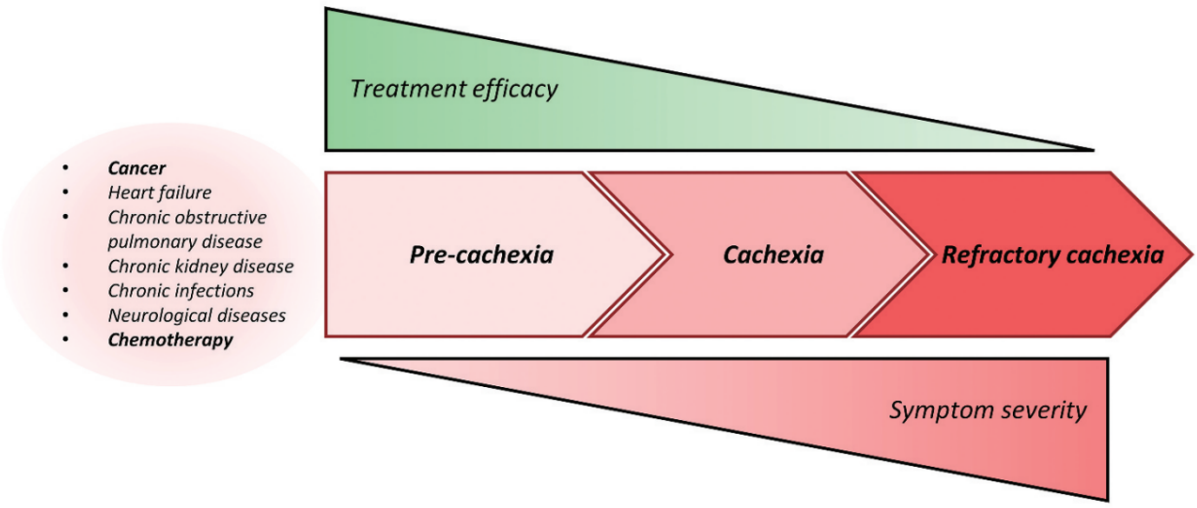

Figure 9. Cachexia progression in relationship with treatment efficacy and symptom severity (modified)[29].

2.2.1. Pathogenetic mechanisms of cancer cachexia

Multiple mechanisms are involved in the pathogenesis of cancer cachexia, including systemic inflammation, tissue-specific and systemic metabolic alterations, mitochondrial dysfunction, oxidative stress, and immune dysregulation[30,35–37].

Systemic inflammation

Cancer cachexia is characterized by chronic and systemic inflammation, which is driven by pro-inflammatory cytokines and other mediators, derived from both the tumor and the host. The abnormal levels of these factors are central to the pathogenesis of cachexia, and lead to molecular alterations that result in altered metabolism, protein and lipid degradation, and, overall, body wasting[28,38–40]. Pro-inflammatory mediators can activate the JAK/STAT3 pathway, which increases myostatin transcription and in turn SMAD2 and SMAD3 activation. This results in an increase of protein degradation paralleled by reduced synthesis, as well as

oxidative stress[40]. The activation of signaling pathways dependent on NF-kB and p38 mitogen-activated protein kinases (p38 MAPK) is another effect of pro-inflammatory cytokines, which further promotes protein degradation via the ubiquitin-proteasome system (UPS). In this context, also lysosomal-autophagic proteolysis is enhanced, adding to the exacerbation of protein catabolism and muscle wasting[28,40]. Additionally, many solid tumors, as well as lytic bone metastases, lead to increased circulating transforming growth factor-β (TGFβ). In the skeletal muscle, TGFβ-dependent signaling results in aberrant calcium leak from the sarcoplasmic reticulum, determining muscle weakness (Figure 10). The addition of muscle weakness to the ongoing muscle wasting further exacerbates the overall muscle dysfunction associated with cachexia[28].

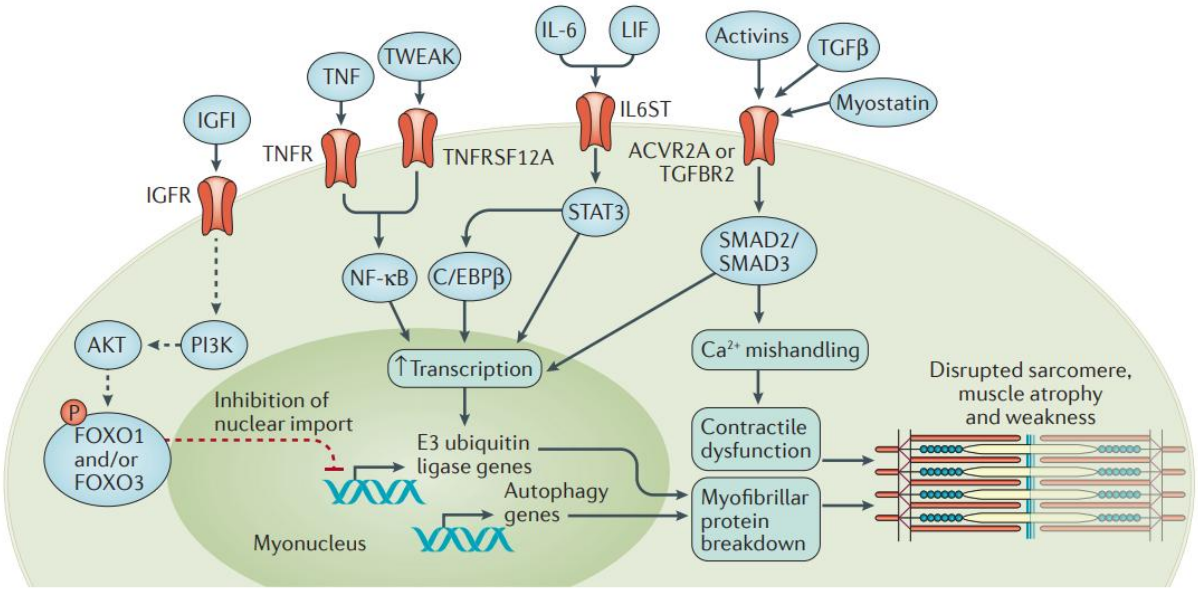

Figure 10. Mediators and signaling pathways involved in cancer-induced skeletal muscle wasting[28].

Reduced food intake, a central feature of cancer cachexia, is strongly linked to systemic inflammation. Specifically, pro-inflammatory stimuli acting on the hypothalamus can trigger anorexigenic (appetite-suppressing) while simultaneously inhibiting orexigenic (appetite-stimulant) pathways. This leads to a decreased production of neuropeptide Y, ultimately resulting in anorexia[28,39]. Importantly, in cancer patients with cachexia this process promoting anorexia can be further exacerbated by anticancer treatments and physical inactivity[39].

Beyond protein degradation and muscle wasting, pro-inflammatory mediators also cause the depletion of adipose tissue, that occurs as a consequence of the enhancement of lipolysis and the inhibition of lipogenesis. Adipose tissue loss is relevant, as it is thought to precede and predispose cancer patients to muscle wasting[28]. Triglyceride degradation in adipocytes, in fact, is hypothesized to occur before protein degradation in the skeletal muscle as it could be directly responsible for signaling the activation of proteolysis. During systemic inflammation, white adipose tissue loss can also be amplified by the upregulation of uncoupling protein (UCP) 1, which in turn increases lipid mobilization and energy expenditure[39].

Metabolic alterations

Cancer cachexia is characterized by a negative energy balance, a state that results in the depletion of body stores and that is caused by the simultaneous occurrence of multiple factors: reduced energy intake (anorexia and malabsorption), increased resting energy expenditure (REE), and tumor-host metabolic competition[28,41]. One of the main causes of REE elevation in cachexia is the upregulation of UCPs in the skeletal muscle and adipose tissue, leading to the dissipation of energy as heat. This process is closely linked to inflammation, as UCPs are induced by pro-inflammatory cytokines, including IL6 and TNFα[40,41]. Energetic inefficiency can also arise from ATP mismanagement. Specifically, on one side ATPases, such as sarcoplasmic reticulum calcium ATPase, can produce heat by uncoupling ATP hydrolysis. In parallel, ATP synthesis by skeletal muscle mitochondria can be impaired due to proton leakage from the IMM. Additionally, alterations in protein, carbohydrate and lipid metabolism can establish futile cycles, in which ATP is used with no net metabolic gain and producing heat, overall representing a source of metabolic inefficiency and increasing the REE. Futile cycles can also be a consequence of tumor metabolism, as seen in the Cori cycle, featuring tumor-host lactate recycling[41] (Figure 11).

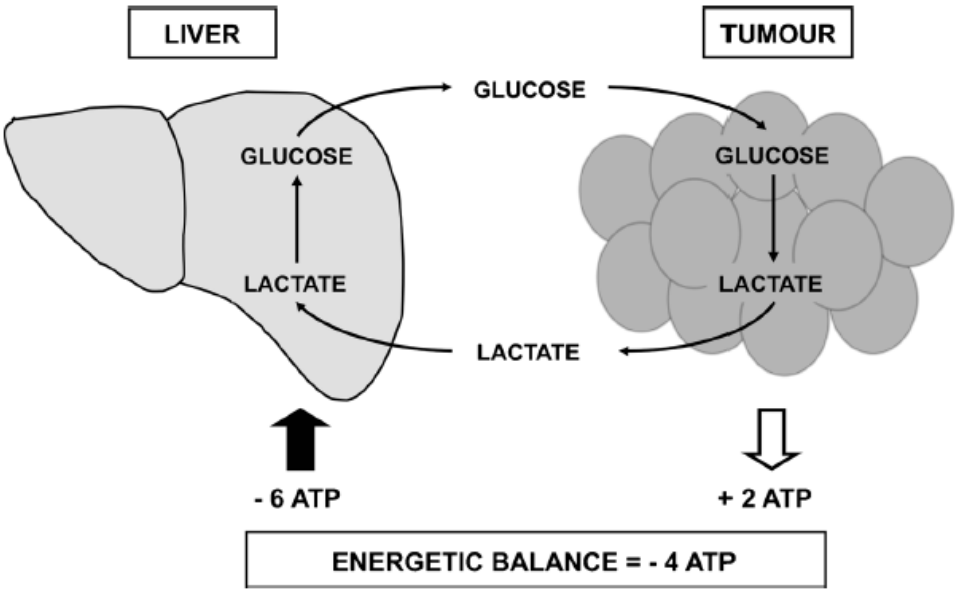

Figure 11. Example of futile cycling between the liver and the tumor (Cori cycle)[41].

In cancer cachexia, protein metabolism alterations also occur by means of altered proteostasis, where protein catabolism is favored, contributing to the loss of skeletal muscle mass and function[40]. Alterations of proteostasis can arise from the increase in protein degradation, the decrease in protein synthesis, or both. The regulation of these processes is fundamental for achieving a physiological balance between them, and depends on several signaling pathways, including the protein kinase B (AKT) pathway. In physiological conditions, AKT is active and promotes protein anabolism via the activation of the mammalian target of rapamycin complex 1 (mTORC1). In parallel, AKT inhibits catabolism by phosphorylating FoxO transcription factors, which prevents the transcription of the ubiquitin ligases MuRF-1 and Atrogin-1, overall inhibiting UPS-mediated protein degradation. During cachexia, however, several factors can inhibit the activity of AKT, including pro-inflammatory cytokines, representing a relevant mechanism of altered proteostasis in the skeletal muscle[28].

Mitochondrial dysfunction

Mitochondrial dysfunction is a central feature of cancer cachexia. Multiple studies have demonstrated that alterations of these organelles are not merely a consequence of the syndrome, rather an active contributor to its pathogenesis. This highlights mitochondria as promising therapeutic targets for counteracting cancer-induced muscle wasting[36,42,43]. In the skeletal

muscle of cachectic cancer hosts, mitochondrial alterations occur at multiple levels, impacting each of the homeostatic processes. Regarding biogenesis, reduction of the master regulator PGC-1α is frequently observed. Even when PGC-1α is unchanged, mitochondrial dynamics are usually compromised, as evidenced by the downregulation of the markers of fusion and fission Mfn2, Opa1, Drp1, and Fis1. The impairment of mitochondrial dynamics is particularly relevant, as it hampers their ability to respond and adapt to physiological and pathological stimuli[36]. Mitophagy is dysregulated as well, featuring an aberrant activation of the mitochondria disposal system. Indeed, several mitophagy-related markers have been reported to be elevated in the skeletal muscle of cachectic tumor-bearing mice, including BNIP3, LC3-II, PINK1, and Parkin[36,44]. Consistent with the combined disruption of mitochondrial biogenesis and disposal, muscle mitochondrial mass is commonly found to be reduced, which is reflected in the transcript and protein levels of markers such as cytochrome c and translocase of outer mitochondrial membrane 20 (TOMM20). The disruption of mitochondrial homeostasis culminates in impaired mitochondrial function. Multiple studies, in fact, have reported reduced mitochondrial respiration and altered levels of energy-associated metabolites in the muscle of cachectic tumor-bearing mice. Importantly, mitochondrial alterations have been validated in the skeletal muscle of cancer patients with cachexia, proving the relevance of mitochondrial dysfunction to muscle wasting[36].

Oxidative stress

Oxidative stress is one of the most common and central mechanisms involved in the pathogenesis of cancer cachexia[37]. Oxidative stress is defined as an imbalance in the normal reduction-oxidation (redox) equilibrium, which results from an increase in reactive oxygen species levels and/or a decrease in the function of antioxidant systems[37]. In cancer cachexia, pro-inflammatory cytokines, such as TNFα, can induce ROS production from several sources, including mitochondria and the NADPH oxidase complex[37]. Beyond these sources, xanthine oxidase (XO) has been identified as another contributor to oxidative stress. This enzyme is involved in the oxidation of hypoxanthine to xanthine and subsequently to uric acid, a process throughout which ROS are produced[37,45]. This pathway is clinically relevant, as patients with cancer often present with hyperuricemia (elevated uric acid levels), a condition linked to the upregulation of XO activity[45]. Importantly, the increase in ROS levels leads to oxidative damage of cellular organelles, membranes, and macromolecules such as proteins and lipids[37].

Oxidative stress also promotes mitochondrial dysfunction, induces protein degradation via increased UPS activity, and reduces protein synthesis, overall contributing to cancer-induced muscle wasting[37,46] (Figure 12).

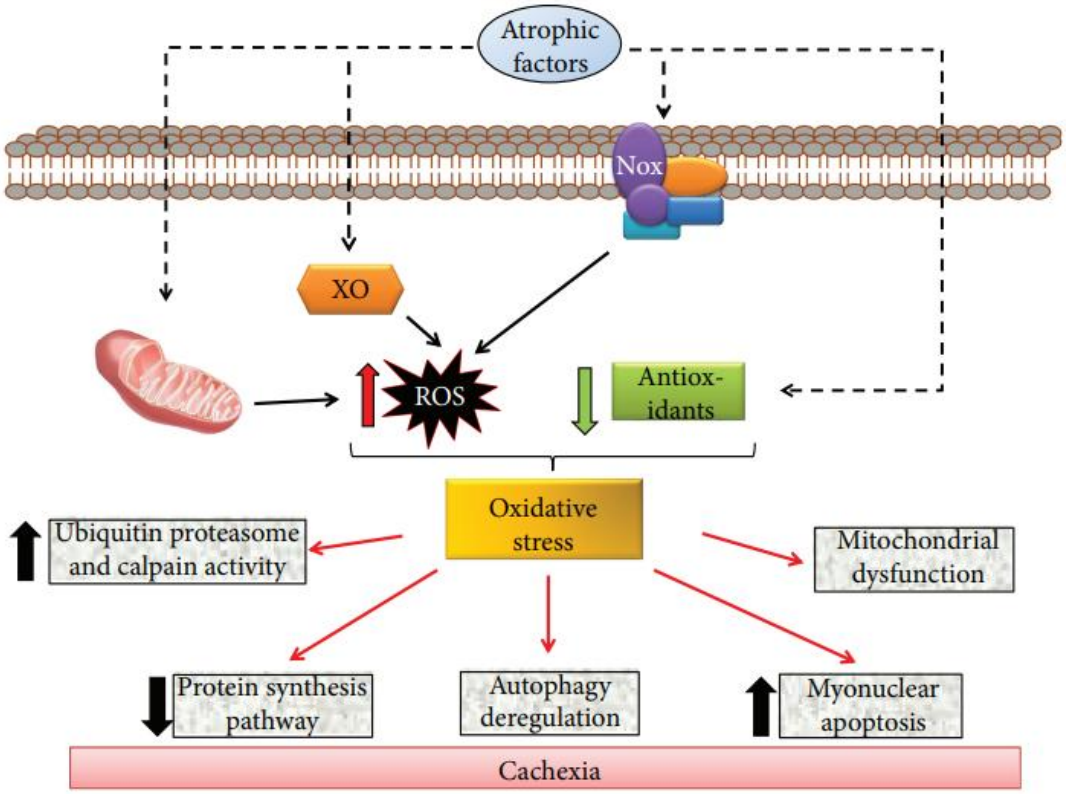

Figure 12. Role of oxidative stress in cancer-induced muscle wasting[37].

2.2.2. Immune response in cancer cachexia

The capacity of cancer to evade both the innate and adaptive immune response is well established, and tumor progression often requires myeloid cells within the tumor microenvironment to support processes like the epithelial-mesenchymal transition and angiogenesis. However, the specific role of the altered immune response in the onset of cachexia has been largely neglected. Research has mostly focused on the impact of circulating pro-inflammatory mediators on peripheral tissue signaling, rather than on the immune cells themselves. Consequently, little is known about the complex interactions linking immune cells,

the tumor, and peripheral tissues, which represents a critical axis in the pathogenesis of cachexia[35] (Figure 13).

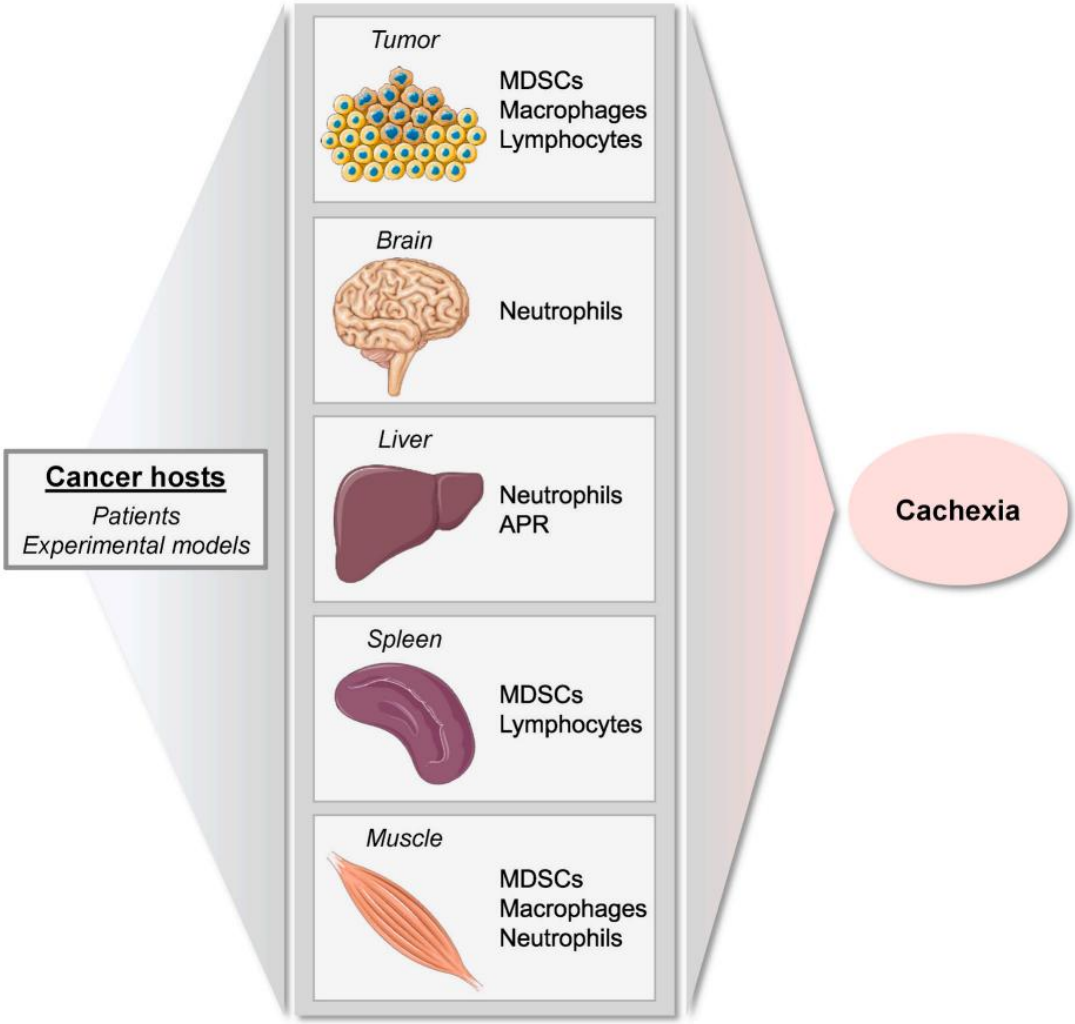

Figure 13. Immune cells potentially implicated in the onset and progression of cancer cachexia[35]. APR: acute phase response; MDSCs: myeloid-derived suppressor cells.

It has been proposed that quantitative and qualitative alterations in myeloid cells, rather than just cytokine production, drive cancer cachexia[47]. Specifically, Myeloid-Derived Suppressor Cells (MDSCs), which are "pathologically activated" myeloid cells with an immunosuppressive phenotype, have been shown to increase in parallel with tumor mass. Their expansion is thought to promote a cachexia-prone environment by suppressing the adaptive immune response, which favors tumor growth, and by becoming a source of pro-inflammatory mediators[47,48].

Importantly, MDSC differentiation depends on the exposure of myeloid cells to pro-inflammatory mediators, which are elevated in the context of cancer-associated systemic inflammation. Moreover, MDSCs have an immunomodulating action that enriches peripheral tissues with immunosuppressive neutrophils and monocytes, as well as affecting T and B cells and natural killer cells[35,48]. The pathological activation of MDSCs is linked to metabolic reprogramming, often in the glucose-poor tumor microenvironment, which pushes MDSCs toward an immunosuppressive and tumor-promoting phenotype[35,49]. Other factors can contribute to the immunosuppressive phenotype of MDSCs, including the activation of STAT3[50], and the overexpression of indolamine 2,3-dioxygenase 1 (IDO1)[51]. Importantly, these pathways are directly implicated in cachexia. Specifically, STAT3 activation has been shown as a causative factor in muscle wasting, and its inhibition can preserve muscle mass and function[52,53]. As for IDO1, it produces kynurenine, which has been implicated in the reduction of myofiber size and muscle force[51,54]. Consistently, endurance exercise, which is a promising anti-cachexia strategy, is able to reduce circulating kynurenine levels. Interestingly, the proposed mechanism consists of exercise-dependent induction of PGC-1α1, which in turn enhances the expression of the kynurenine-processing enzymes kynurenine aminotransferases[55]. Several studies have also shown the direct implication of MDSC expansion in cachexia. For instance, they are associated with metabolic alterations and can infiltrate in the skeletal muscle of tumor-bearing mice promoting wasting, while their partial depletion has protective effects[56–58]. Overall, MDSCs are strongly implicated in tumor progression and muscle wasting, highlighting the importance of the tumor-immune cells-peripheral tissues link and uncovering the relevance of immune dysregulation for cachexia as well.

Macrophages are relevant for cancer cachexia as well. While their presence in the tumor microenvironment is strictly associated with tumor progression, they are also fundamental for local immune responses and physiological processes in peripheral tissues such as the skeletal muscle. The specific phenotype they assume, which, simplistically, can be categorized as M1 (pro-inflammatory) or M2 (anti-inflammatory), is critical in dictating their function[35,59]. In injured skeletal muscle, they are central to the repair process. Initially, M1 macrophages clear debris and allow myogenic cell proliferation and differentiation. Subsequently, M2 macrophages are recruited, and in turn release cytokines (such as IL10, TGFβ, IGF-1) that promote the formation of new myofibers[60]. Despite their implication in tumor progression and muscle physiology, however, little is known of the role of macrophages in cancer cachexia.

Interestingly, the administration of IL4 in tumor-bearing mice was shown to improve survival, myogenesis and muscle fitness. These effects were associated with increased M2 macrophages in both the skeletal muscle and the tumor microenvironment, suggesting potential beneficial effects provided by M2 macrophages in the context of cancer cachexia[61].

Finally, lymphocytes are frequently altered in cancer patients, showing alterations in the number of circulating $CD8^+$ and $CD4^+$ T cells, including T regulatory (Treg) cells, which have been correlated with poor prognosis. However, the link between T lymphocyte alterations and cancer cachexia is still unclear. Indeed, while T cell activity could reduce tumor burden and thereby improve cachexia, it could also worsen wasting by enhancing the systemic pro-inflammatory environment[35]. Despite the complexity of this link, recent observations suggest their involvement in cachexia. Supporting a potential protective role, the infusion of naive T helper cells into tumor-bearing mice was shown to protect against muscle atrophy[62]. Furthermore, in gastrointestinal cancer patients, naive and memory T lymphocyte levels have been found to correlate with muscle function, while Treg abundance correlates with BMI changes. Conversely, it has also been reported that cytotoxic T cells can actively contribute to adipose tissue wasting, highlighting the dual and complex nature of the adaptive immune response in cachexia[63].

2.2.3. Therapeutic strategies for cancer cachexia

Despite its relevance for the clinical outcomes of cancer patients, current therapies for cachexia have not proven effective, highlighting this syndrome as an unmet medical need[29,35]. Given the complexity of the pathogenesis of this systemic multi-factorial syndrome, interventions should be multimodal, integrating drugs, exercise, and nutritional interventions, as evidence shows how targeting single specific pathways is unlikely to succeed. Adding a layer of complexity, these multimodal therapeutic approaches need to be combined with anticancer treatments[29].

Anti-inflammatory and anti-cytokine strategies

Given that systemic inflammation and pro-inflammatory cytokines are central in the pathogenesis of cancer cachexia, anti-inflammatory strategies hold significant therapeutic potential. These approaches include general agents like non-steroidal anti-inflammatory drugs (NSAIDs) and more specific anti-cytokine agents. While appealing for their accessibility and

tolerability, and despite some studies showing improvements in body weight and physical performance in cachectic patients, evidence supporting the use of NSAIDs in the clinical setting is still insufficient[64]. Anti-cytokine strategies, which are designed to block cytokine synthesis or action, have also been investigated, but conclusive evidence of effectiveness is lacking. For instance, agents targeting TNFα failed to show improvements of cachexia in cancer patients[65,66]. Other approaches able to target in parallel inflammation and multiple cytokines (including IL6 and TNFα) were able to induce modest improvements in body weight and muscle mass[65]. While promising results emerged from targeting IL6 and growth differentiation factor 15 (GDF-15)[67–69], currently no anti-cytokine strategies have been approved for clinical use[29].

Exercise therapy and exercise mimetics

Exercise therapy is considered to be a fundamental component of multimodal interventions for cancer cachexia[29]. Indeed, the American College of Sports Medicine advises physical activity regimens for both healthy subjects and cancer patients[70]. Exercise holds significant therapeutic potential for counteracting cachexia because it can simultaneously provide anti-inflammatory and antioxidant stimuli, while improving muscle metabolism, mass and function[40]. The potential benefits of exercise for cachectic cancer patients are multiple, impacting both muscle-specific and systemic maladaptations. Regarding the skeletal muscle, exercise promotes hypertrophy and inhibits atrophy, overall counteracting cancer-associated wasting. At the molecular level, exercise promotes protein synthesis via increased mTORC1 signaling, paralleled by decreased rates of protein degradation by reducing the levels of autophagy-related proteins and E3 ligase transcripts. Additionally, exercise enhances muscle function and energy metabolism by improving mitochondrial homeostasis and function[30,70,71]. The benefits of exercise expand systemically, as it promotes an anti-inflammatory environment, that in turn impinges on cachexia-driving mechanisms, and protects from oxidative stress by stimulating the antioxidant defense systems[40,70,71]. It also counteracts cancer-induced metabolic dysregulations, such as insulin resistance by increasing GLUT4 availability on the sarcolemma[40,72]. Importantly, exercise has been shown to affect tumor growth itself, thereby impinging on systemic and muscle derangements associated with cancer[40,73]. Despite its therapeutic potential, not all cachectic cancer patients are able to perform or tolerate exercise therapy, and inadequate regimens could be detrimental[40,70]. In this context, therapeutic strategies that mimic the beneficial effects of exercise, namely “exercise mimetics”, offer a

valuable opportunity[71,74]. Exercise-mimicking agents could be used to substitute for, potentiate the effects of, and avoid the side effects of exercise. Examples include peroxisome proliferator-activated receptor (PPAR-δ) and 5' AMP-activated protein kinase (AMPK) agonists, and peroxisome proliferator-activated receptor γ coactivator-1α (PGC-1α) modulators[71,75].

Immunomodulation

Considering that alterations of the immune response contribute to both tumor progression and cachexia, strategies able to modulate the immune response (immunomodulation) represent a novel therapeutic opportunity[35]. Advanced immunotherapies, such as immune checkpoint inhibitors and chimeric antigen receptor (CAR) T-cell therapy, have revolutionized oncology. As an example, CAR-T therapy involves genetically modifying T lymphocytes to recognize specific tumor antigens[35,76]. These strategies bear great potential as they can lead to long term remission and even tumor eradication[35]. However, their clinical effectiveness is often limited due to toxicity and resistance[77]. In this context, the complex relationship between immunotherapy and cachexia is relevant. Indeed, while these therapies could potentially be used to treat cachexia, they can also induce or exacerbate the syndrome. Moreover, the presence of cachexia itself can negatively impact the anticancer effectiveness of immunotherapy[35]. Supporting this last statement, muscle wasting has been negatively correlated with survival in large B-cell lymphoma patients treated with CD19 CAR-T cells[78]. The presence of cachexia has also been reported to affect the outcomes of CAR-T cell therapy in another cohort of B cell lymphoma patients[79], and to be a predictive factor for immune checkpoint inhibitor clinical response in advanced lung cancer patients[80,81]. Collectively, the complex scenario described above suggests the need for multimodal therapeutic approaches that integrate the modulation of the immune response to counteract cachexia and, in parallel, maximize the efficacy of anticancer immunotherapies.

3. AIM OF THE STUDY

Cancer cachexia is a complex paraneoplastic syndrome affecting a significant proportion of cancer patients, complicating their clinical management, reducing their quality of life, increasing mortality rates and significantly hampering anticancer therapies[28]. Specific treatments for cancer cachexia are currently unavailable, overall highlighting the need for novel effective therapeutic strategies able to address this unmet medical need[29].

Multiple mechanisms are involved in the development and progression of cancer cachexia, including systemic inflammation, altered energy metabolism, mitochondrial dysfunction, and immune dysregulation, overall involving multiple organs[28,35,36]. Given this multi-etiological nature, therapies against cachexia must be multimodal, impinging on several pathogenic mechanisms simultaneously. Multimodal interventions are generally viewed as the combination of distinct approaches, including pharmacological, and nutritional components as well as exercise[29]. This latter, in particular, has a great potential, being able to tackle cachexia from multiple angles. However, not all cancer patients can perform physical activity, and possible side effects include the exacerbation of cachexia. For this reason, pharmacological agents able to mimic the beneficial effects of exercise have great therapeutic potential for cachectic cancer patients[29].

Given the multifactorial pathogenesis of cachexia, identifying single therapeutic agents able to target multiple pathways and mechanisms in parallel holds a high potential. Adding a layer of complexity, therapeutic strategies for cachexia and cancer should be finely coordinated, with the overall goal of counteracting cachexia-specific mechanisms while enhancing tolerance and antineoplastic effectiveness of anticancer therapies[29,35]. In this context, immunotherapy is gaining attention. While being one of the most advanced anticancer treatments, it also showed therapeutic potential for cancer cachexia, thus representing a potential bridge between therapies for the two conditions[35].

Along this line, interleukin-4 (IL4), a cytokine with anti-inflammatory properties able to promote type 2 immune responses[82,83], and its receptor were shown to be upregulated in the muscle upon strength training, suggesting their involvement in muscle anabolism[84]. In parallel, IL4 transcripts were downregulated in the liver and muscle of pancreatic cancer patients with cachexia[85]. Altogether, these findings suggest the relevance of IL4 signaling in the context of

cancer cachexia, as a possible agent able to counteract the syndrome by simultaneously targeting inflammation, improving muscle fitness, and modulating the immune response.

Consistently, a previous study investigated the role of IL4 administration in tumor-bearing mice, demonstrating that the cytokine was indeed beneficial for cancer hosts by attenuating cachexia. Specifically, it improved muscle mass and function, myogenesis, and survival[61]. However, information on the effects of IL4 on the immune response and muscle-specific and systemic metabolism in cancer cachexia is unavailable. Additionally, although suggested by previous work[61], IL4-dependent modulation of the tumor microenvironment and its relationship with cachexia progression remains a relevant open question.

Based on these premises, the present study aimed to further investigate IL4 as an immuno-metabolic modulating strategy able to improve the immune response and mimic exercise, thereby counteracting cancer cachexia. Specifically, this study aimed to expand the knowledge of the effects of IL4 administration in C26 tumor-bearing mice with a holistic approach, examining the systemic immune response, the tumor microenvironment, and both muscle-specific and systemic metabolism.

Additionally, the relevance of pathways unaffected by IL4 was assessed. For instance, the finding that IL4 did not impinge on muscle uric acid levels suggested that it does not attenuate xanthine oxidase-dependent oxidative stress, a known contributor to cancer-induced muscle wasting[37]. Hence, the inhibition of xanthine oxidase via febuxostat (FBX) in the C26 hosts was investigated as well.

4. MATERIALS AND METHODS

This work was conducted across two institutions and includes two distinct projects. The first, the "IL4 project", was conducted at the Department of Clinical and Biological Sciences of the University of Turin (Turin, Italy). The second, the "FBX project", was performed at the Department of Pathology of the University of Colorado Anschutz Medical Campus (Aurora, CO, USA).

Animals and experimental designs

IL4 project

All animal procedures were performed in compliance with the Italian Ministry of Health Guidelines and the Policy on Humane Care and Use of Laboratory Animals (NRC, 2011). The experimental protocol was approved by the Bioethical Committee of the University of Turin (Turin, Italy) and by the Italian Ministry of Health (authorization no. 579/2018-PR). Mice were housed in a temperature-controlled environment (20–23°C) on a regular 12-hour light/dark cycle, with ad libitum access to food and water throughout the experimental period.

For the IL4 project, two *in vivo* experiments were performed. In both experiments, C26 tumor-bearing mice were inoculated subcutaneously dorsally with 5×10^5 C26 colon carcinoma cells. Starting from day 5 after tumor implantation, daily IL4 (#214-14, PeproTech) treatments were performed by intraperitoneal injection (66.5 µg/kg) until the day before sacrifice. Body weight and food intake were monitored daily. On the day of sacrifice, mice were anesthetized (2% isoflurane in O_2) and blood was collected by cardiac puncture. Euthanasia was performed by cervical dislocation. Blood was centrifuged at 2500 × *g* for 15 min at 4°C to obtain plasma, which was then stored at −80 °C. Several tissues and organs were collected, weighed, frozen in liquid nitrogen, and stored at −80 °C for further analyses, unless differently specified. For each of the two *in vivo* experiments, additional details are specified below.

IL4 project – 1st in vivo experiment

Ten-week-old BALB/c male mice (Charles River Laboratories) of about 28 g were randomized into 4 experimental groups: healthy controls (C), IL4-treated controls (IL4), C26 tumor-bearing mice (C26), and IL4-treated C26 tumor-bearing mice (C26+IL4). Group size is specified in the figure legends. Animals were sacrificed on day 15 after tumor implantation. Grip strength test was performed on days 0, 5, 10 and 14 after tumor implantation using a digital grip strength meter (Bioseb) (Figure 14).

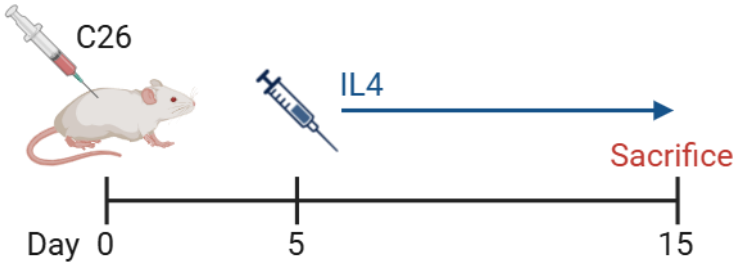

Figure 14. Schematic representation of the experimental design for the first *in vivo* experiment related to the IL4 project. Created with BioRender.com.

IL4 project – 2nd in vivo experiment

Ten-week-old BALB/c male mice (Charles River Laboratories) of about 26 g were randomized into 6 experimental groups: healthy controls (C), IL4-treated controls (IL4), C26 tumor-bearing mice sacrificed at the early time point (C26 ETP), IL4-treated C26 tumor-bearing mice sacrificed at the early time point (C26+IL4 ETP), C26 tumor-bearing mice sacrificed at the experimental endpoint (C26 EEP), and IL4-treated C26 tumor-bearing mice sacrificed at the experimental endpoint (C26+IL4 EEP). Group size is specified in the figure legends. C26 tumor-bearing mice were sacrificed at two time points: early time point (ETP, 10 days after tumor implantation) and experimental endpoint (EEP, 15 days after tumor implantation). Control mice were sacrificed at EEP. Grip strength test was performed on the day of tumor implantation and the day before sacrifice using a digital grip strength meter (Bioseb) (Figure 15).

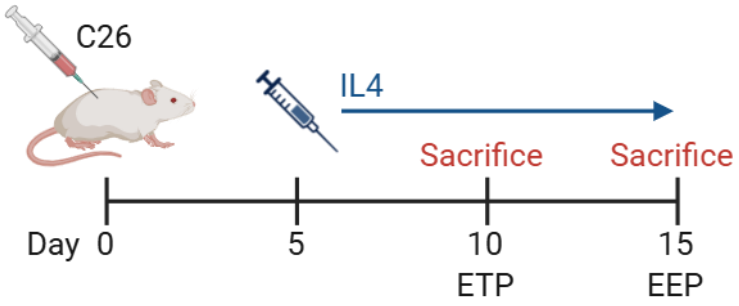

Figure 15. Schematic representation of the experimental design for the second *in vivo* experiment related to the IL4 project. Created with BioRender.com.

FBX project

All animal procedures were approved by the Institutional Animal Care and Use Committee at University of Colorado Anschutz Medical Campus and were in compliance with the National

Institutes of Health Guidelines for Use and care of Laboratory Animals. Mice were housed in a temperature-controlled environment (20–23°C) on a regular 12-hour light/dark cycle, with ad libitum access to food and water throughout the experimental period.

Twelve-week-old CD2F1/Hsd male mice (Envigo, an Inotiv company) of about 30 g were randomized into 4 experimental groups: healthy controls (C), febuxostat (FBX)-treated controls (C+FBX), C26 tumor-bearing mice (C26), and FBX-treated C26 tumor-bearing mice (C26+FBX). Group size is specified in the figure legends. C26 tumor-bearing mice were inoculated subcutaneously dorsally with 1×10^6 C26 colon carcinoma cells. Starting from day 4 after tumor implantation, daily FBX (#S1547, Selleck Chemicals) was administered orally by gavage (10 mg/kg/day in 5% DMSO and 95% corn oil) until the day before sacrifice. FBX naive mice were administered equal volumes of vehicle (5% DMSO and 95% corn oil). Animals were sacrificed on day 11 after tumor implantation. Body weight and food intake were monitored daily. On the day of sacrifice, mice were anesthetized (2% isoflurane in O_2) and blood was collected by cardiac puncture. Euthanasia was performed by cervical dislocation. Blood was centrifuged at 2500 × *g* for 15 min at 4°C to obtain plasma, that was then stored at −80 °C. Several tissues and organs were collected, weighed, frozen in liquid nitrogen, and stored at −80 °C for further analyses, unless differently specified (Figure 16).

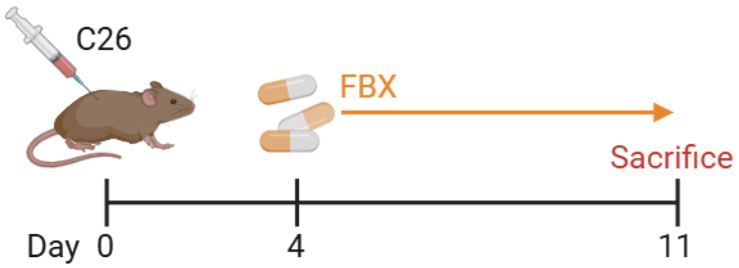

Figure 16. Schematic representation of the experimental design for the *in vivo* experiment related to the FBX project. Created with BioRender.com.

Cell culture

C26 colon carcinoma cells, obtained from Prof M.P. Colombo (National Cancer Institute, Milano, Italy) in 2005, were cultured in high-glucose Dulbecco's modified Eagle's medium (DMEM), supplemented with 10% fetal bovine serum (FBS), 1 mg/mL of sodium pyruvate, and 1 IU/mL of penicillin and streptomycin, and were incubated at 37°C, 5% CO_2, 5% O_2. The day of tumor implantation, cells were trypsinized and resuspended in sterile saline solution at a concentration of 5×10^6 cells/mL.

Cytokine and chemokine profiling assay

Several cytokines and chemokines were assessed in plasma samples using the commercially available Milliplex Kits (#MCYTMAG-70K-PX32, #MAGE1MAG-25K, Merck Life Science) and the Luminex technology. This system, which combines the principle of a sandwich immunoassay with fluorescent bead-based technology, allows individual and multiplex analysis of different analytes in a single microtiter well[86]. The assays were performed by Bioclarma srl (Turin, Italy), following the manufacturer's instructions. Samples were analyzed in 96-well microplates. The content of each well was drawn up into the Bio-Plex 200 System array reader (Bio-Rad Laboratories), which identifies and quantifies each specific reaction based on bead color and fluorescent signal intensity. The data were then processed using Bio-Plex Manager software using five-parametric curve fitting and converted to pg/mL.

Spleen immunophenotyping

Splenocyte isolation

Freshly excised spleens were homogenized using the flat plunger end of a syringe and a 100 µm filter. The isolated splenocytes were counted by flow cytometry (BD Accuri C6), centrifuged at 1000 × *g* for 10 min, resuspended in freezing medium (DMEM supplemented with 20% FBS, 10% dimethyl sulfoxide, 1% sodium pyruvate, 1% L-glutamine, and 1% penicillin/streptomycin) and stored at −80°C.

Flow cytometry analysis

Cryopreserved splenocytes were thawed, centrifuged at 1000 × *g* for 10 min, and resuspended in Roswell Park Memorial Institute (RPMI) medium supplemented with 10% Fetal Bovine Serum (FBS). Following cell counting, approximately 1×10^6 splenocytes were dispensed into FACS tubes. Cells were washed twice in washing solution (PBS containing 2% FBS and 0.1% sodium azide) by centrifugation at 1000 × *g* for 10 min. Afterwards, cells were treated with an Fc receptor blocker (anti-mouse CD16/CD32, #156604, BioLegend, 2 µL) for 15 min at 4°C.

For the analysis of myeloid populations (macrophages, MDSCs), cells were incubated for 30 min at 4°C with the following surface antibodies: FITC anti-mouse CD11b (#101206, BioLegend, 0.5 µL), APC anti-mouse F4/80 (#123116, BioLegend, 1 µL), Brillan Violet 412 anti-mouse CD206 (#141717, BioLegend, 3 µL), Alexa Fluor 647 anti-mouse Ly-6G/Ly-6C (Gr1) (#108418, BioLegend, 0.5 µL). After the incubation, cells were washed with washing solution at 1000 × *g* for 5 min and prepared for acquisition.

For the analysis of Tregs, cells were first stained for surface markers for 30 min at 4°C with: FITC anti-mouse CD4 (#100406, BioLegend, 0.5 µL), PE anti-mouse CD25 (#113704, BioLegend, 1 µL). Following surface staining, cells were washed with washing solution at 1000 × *g* for 5 min, then fixed and permeabilized using the Cyto-Fast Fix/Perm Solution (#426803; BioLegend, 150 µL) according to the manufacturer's instructions (20 min at RT). Cells were then incubated with the Fc receptor blocker as described above and subsequently stained for 30 min at 4°C with Pacific Blue anti-mouse FOXP3 (#126410, BioLegend, 0.5 µL). Finally, cells were washed with Cyto-Fast Perm/Wash solution (#126410, BioLegend, 1 mL) and prepared for acquisition.

To detect intracellular cytokine production, and thus $CD4^+$, Th1, Th17, $CD8^+$, CTL, TC17 cells, 1×10^6 splenocytes were cultured in 48-well plates and activated for 18 hours with 50 ng/mL PMA (#P8139, Sigma-Aldrich), 500 ng/mL Ionomycin (#I0634, Sigma-Aldrich), and 10 ng/mL Brefeldin A (#B7651, Sigma-Aldrich). Following stimulation, cells were harvested, and washed with washing solution at 1000 × *g* for 5 min. Cells were then incubated with the Fc receptor blocker as described above, and stained for surface markers for 30 min at 4°C with: FITC anti-mouse CD4 (#100406, BioLegend, 0.5 µL), PE anti-mouse CD8a (#100708, BioLegend, 1 µL). Subsequently, cells were washed with washing solution at 1000 × *g* for 5 min, then fixed and permeabilized using the Cyto-Fast Fix/Perm Solution as described above. Cells were then incubated with the Fc receptor blocker as described above. Finally, cells were stained intracellularly for 30 min at 4°C with: Alexa Fluor 647 anti-mouse IL-17A (#506912, BioLegend, 0.5 µL), Pacific Blue anti-mouse IFN-γ (#505818, BioLegend, 0.2 µL). After washing with Cyto-Fast Perm/Wash solution (#126410, BioLegend, 1 mL), stained cells were prepared for acquisition.

All stained cells were acquired on a BD FACSCelesta™ (BD Biosciences). Data were analyzed using FlowJo v10 software (BD Biosciences).

Hematological analysis

Immediately after collection, the blood was transferred into tubes containing K-EDTA to a final concentration of 0.2% EDTA to prevent coagulation. A complete blood count (CBC) was performed immediately using the ProCyte Dx Haematology Analyser (IDEXX Laboratories). For this study, the total leukocyte count (K/µL) and the differential percentages of lymphocytes, monocytes, neutrophils, eosinophils, and basophils were included in the analysis.

Tumor histological analysis

A portion of the tumor was frozen in melting isopentane cooled in liquid nitrogen and stored at −80 °C. Sections 7 µm thick were then obtained using a cryostat (Leica) and were stored at −20 °C for later staining. The sections were used for Hematoxylin and Eosin staining. Briefly, sections were first warmed to room temperature before staining. Sections were incubated for 4 min in hematoxylin, washed with running water, and subsequently incubated in eosin for 8 s. Following a final wash with running water, dehydration was performed using an increasing ethanol gradient (75%, 90%, and 100%). Sections were then cleared in xylene and mounted with Eukitt Quick-hardening mounting medium (#03989, Sigma-Aldrich). Stained sections were examined by light microscopy (Nikon Eclipse TS100) and images were acquired using a digital camera (Nikon COOLPIX 4500). Full sections were reconstructed using GIMP software (2.10.38). The tumor necrotic area was quantified as the ratio of the eosinophilic areas lacking nuclei to the total area of the tumor section, using ImageJ software (2.14.0). For each sample, two sections were quantified, and the average value was used.

Tumor single nuclei RNA sequencing

Nuclei isolation

Nuclei were isolated from about 50 mg of tumor tissue, using the Chromium Nuclei Isolation Kit (#1000494, #1000450, #1000449, #1000448, #1000447, 10X Genomics) according to the manufacturer's instructions.

Fixed single nuclei RNA sequencing

Nuclei were fixed in a 4% formaldehyde fixative solution and using the Chromium Next GEM Single Cell Fixed RNA Sample Preparation Kit (#1000414, 10X Genomics). The fixed nuclei were checked for the absence of debris, followed by counting and normalization before the whole transcriptome probe pairs (10X Genomics) were added to the fixed single nuclei suspensions to hybridize to their complementary target RNA in an overnight incubation. After hybridization, the unbound probes were washed off. The fixed and probe-hybridized single nuclei suspensions were loaded onto Chromium X (10X Genomics) microfluidics instrument to generate partitioned nanoliter-scale droplets in oil emulsion. Each droplet contains a barcoded gel bead, a single nucleus, and enzyme Master Mix (10X Genomics) for probe pair ligation and gel bead primer barcode extension. The droplets in oil emulsion were placed in a thermal cycler for 60 min at 25°C, 45 min at 60°C, and 20 min at 80°C. The single nuclei-barcoded, ligated probe product underwent library preparation to be compatible with Illumina next-generation sequencing.

Sequencing

The gene expression library derived from single nuclei-barcoded, ligated probe product was sequenced as paired-end 150 bp reads on the Illumina NovaSeq X (Illumina) at the University of Colorado - Genomics Shared Resource (Aurora, CO, USA) at a depth of 20,000 reads per nucleus.

Data analysis

Single nuclei RNA sequencing FASTQ files were processed using Cell Ranger (v7.1.0, 10X Genomics) to assign reads to genes based on the Chromium Mouse Transcriptome Probe Set (v1.0.1). The resulting count matrices were analyzed in Python 3.12 using Scanpy (v1.11.4) in the Google Colab environment. After quality control filtering (>200 detected genes, <20% mitochondrial reads, and >500 UMIs per nucleus), gene expression values were normalized to 10,000 counts per cell and log-transformed. Mouse genes were converted to their human orthologs using the MyGene.info API (v3.2.2). Gene symbols were queried in batches of 100 against the Mus musculus genome to retrieve corresponding Homo sapiens orthologs based on Ensembl annotations; when multiple orthologs were found, the primary match was retained, and genes lacking orthologs were excluded. Batch correction was performed using HarmonyPy (v0.0.10), applying the sample identity as the batch key and integrating results with principal component analysis (PCA; 50 components) prior to alignment. Dimensionality reduction and visualization were conducted using UMAP (15 neighbors), followed by Leiden clustering (resolution = 0.5) to identify transcriptionally distinct populations. Cell type annotation combined canonical marker evaluation with automated classification using CellTypist (v1.7.1) and CancerFinder (v1.0.1). Comparative analyses included the estimation of cell-type proportions across experimental groups. Statistical significance was assessed using either the Chi-squared test or Fisher's exact test, depending on expected count assumptions, with p-values adjusted for multiple testing via the Bonferroni correction. The relative prevalence of macrophage subtypes (M1- and M2-like) was evaluated using signature enrichment scores based on previously published gene expression programs[87]. Gene expression values were averaged for each gene within every combination of experimental group and cell type, standardized using z-score normalization (mean = 0, SD = 1; scikit-learn v1.6.1), symmetrically clipped to the range of −2 to 2, and visualized as heatmaps generated with Seaborn (v0.13.2).

Western blotting

Total protein extracts were obtained from the gastrocnemius muscle. About 50 mg of tissue were homogenized using a bead homogenizer (Bullet Blender, Next Advance) in RIPA buffer

solution containing freshly added protease (#10981532001, Roche; #A2183, ITW Reagents) and phosphatase (#P0044, Sigma-Aldrich) inhibitors. The homogenates were then sonicated for 10 s at low intensity, centrifuged at 15682 × *g* for 5 min at 4°C and the supernatant collected. Total protein concentration was assessed using the Bradford assay (Bio-Rad), BSA being the working standard. Samples were prepared by adding equal amounts of protein (10-45 µg) to sample loading buffer (Sample Buffer, Laemmli 2x Concentrate, #S3401, Sigma-Aldrich), followed by heat-denaturation (5 min at 95°C; omitted for OXPHOS). Protein samples were resolved by SDS-PAGE (Criterion TGX Precast Gels, Bio-Rad) and transferred to nitrocellulose membranes (Trans-Blot Turbo Transfer System, Bio-Rad). Membranes were blocked using Tris-buffered saline (TBS) containing 0.05% Tween and 5% nonfat dry milk and then incubated overnight with one of the following antibodies: Akt (#9272, Cell Signaling Technology, 1:1000), P-Akt Ser473 (#4060, Cell Signaling Technology, 1:2000), BNIP3 (#3769, Cell Signaling Technology, 1:1000), Cyt C (#556433, BD Biosciences, 1:1000), MFN2 (#9482, Cell Signaling Technology, 1:1000), MuRF-1 (#SAB1411517, Sigma-Aldrich, 1:500), NF-κB p65 (#6956, Cell Signaling Technology, 1:1000), P-NF-κB p65 Ser536 (#3033, Cell Signaling Technology, 1:1000), OPA1 (#80471, Cell Signaling Technology, 1:1000), PGC-1α (#AB3242, Merck Millipore, 1:1000), Stat3 (#4904, Cell Signaling Technology, 1:2000), P-Stat3 Tyr705 (#9138, Cell Signaling Technology, 1:1000), TOMM20 (#ab186735, Abcam, 1:2000), Total OXPHOS Antibody Cocktail (#ab110413, Abcam, 1:1000), Ubiquitin (#3933, Cell Signaling Technology, 1:1000), VDAC (#4866, Cell Signaling Technology, 1:1000) and vinculin (#sc73614, Santa Cruz Biotechnology, 1:2000). Goat anti-mouse and goat anti-rabbit HRP conjugated IgGs (Bio-Rad, 1:8000) were used as secondary antibodies, except for OXPHOS, for which Mouse TrueBlot ULTRA Anti-Mouse Ig HRP (#18-8817-33, Rockland, 1:1000) was used. Membrane-bound immune complexes were detected by an enhanced chemiluminescence system (Clarity Western ECL Blotting Substrate, #1705061, Bio-Rad and ChemiDoc XRS+ System, Bio-Rad). Protein loading was normalized according to vinculin expression, unless differently specified. Bands were quantified by densitometric analysis using ImageLab software (6.0.1, Bio-Rad).

Hexokinase activity assay

The enzymatic activity of hexokinase was assessed on the gastrocnemius muscle, using the Hexokinase Activity Assay Kit (#ab13697, Abcam) according to the manufacturer's instructions. Briefly, 10 mg of tissue were homogenized using a bead homogenizer (Bullet Blender, Next Advance), and the resulting lysate was diluted 1:10 in assay buffer. Absorbance

was measured in a kinetic mode, and hexokinase activity was calculated between two time points within the linear range, using the NADH standard curve.

High-resolution respirometry in permeabilized fibers

Mitochondrial respiration was assessed on freshly excised gastrocnemius muscle, using the Oroboros Oxygraph-O2k (Oroboros Instruments). Right after excision, tissues were placed into ice-cold BIOPS solution [50 mM MES, 20 mM taurine, 0.5 mM dithiothreitol, 6.56 mM $MgCl_2$, 5.77 mM Na_2ATP, 15 mM Na_2Phosphocreatine, 20 mM imidazole, 10 mM Ca-EGTA buffer (2.77 mM CaK_2EGTA + 7.23 mM K_2EGTA; 0.1 µM free calcium) pH 7.1 adjusted with 5 N KOH] and were further dissected manually into about 2 mg fiber bundles under a dissecting microscope. Oxygen consumption rate (OCR) analysis requires plasma membrane permeabilization, with effective washout of free cytosolic molecules, including adenylates, substrates, and cytosolic enzymes, making externally added compounds accessible to the mitochondria[88]. Thus, muscle fiber bundles were permeabilized by placing them into separate wells of a 12-well plate filled with 2 mL BIOPS solution containing saponin (50 µg/mL) and incubated with gentle shaking on ice for 20 min. Muscle fiber bundles were then washed in 2 mL ice-cold BIOPS solution with gentle shaking for 10 min. Samples were then gently blotted dry on filter paper, weighed, and inserted into the respirometer chambers containing the respiration medium MiR05 (0.5 mM EGTA, 3 mM $MgCl_2$, 60 mM K-lactobionate, 20 mM taurine, 10 mM KH_2PO_4, 20 mM HEPES, 110 mM sucrose, and 1 g/l BSA, pH 7.1). Respiration was recorded using a SUIT protocol SUIT-008_O2_pfi_D014[89,90] in a hyper-oxygenated environment. The following substrates and inhibitors were sequentially added: 1) 1 mM malate, 5 mM pyruvate to determine non-phosphorylating LEAK respiration supported by complex I-linked substrates; 2) 5 mM ADP to achieve maximal phosphorylating respiration from electron input through complex I (CI OXPHOS capacity); 3) 10 µM cytochrome c to assess the integrity of the outer mitochondrial membrane; 4) 10 mM glutamate (CI OXPHOS capacity); 5) 10 mM succinate to saturate complex II and achieve maximal convergent electron flux through complex I and II (CI and CII OXPHOS capacity); 6) 0.5 µM FCCP to assess complex I and II linked maximal capacity (CI and CII ETS capacity); 7) 0.5 µM rotenone to inhibit complex I (CII ETS capacity); and 8) 2.5 M antimycin A to inhibit complex III and obtain the residual oxygen consumption (ROX). Complex IV activity was evaluated after antimycin A, by ascorbate (0.5 mM) and TMPD (N, N, N', N'-tetramethyl-p-phenylenediamine; 2 mM) injection. Finally, 200 mM azide was adjusted to inhibit complex IV. Oxygen fluxes of the different respiratory states

were corrected by subtracting residual oxygen consumption following antimycin A treatment and normalized to muscle fiber bundle wet mass.

Muscle cryopreservation for high-resolution respirometry

Mitochondrial respiration was also assessed on cryopreserved gastrocnemius muscle. Right after excision, the gastrocnemius muscle was cryopreserved according to Kuznetsov AV et al[91]. Briefly, muscle tissues were immersed in 200 µL of cryopreservation solution (BIOPS solution containing 30% DMSO and 10 mg/mL fatty acid-free BSA). After 5 s of equilibration in the cryopreservation solution, the samples were snap frozen in liquid nitrogen and stored at −80°C. Before OCR analysis, tubes were placed in a water bath at 37°C and, when the cryopreservation solution was completely thawed, muscle tissues were immediately transferred and washed in the respiration medium MiR05 containing 2 mg/mL BSA to minimize the time of contact with DMSO. From this step onward, the procedure continued with muscle fiber bundle permeabilization as described in the previous paragraph.

Metabolomics and lipidomics

Metabolomic and lipidomic analyses were performed on the gastrocnemius muscle and the liver. Frozen tissues were weighed to the nearest 0.1 mg. Metabolites were extracted from frozen tissue specimens by the addition of ice-cold 5:3:2 MeOH:MeCN:H2O (v/v/v) at 15 mg/mL. Tubes were then vigorously vortexed for 30 min at 4°C. Supernatants were clarified by centrifugation (18,000 × g for 10 min at 4°C). Next, hydrophilic metabolites were separated and measured (10 µL injection) by ultra-high-pressure liquid chromatography coupled to mass spectrometry (UHPLC-MS — Vanquish and Orbitrap Exploris 120, Thermo Fisher) using a 5 min C18 gradient as previously described[92]. Samples were randomized and then analyzed in negative and positive ion modes (separate runs). The mass spectrometer scanned using full MS from 65-975 m/z at 120,000 resolution. Electrospray ionization was achieved with 50 sheath gas, 10 auxiliary gas, and 3 kV spray voltage. Following data acquisition, .raw files were converted to .mzXML using RawConverter. Following, metabolites were assigned and peaks integrated at the MS1 level using El-Maven (Elucidata) in conjunction with the KEGG database and an in-house standard library.

Lipids were extracted from frozen tissue specimens by the addition of ice-cold methanol at 15 mg/mL. Tubes were vortexed for 30 min at 4°C. Supernatants were clarified by centrifugation (18,000 × g for 10 min at 4°C). Next, lipids were separated and measured (5 µL injection) by ultra-high-pressure liquid chromatography coupled to mass spectrometry (UHPLC-MS —

Vanquish and Q Exactive, Thermo Fisher) using a 5 min C18 lipidomics gradient as previously described[93]. Samples were randomized and then analyzed in negative and positive ion modes (separate runs). The MS scanned 125 to 1500 m/z with 70,000 resolution, 4 kV spray voltage, 45 sheath gas, and 25 auxiliary gas. The MS was run in data-dependent acquisition mode (ddMS2) with top10 fragmentation. Raw MS data files were searched using LipidSearch v 5.0 (ThermoFisher).

Quality control for each of the omics analyses was assessed using technical replicates run at the beginning, end, and at defined intervals within each sequence.

***Ex vivo* muscle contractility**

Ex vivo muscle contractility assessment was performed on the extensor digitorum longus (EDL) muscle. Muscles were quickly excised in a tray containing Tyrode solution (121 mM NaCl, 5.0 mM KCl, 1.8 mM $CaCl_2$, 0.5 mM $MgCl_2$, 0.4 mM NaH_2PO_4, 24 mM $NaHCO_3$, 0.1 mM EDTA, and 5.5 mM glucose), and stainless-steel hooks were tied to both tendons using 4-0 silk sutures. Subsequently, muscles were positioned in a mounted force transducer (Aurora Scientific) and incubated in a heated bath containing Tyrode solution with continuous supplementation of O_2/CO_2 (95/5%). After 10 min of incubation, the maximum twitch force was obtained by determining the optimal muscle length. Force data were collected and analyzed with the Dynamic Muscle Control/Data Acquisition and Dynamic Muscle Control Data Analysis programs (Aurora Scientific). The EDL muscle weight and optimal muscle length were used to determine the specific force.

Xanthine oxidase activity assay

The enzymatic activity of xanthine oxidase was assessed on the gastrocnemius muscle using the Xanthine Oxidase Activity Assay Kit (#ab102522, Abcam), following the manufacturer's instructions. Briefly, about 40 mg of tissue were homogenized using a bead homogenizer (Bullet Blender, Next Advance), and the resulting lysate was diluted 1:2 in assay buffer. Absorbance was measured in a kinetic mode, and xanthine oxidase activity was calculated between two time points within the linear range, using the H_2O_2 standard curve.

Uric acid assay

Uric acid levels were measured in plasma samples using the QuantiChrom™ Uric Acid Assay Kit (#DIUA-250, BioAssay Systems), following the manufacturer's instructions. Briefly, 5 µL of sample were added in duplicate to a 96-well plate. After the addition of the working reagent

and a 30 min incubation at room temperature, the absorbance was read at 562 nm. Uric acid concentration was calculated using the provided standard and expressed in mg/dL.

Data analysis

Statistical analysis and data visualization were performed using GraphPad Prism software (10.2.3, GraphPad). Data are presented as the mean ± standard deviation, unless otherwise noted. Outliers were identified according to ROUT (Q=1%) and excluded. Normality of the distributions was assessed by Shapiro-Wilk test. For normal distributions, significance of the differences was evaluated by Student's t test or analysis of variance (ANOVA) followed by Tukey's test. For non-normal distributions, significance of the differences was evaluated by Mann-Whitney test or Kruskal-Wallis test followed by Dunn's test. Differences with p-value < 0.05 were considered statistically significant. Correlation analyses were performed using Pearson's (for normal distributions) or Spearman's (for non-normal distributions) correlation coefficient.

Metabolomic and lipidomic data were analyzed and visualized using MetaboAnalyst software (6.0) and R (4.4.2). Significant metabolites and lipids were identified with an FDR < 0.1 and a p-value < 0.05.

Data processing and statistical analyses specific to single nuclei RNA sequencing are described in the 'Tumor single nuclei RNA sequencing' section above.

5. RESULTS

5.1. IL4 administration counteracts cachexia in the C26 tumor-bearing mice

At the experimental endpoint (EEP, day 15 after tumor implantation), a significant loss of body weight was observed in untreated C26 tumor-bearing mice as compared to controls. Consistently with a previous study[61], this phenotype was prevented by IL4 administration. At the early time point (ETP; day 10 after tumor implantation), instead, C26-induced body weight loss was undetectable in both treated and untreated mice (Figure 17A). Skeletal muscle mass, muscle strength and white adipose tissue mass showed a significant decrease in the C26 group only at EEP, with IL4 exerting a marked protective effect. Splenomegaly, progressively occurring in the C26 hosts starting from ETP, was significantly increased by IL4, suggesting that the interference exerted by the cytokine on the immune system is an early event. Liver mass did not exhibit significant tumor- or IL4-dependent modulations at both time points. However, at EEP, a non-significant tendency towards increased liver mass was observed in the IL4-treated C26 hosts as compared to their untreated counterparts (Figure 17B-F). A reduction in food intake could be observed in the C26 tumor-bearing mice starting from day 11 after tumor implantation. Conversely, IL4-treated C26 tumor-bearing mice did not show anorexia, even though a tendency towards a reduction in food intake could be observed starting from day 11 (Figure 17G). While previous work[61] and an additional experiment (Figure 18G) showed different food intake patterns, the possibility that the efficacy of IL4 partially relies on food intake preservation cannot be discarded. The different body weight observed between IL4-treated and untreated C26 hosts at EEP was independent of tumor burden. Indeed, tumor mass, which increased from ETP to EEP, remained comparable between treated and untreated mice within each time point, with a non-significant decreasing trend in IL4-treated mice at EEP (Figure 17H). The lack of an effect of IL4 treatment on the kinetics of tumor growth was confirmed by an additional experiment, where tumor mass was comparable between IL4-treated and untreated C26 tumor-bearing mice (Figure 18C). The results described above were replicated in an independent experiment following the same experimental design, with sacrifice at the experimental endpoint only (Figure 18).

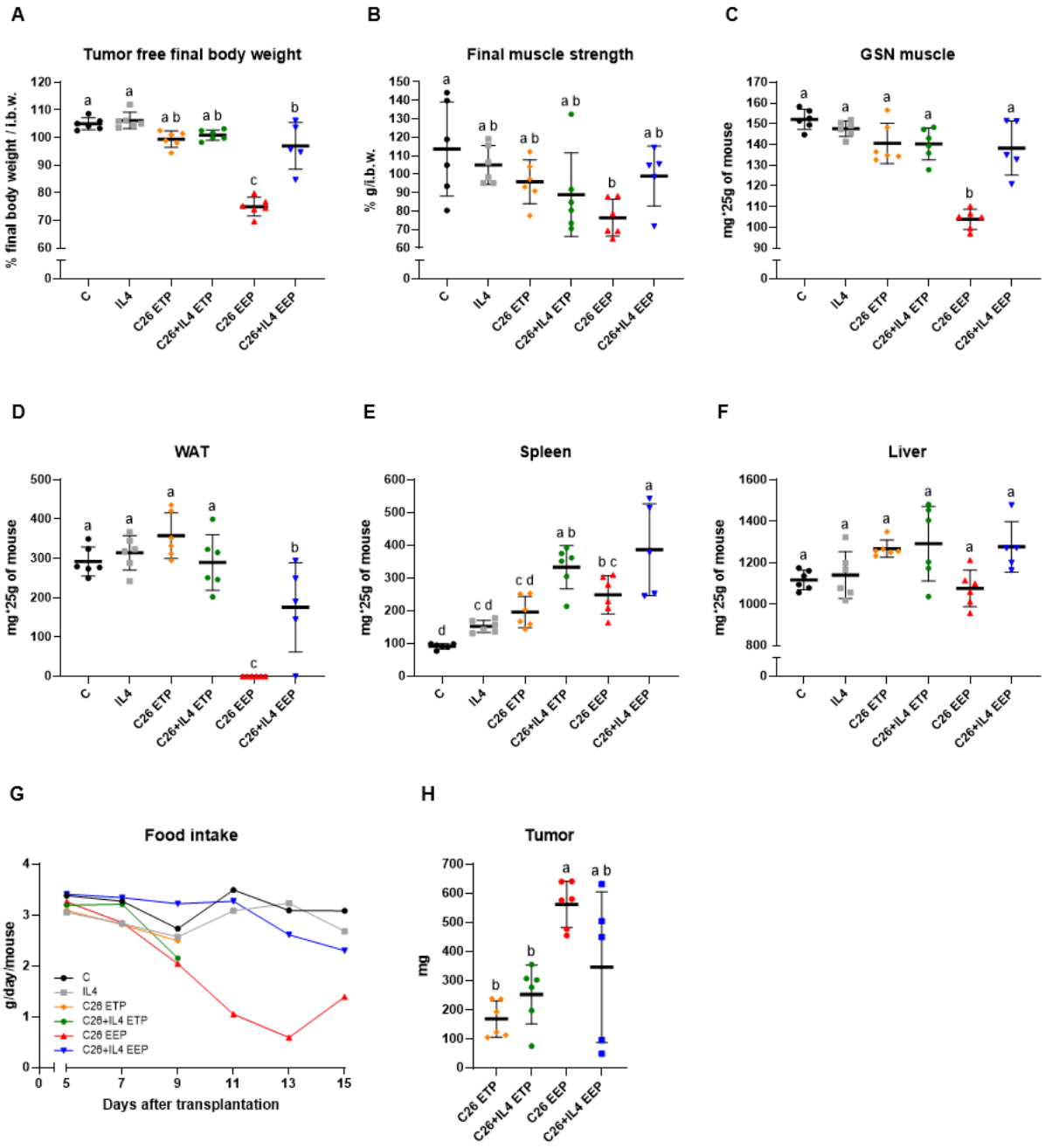

Figure 17. Effects of IL4 treatment on the C26 tumor-bearing mice at different time points. (*A*) Tumor free final body weight expressed as percentage of the initial body weight (i.b.w.). (*B*) Final muscle strength (grip strength test) normalized by the initial body weight and expressed as percentage of the initial muscle strength. (*C-F*) Gastrocnemius (GSN) muscle weight (*C*), white adipose tissue (WAT) weight (*D*), spleen weight (*E*) and liver weight (*F*), normalized to 25g of mouse body weight and expressed in mg. (*G*) Food intake kinetic curve from day 5 (first day of IL4 treatment) to day 15 after tumor implantation. Food intake expressed as g/day/mouse. Before day 5, food intake was stable and homogenous across groups

(cumulative food intake from day 2 to day 5 after tumor transplantation: C = 10.15 g/mouse, IL4 = 9.16 g/mouse, C26 ETP = 9.26 g/mouse, C26+IL4 ETP = 9.56 g/mouse, C26 EEP = 9.78 g/mouse, C26+IL4 EEP = 10.23 g/mouse). (*H*) Tumor weight expressed in mg. Experimental groups: control (C; n=6), IL4-treated control (IL4; n=6), C26 tumor-bearing mice sacrificed at ETP (C26 ETP; n=6), IL4-treated C26 tumor-bearing mice sacrificed at ETP (C26+IL4 ETP; n=6), C26 tumor-bearing mice sacrificed at EEP (C26 EEP; n=6), IL4-treated C26 tumor-bearing mice sacrificed at EEP (C26+IL4 EEP; n=5). Data expressed as mean ± standard deviation, except for food intake. Significant differences ($p < 0.05$) represented by different letters.

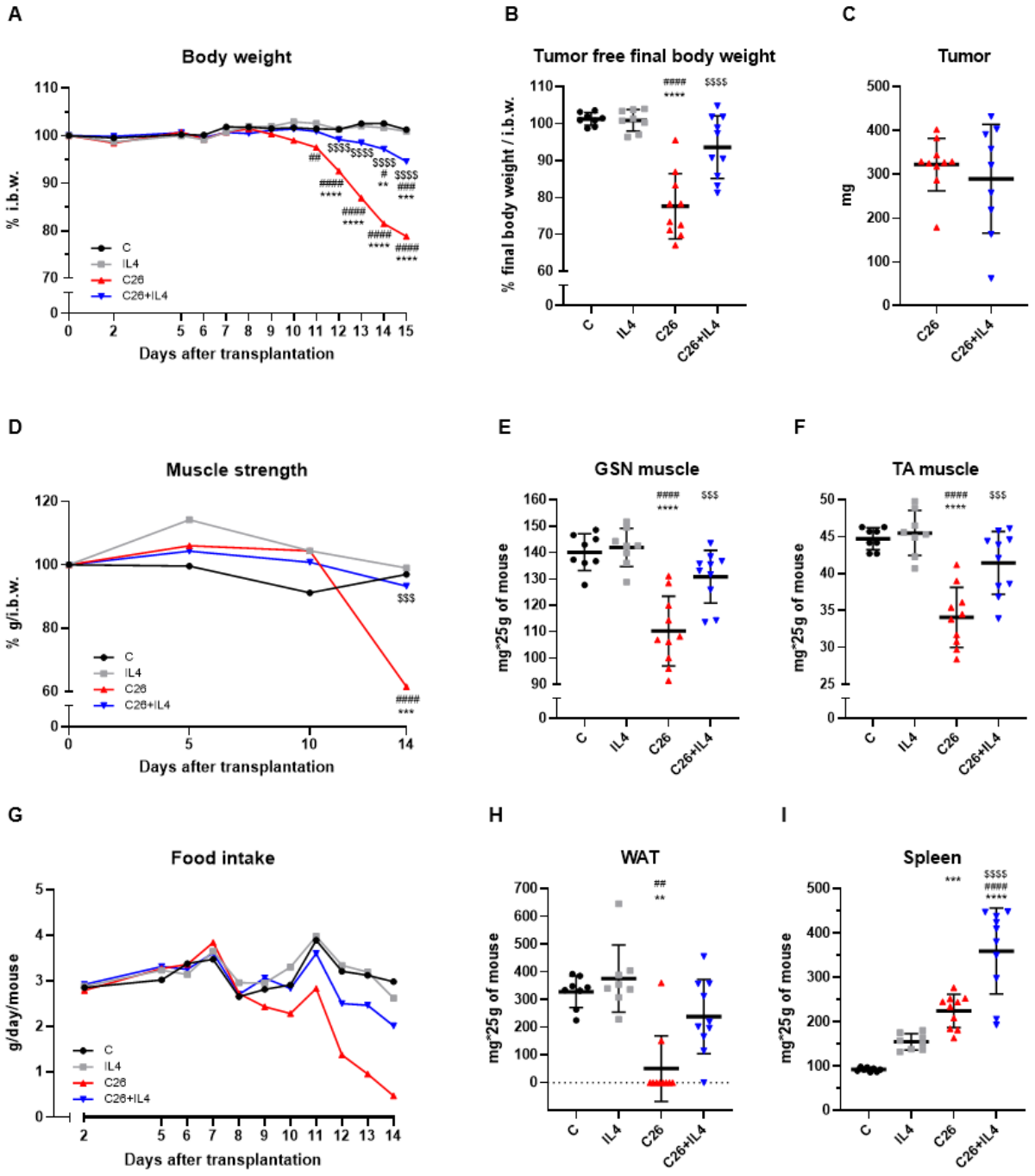

Figure 18. Effects of IL4 treatment on the C26 tumor-bearing mice from an independent experiment following the same experimental design, with sacrifice at the experimental endpoint only. (*A*) Body weight kinetic curve. Body weight expressed as percentage of the initial body weight (i.b.w.). (*B*) Tumor free final body weight expressed as percentage of the i.b.w. (*C*) Tumor weight expressed in mg. (*D*) Muscle strength kinetic curve. Muscle strength normalized by the initial body weight and expressed as percentage of the initial muscle strength. (*E*, *F*, *H*, *I*) Gastrocnemius (GSN) muscle weight (*E*), tibialis anterior (TA) muscle weight (*F*),

white adipose tissue (WAT) weight (*H*), and spleen weight (*I*), normalized to 25g of mouse body weight and expressed in mg. (*G*) Food intake kinetic curve. Food intake expressed as g/day/mouse. Experimental groups: control (C; n=8), IL4-treated control (IL4; n=8), C26 tumor-bearing mice (C26; n=10), IL4-treated C26 tumor-bearing mice (C26+IL4; n=10). Data expressed as mean ± standard deviation, except for food intake. Significance of the differences: *p < 0.05; **p < 0.01; ***p < 0.001; ****p < 0.0001 vs C; # vs IL4; $ vs C26.

5.2. Circulating cytokine and chemokine levels are modulated by IL4 in the C26 hosts

The presence of the tumor altered the circulating levels of numerous cytokines and chemokines. Specifically, the levels of IL6, IL10, TNFα, FGF21, IP-10, and Eotaxin were increased in the C26 hosts as compared to controls and were, at least partially, reduced by IL4 treatment (Figure 19B, C, E, G-I). Conversely, Jagged1 levels, which were significantly reduced in the C26 group, were increased by IL4 administration back towards control levels (Figure 19J). By contrast, Notch1 and Leptin levels were significantly reduced in both IL4-treated and untreated C26 tumor-bearing mice (Figure 19K, L). The levels of IFN-γ and IL17 were unaltered across groups, although IL17 showed a non-significant trend towards reduction in both IL4-treated control and C26 tumor-bearing mice (Figure 19D, F). As expected, IL4 administration always resulted in increased circulating IL4 levels, irrespective of the presence or the absence of the tumor, confirming the efficacy of the treatment (Figure 19A).

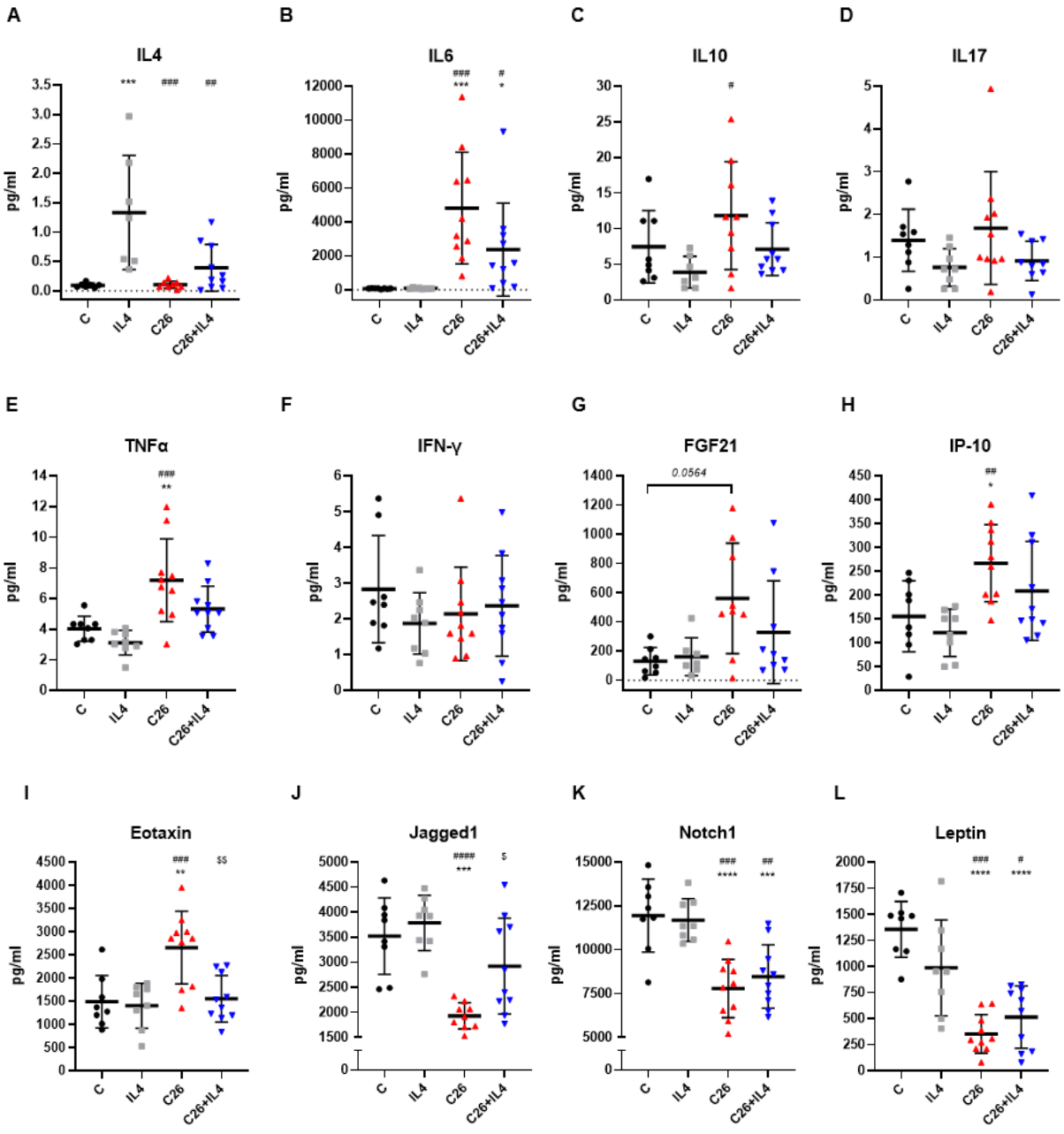

Figure 19. Circulating cytokine and chemokine profile at endpoint. (*A-L*) Plasma levels of IL4 (*A*), IL6 (*B*), IL10 (*C*), IL17 (*D*), TNFα (*E*) IFN-γ (*F*), FGF21 (*G*), IP-10 (*H*), Eotaxin (*I*), Jagged1 (*J*), Notch1 (*K*), and Leptin (*L*), expressed in pg/mL. Experimental groups: control (C; n=8), IL4-treated control (IL4; n=8), C26 tumor-bearing mice (C26; n=10), IL4-treated C26 tumor-bearing mice (C26+IL4; n=10). Data expressed as mean ± standard deviation. Significance of the differences: *p < 0.05; **p < 0.01; ***p < 0.001; ****p < 0.0001 vs C; # vs IL4; $ vs C26. Abbreviations: interleukin (IL), tumor necrosis factor-alpha (TNFα), interferon gamma (IFN-γ), fibroblast growth factor 21 (FGF21), interferon-gamma-inducible protein 10 kDa (IP-10).

5.3. IL4 counteracts cancer-induced immunosuppression

In the spleen, the percentage of macrophages was significantly increased in both IL4-treated and untreated C26 hosts as compared to controls. A similar pattern was observed for spleen derived M2 macrophages, although a trend towards control values was observed in the C26+IL4 group (Figure 20A-C). The percentage of myeloid-derived suppressor cells (MDSCs), significantly higher in the C26 hosts than in controls, was restored to values close to normal by IL4 treatment (Figure 20D). In contrast to macrophages, spleen derived $CD4^+$ cells were significantly reduced in both IL4-treated and untreated C26 tumor-bearing mice as compared to controls. Similar trends could be observed for spleen derived Th1 cells, the reduction of which being more marked and significant in the C26+IL4 group only. The percentages of Th17 cells were similar across all groups (Figure 20E-G). Consistently with MDSCs abundance, the percentage of spleen derived regulatory T cells (Tregs) was significantly increased in the C26 hosts and was fully restored to control levels by IL4 treatment (Figure 20H). Spleen derived $CD8^+$ cells and cytotoxic T lymphocytes (CTLs) were significantly lower than controls only in the IL4-treated C26 tumor bearers, while TC17 cells were unaltered across all groups (Figure 20I-K).

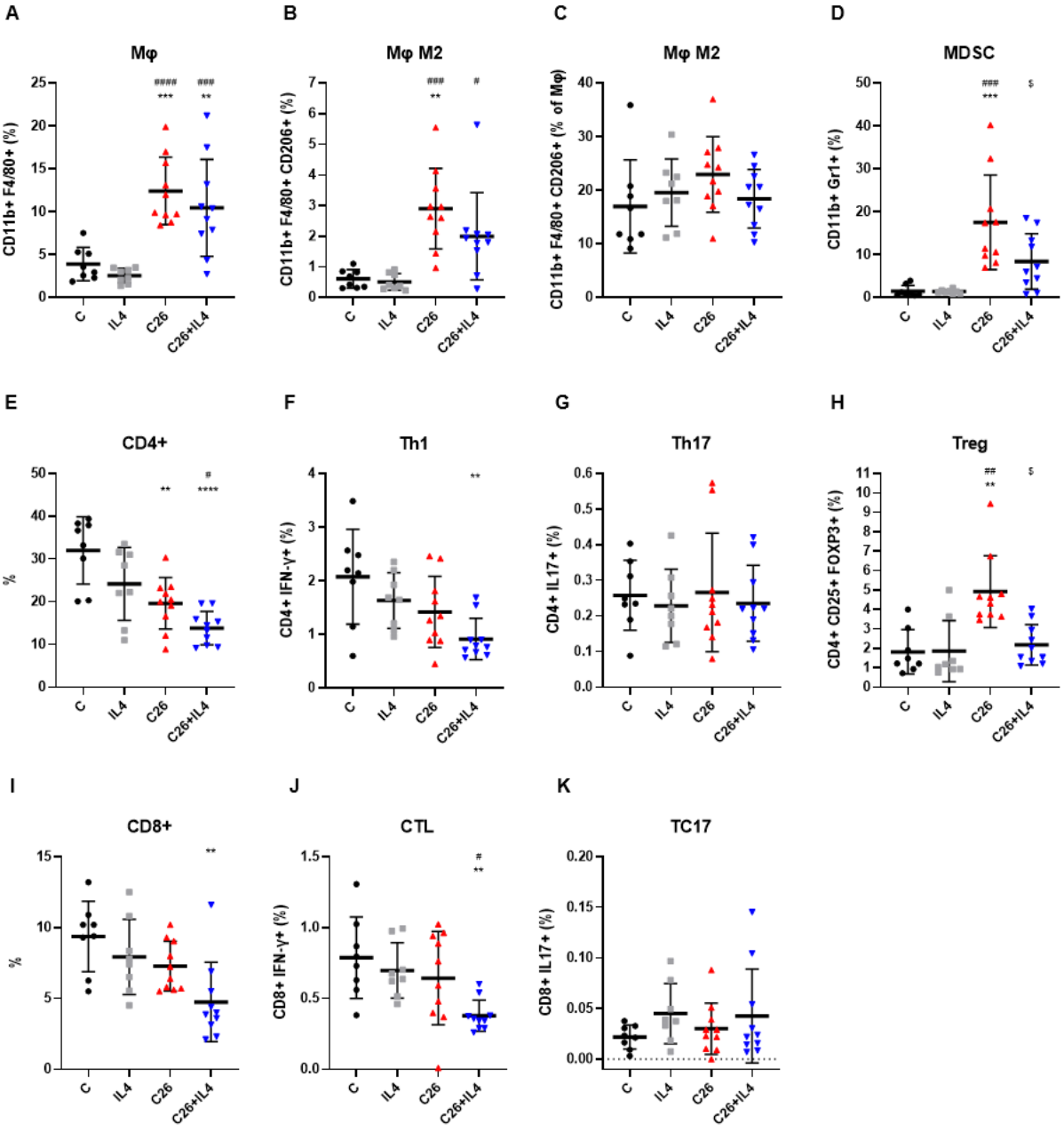

Figure 20. Spleen immunophenotype at endpoint. (*A*, *B*) Macrophages (*A*), and M2 macrophages, expressed as percentage of the total splenic immune cells. (*C*) M2 macrophages, expressed as percentage of the total splenic macrophages. (*D-K*) MDSC (*D*), $CD4^+$ (*E*), Th1 (*F*), Th17 (*G*), Treg (*H*), $CD8^+$ (*I*), CTL (*J*), and TC17 (*K*), expressed as percentage of the total splenic immune cells. Experimental groups: control (C; n=8), IL4-treated control (IL4; n=8), C26 tumor-bearing mice (C26; n=10), IL4-treated C26 tumor-bearing mice (C26+IL4; n=10). Data expressed as mean ± standard deviation. Significance of the differences: *$p < 0.05$; **$p < 0.01$; ***$p < 0.001$; ****$p < 0.0001$ vs C; # vs IL4; $ vs C26. Abbreviations: macrophages (Mφ), myeloid-derived suppressor cells (MDSC), T helper cells type

1 (Th1), T helper 17 cells (Th17), regulatory T cells (Treg), cytotoxic T lymphocytes (CTL), interleukin-17-producing $CD8^+$ T cells (TC17).

The total circulating leukocyte count did not change in controls and tumor host, in the presence or in the absence of IL4, though a non-significant increasing trend was observed in the C26 tumor-bearing mice (Figure 21A). Lymphocytes and eosinophils in the tumor hosts were significantly lower than in the healthy mice, regardless of IL4 treatment, while neutrophils showed an opposite pattern (Figure 21B, D, E). Although monocyte and basophil populations were not significantly modulated across groups, IL4 treatment showed a non-significant trend to increase monocytes while decreasing basophils in both control and C26 bearers (Figure 21C, F).

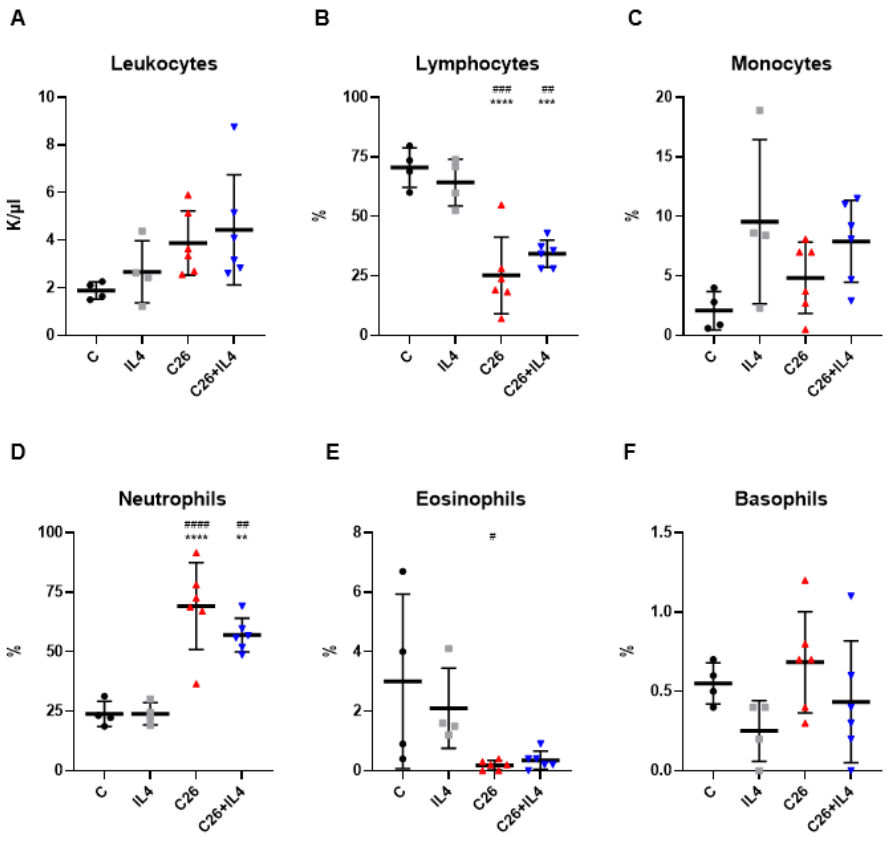

Figure 21. Circulating immune cells at endpoint. (*A*) Leukocytes levels in the blood expressed in K/µL. (*B-F*) Lymphocytes (*B*), monocytes (*C*), neutrophils (*D*), eosinophils (*E*), and basophils (*F*), expressed as percentage of the total leukocytes in the blood. Experimental groups: control (C; n=4), IL4-treated control (IL4; n=4),

C26 tumor-bearing mice (C26; n=6), IL4-treated C26 tumor-bearing mice (C26+IL4; n=6). Data expressed as mean ± standard deviation. Significance of the differences: *p < 0.05; **p < 0.01; ***p < 0.001; ****p < 0.0001 vs C; # vs IL4; $ vs C26.

5.4. Immunosuppression correlates with cachexia

The elevated percentages of splenic MDSCs and Tregs reflected the occurrence of immunosuppression in the C26 tumor-bearing mice, which was counteracted by IL4. A correlation analysis combining data in both treated and untreated C26b hosts, revealed a significant negative relation between the percentages of splenic MDSCs and Tregs and final body weight, muscle mass, and muscle strength (Figure 22).

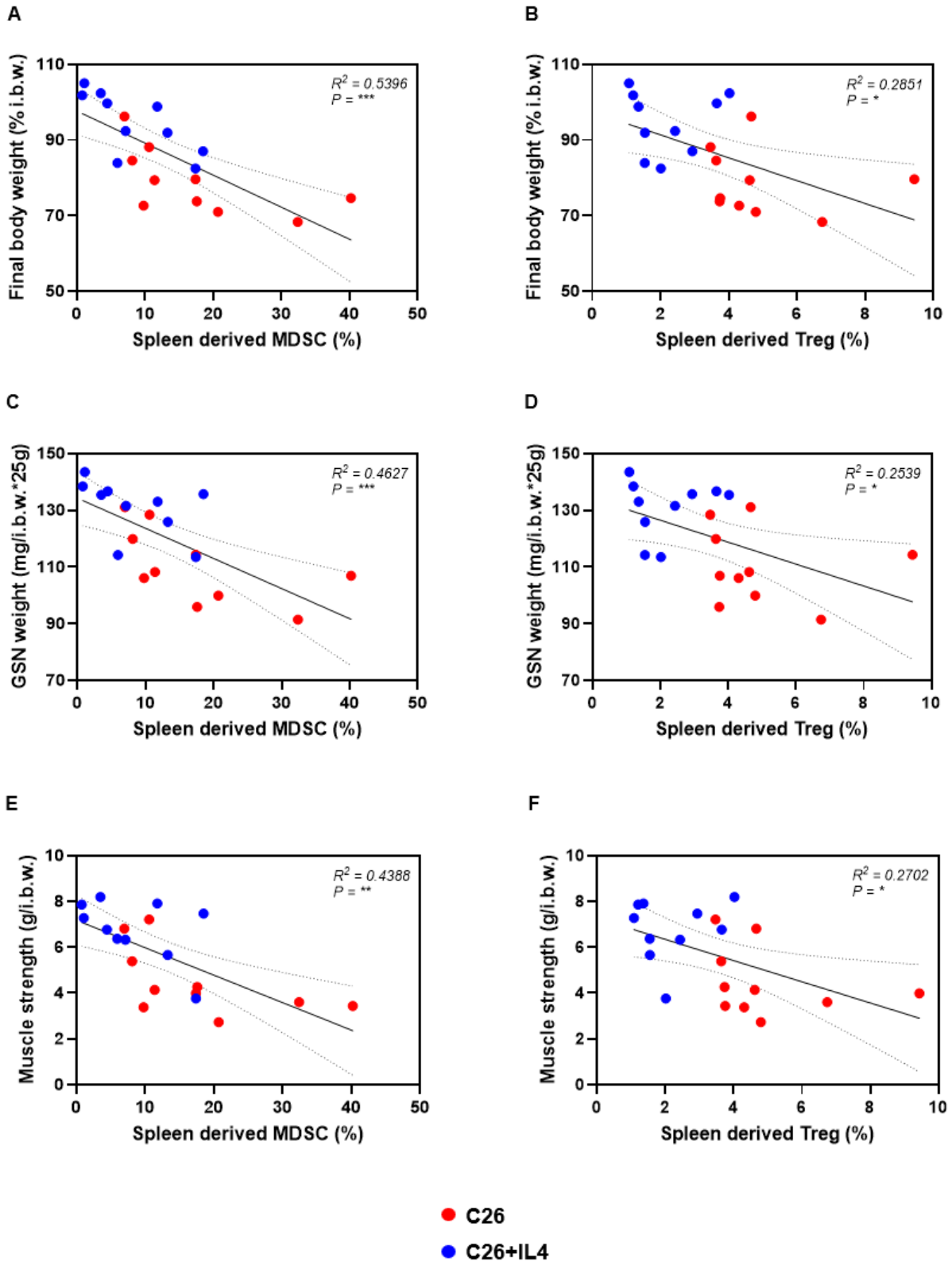

Figure 22. Correlation analysis between cachexia parameters and splenic immunosuppressive cells. (*A*, *B*) Correlation between final body weight and splenic MDSCs (*A*) or Tregs (*B*). (*C, D*) Correlation between GSN muscle weight and splenic MDSCs (*C*) or Tregs (*D*). (*E, F*) Correlation between final muscle strength

and splenic MDSCs (*E*) or Treg (*F*). Correlations performed using Pearson's correlation coefficient (R^2). Final body weight expressed as percentage of the initial body weight (I.b.w.). GSN weight normalized to 25g of mouse body weight and expressed in mg. Final muscle strength expressed as grams normalized by the i.b.w. Splenic MDSCs and Tregs expressed as the percentage of the total splenic immune cells. Experimental groups: C26 tumor-bearing mice (C26; n=10), IL4-treated C26 tumor-bearing mice (C26+IL4; n=10). Significances: *p < 0.05; **p < 0.01; ***p < 0.001; ****p < 0.0001. Abbreviations: gastrocnemius (GSN), myeloid-derived suppressor cells (MDSC), regulatory T cells (Treg).

5.5. IL4 administration modulates the tumor microenvironment

Increased necrosis in tumors from IL4-treated versus untreated C26 hosts was previously reported[61]. However, this comparison was limited because tumors from treated and untreated mice were collected at different time points. In the current study, all tumors were collected on day 15 after implantation. The histological assessment revealed a non-significant trend towards reduction in the necrotic area in tumors from IL4-treated C26 hosts as compared to their untreated counterparts (Figure 23).

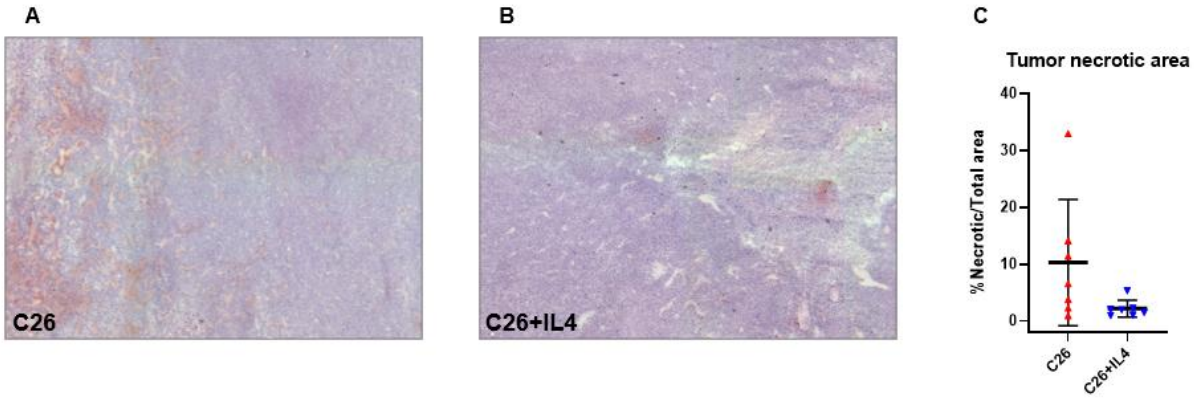

Figure 23. Tumor histological analysis at endpoint. (*A*, *B*) Representative images of hematoxylin and eosin staining performed on tumor section (5x). (*C*) Tumor necrotic area expressed as percentage of the total area of the tumor section. Experimental groups: C26 tumor-bearing mice (C26; n=7), IL4-treated C26 tumor-

bearing mice (C26+IL4; n=7). Data expressed as mean ± standard deviation. Significance of the differences: *p < 0.05; **p < 0.01; ***p < 0.001; ****p < 0.0001.

Despite the lack of significant effects on tumor mass or necrosis, IL4 treatment markedly modulated the tumor microenvironment (TME). Indeed, UMAP analysis of the single-nuclei RNA-sequencing data revealed clear differences in the cellular composition and relative abundance of cell populations between tumors from the C26 and C26+IL4 groups (Figure 24A). Specifically, tumors from IL4-treated mice exhibited a striking decrease in T cells compared to those from untreated animals. In parallel, the proportion of malignant cells was increased by IL4 treatment. Other cell populations within the TME were also modulated, though to a lesser extent. Both fibroblasts and macrophages were increased in tumors from IL4-treated mice, whereas epithelial cells were reduced (Figure 24B). As for macrophages, in the tumors from untreated C26 hosts, M1 macrophages were more abundant than the M2, while the opposite was observed in those of the C26+IL4 group (Figure 24C).

IL4 treatment also modulated gene expression across several cell populations in the TME. As an example, the expression of Ki67 and GDF15 was upregulated in malignant cells from the C26+IL4 group as compared to the C26 group, a pattern also observed in B cells, endothelial cells, epithelial cells, fibroblasts, macrophages, and T cells. Similarly, FGF21 expression was increased by IL4 treatment in B cells, epithelial cells, monocytes, and plasma cells (Figure 24D).

A

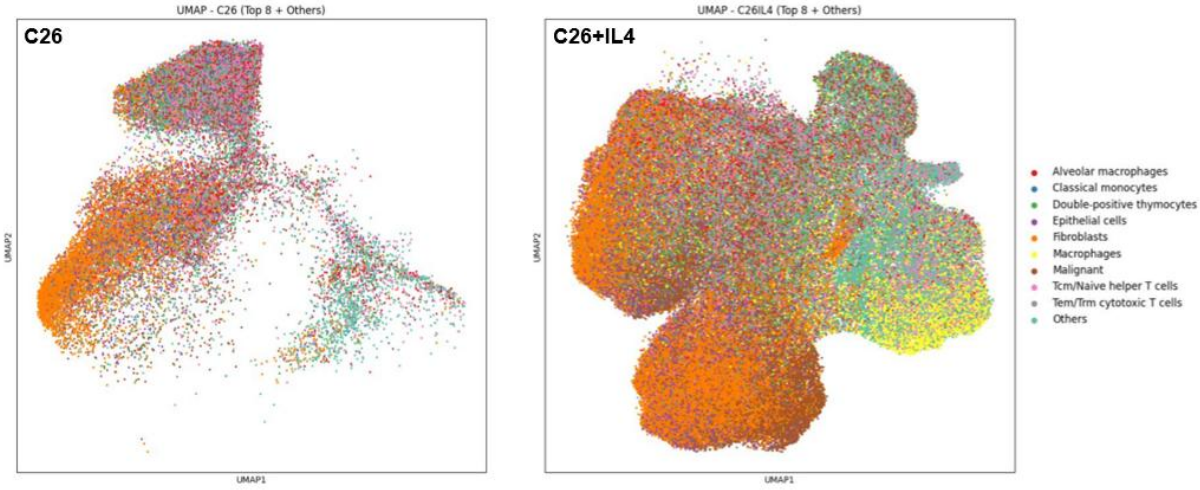
UMAP - C26 (Top 8 + Others)
C26
UMAP2
UMAP1
UMAP - C26IL4 (Top 8 + Others)
C26+IL4
UMAP2
UMAP1
Alveolar macrophages
Classical monocytes
Double-positive thymocytes
Epithelial cells
Fibroblasts
Macrophages
Malignant
Tcm/Naive helper T cells
Tem/Trm cytotoxic T cells
Others

B

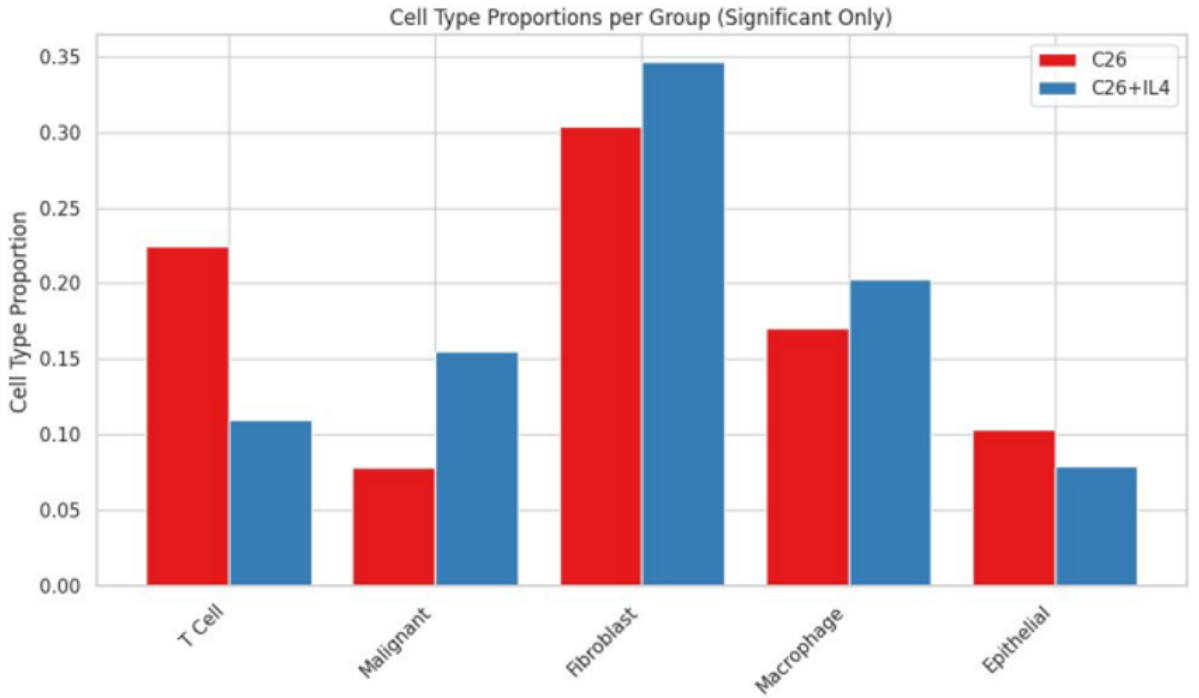
Cell Type Proportions per Group (Significant Only)
C26
C26+IL4
Cell Type Proportion
0.35
0.30
0.25
0.20
0.15
0.10
0.05
0.00
T Cell
Malignant
Fibroblast
Macrophage
Epithelial

C

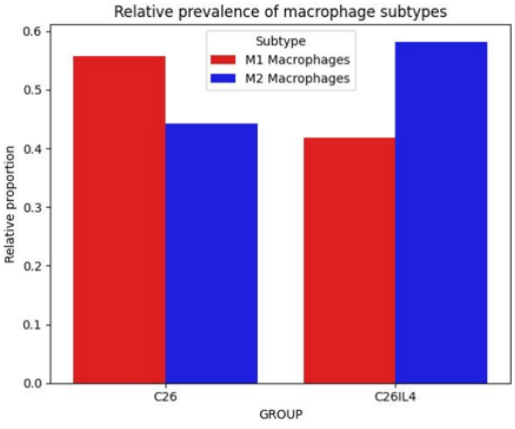
Relative prevalence of macrophage subtypes
Subtype
M1 Macrophages
M2 Macrophages
Relative proportion
0.6
0.5
0.4
0.3
0.2
0.1
0.0
C26
C26IL4
GROUP

D

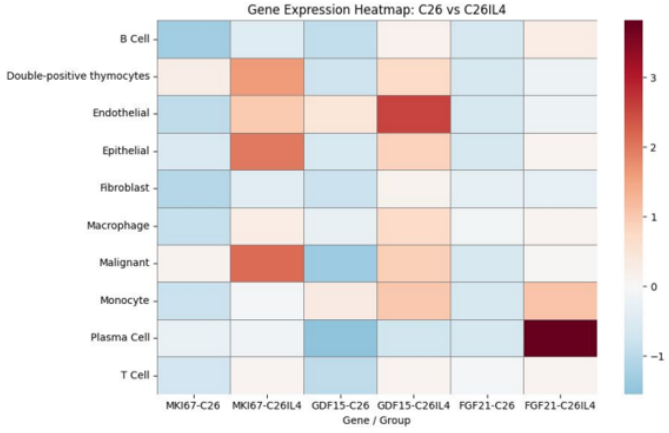
Gene Expression Heatmap: C26 vs C26IL4
B Cell
Double-positive thymocytes
Endothelial
Epithelial
Fibroblast
Macrophage
Malignant
Monocyte
Plasma Cell
T Cell
MKI67-C26
MKI67-C26IL4
GDF15-C26
GDF15-C26IL4
FGF21-C26
FGF21-C26IL4
Gene / Group
3
2
1
0
−1

Figure 24. Preliminary analysis of the tumor microenvironment at endpoint via single nuclei RNA sequencing. (*A*) UMAP visualization of cell types in the tumor. (*B*) Proportions of significantly different cell types in the tumor across groups. (*C*) Relative abundance of M1 and M2 macrophages in the tumor. (*D*) Heatmap of differential gene expression between groups across several cell types in the tumor. Experimental groups: C26 tumor-bearing mice (C26; n=8), IL4-treated C26 tumor-bearing mice (C26+IL4; n=8).

5.6. IL4 administration improves muscle mitochondrial homeostasis and energy metabolism

Modulations of the TME were reported to reflect a metabolic rewiring in the tumor[94], but also in the host[95]. Along this line, experiments were set up to investigate whether the effects exerted by IL4 on both the TME and the spleen immunophenotype could be paralleled by improved energy metabolism in the skeletal muscle, one of the tissues mainly affected by cachexia.

At EEP, the C26 hosts displayed a significant reduction in the skeletal muscle protein levels of the electron transport chain component cytochrome c, the master regulator of mitochondrial biogenesis PGC-1α, and the outer membrane protein import channel TOMM20 as compared to control and C26+IL4 groups. Conversely, the protein levels of the mitophagy regulator BNIP3 were significantly increased in the C26 tumor-bearing mice as compared to controls and were markedly reduced by IL4 treatment. Notably, this pattern was absent at ETP, where mitochondrial homeostasis markers remained comparable to control values and were not modulated by IL4 (Figure 25A-D).

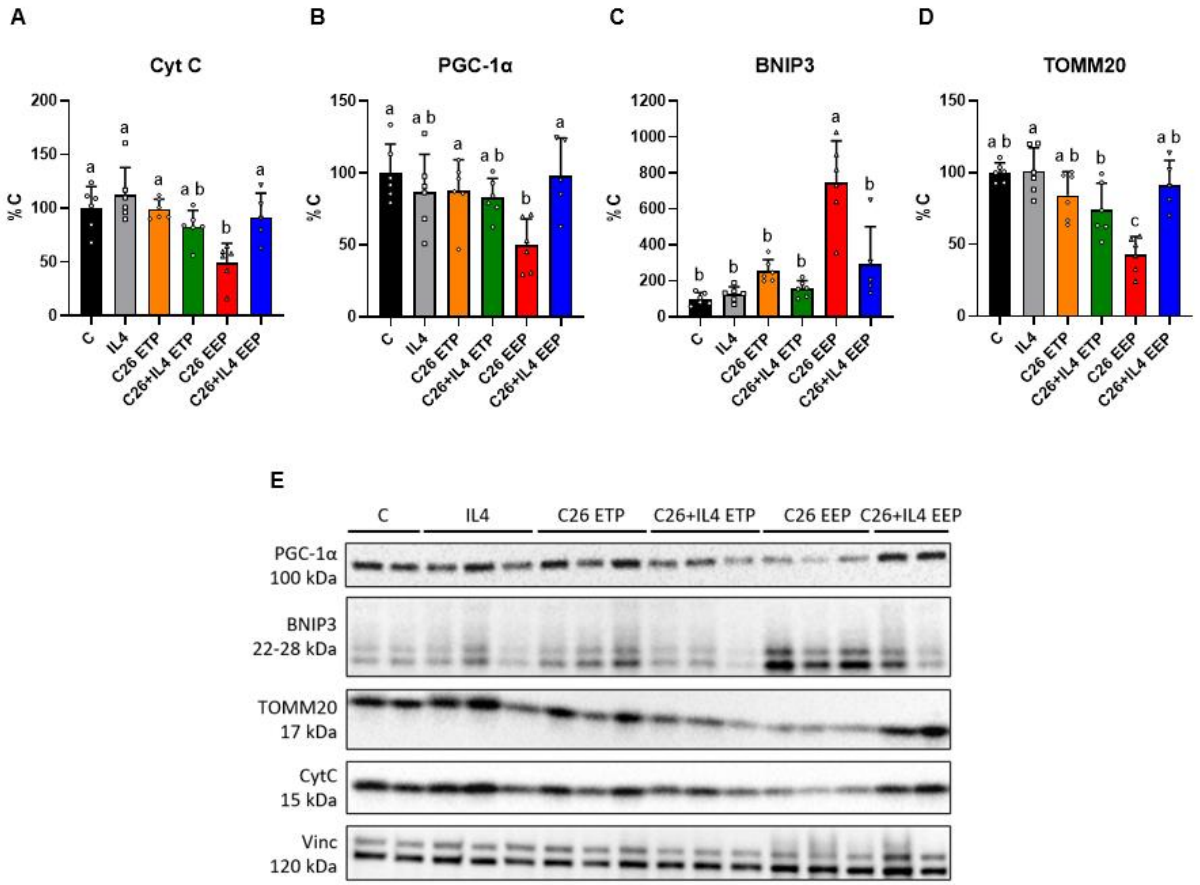

Figure 25. Skeletal muscle protein levels of mitochondrial markers at different time points. (*A-D*) Protein levels of cytochrome c (Cyt C)(*A*), peroxisome proliferator-activated receptor-gamma coactivator 1 alpha (PGC-1α)(*B*), Bcl-2 interacting protein 3 (BNIP3)(*C*) and translocase of outer mitochondrial membrane 20 (TOMM20)(*D*). (*E*) Representative western blotting bands. Protein levels normalized by vinculin and represented as percentage of control values. Experimental groups: control (C; n=6), IL4-treated control (IL4; n=6), C26 tumor-bearing mice sacrificed at ETP (C26 ETP; n=6), IL4-treated C26 tumor-bearing mice sacrificed at ETP (C26+IL4 ETP; n=6), C26 tumor-bearing mice sacrificed at EEP (C26 EEP; n=6), IL4-treated C26 tumor-bearing mice sacrificed at EEP (C26+IL4 EEP; n=5). Data expressed as mean ± standard deviation. Significant differences ($p < 0.05$) represented by different letters.

The improved mitochondrial health induced by IL4 treatment in the muscle of the C26 hosts at EEP suggested a potential restoration of energy metabolism. This hypothesis was tested by assessing the activity of hexokinase II, a key enzyme involved in glycolysis, and the protein levels of the oxidative phosphorylation (OXPHOS) complexes (I-V). Both hexokinase II

activity and OXPHOS complexes protein levels were reduced in the skeletal muscle of the C26 hosts at EEP and were restored by IL4. By contrast, in the C26 hosts at ETP, hexokinase II activity was comparable to controls and was unaltered by IL4, while the protein levels of OXPHOS complexes I, II, and IV were higher than in control mice, an increase that was partially prevented by IL4 (Figure 26A-F).

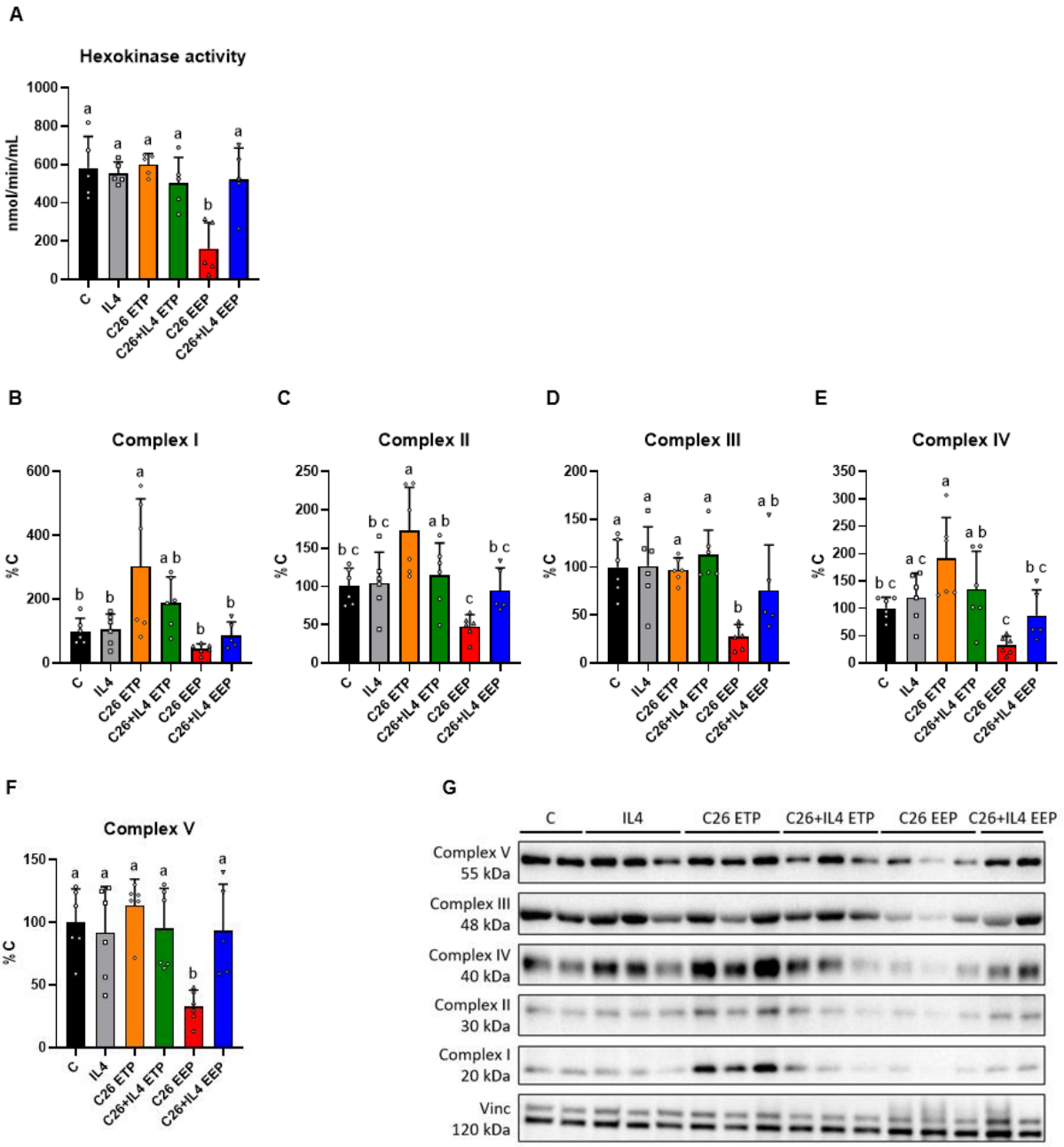

Figure 26. Evaluation of energy metabolism in the skeletal muscle at different time points. (*A*) Enzymatic activity of hexokinase expressed in nmol/min/mL.

Experimental groups: control (C; n=5), IL4-treated control (IL4; n=5), C26 tumor-bearing mice sacrificed at ETP (C26 ETP; n=5), IL4-treated C26 tumor-bearing mice sacrificed at ETP (C26+IL4 ETP; n=5), C26 tumor-bearing mice sacrificed at EEP (C26 EEP; n=5), IL4-treated C26 tumor-bearing mice sacrificed at EEP (C26+IL4 EEP; n=5). (*B-F*) Protein levels of oxidative phosphorylation (OXPHOS) complexes I-V. (*G*) Representative western blotting bands. Protein levels normalized by vinculin and represented as percentage of control values. Experimental groups: C (n=6), IL4 (n=6), C26 ETP (n=6), C26+IL4 ETP (n=6), C26 EEP (n=6), C26+IL4 EEP (n=5). Data expressed as mean ± standard deviation. Significant differences ($p < 0.05$) represented by different letters.

Consistently with the decreased availability of OXPHOS complexes, the skeletal muscle of the C26 hosts at EEP exhibited a reduced energy production capacity. Specifically, at EEP, the oxygen consumption rate (OCR) related to OXPHOS CI+CII and ETS CI+CII phases was decreased in the C26 hosts as compared to controls, but was fully restored by IL4 administration (Figure 27A). At ETP, a non-significant trend towards reduced OCR in the C26 hosts was observed as well, which, however, was not modulated by IL4 (Figure 27B).

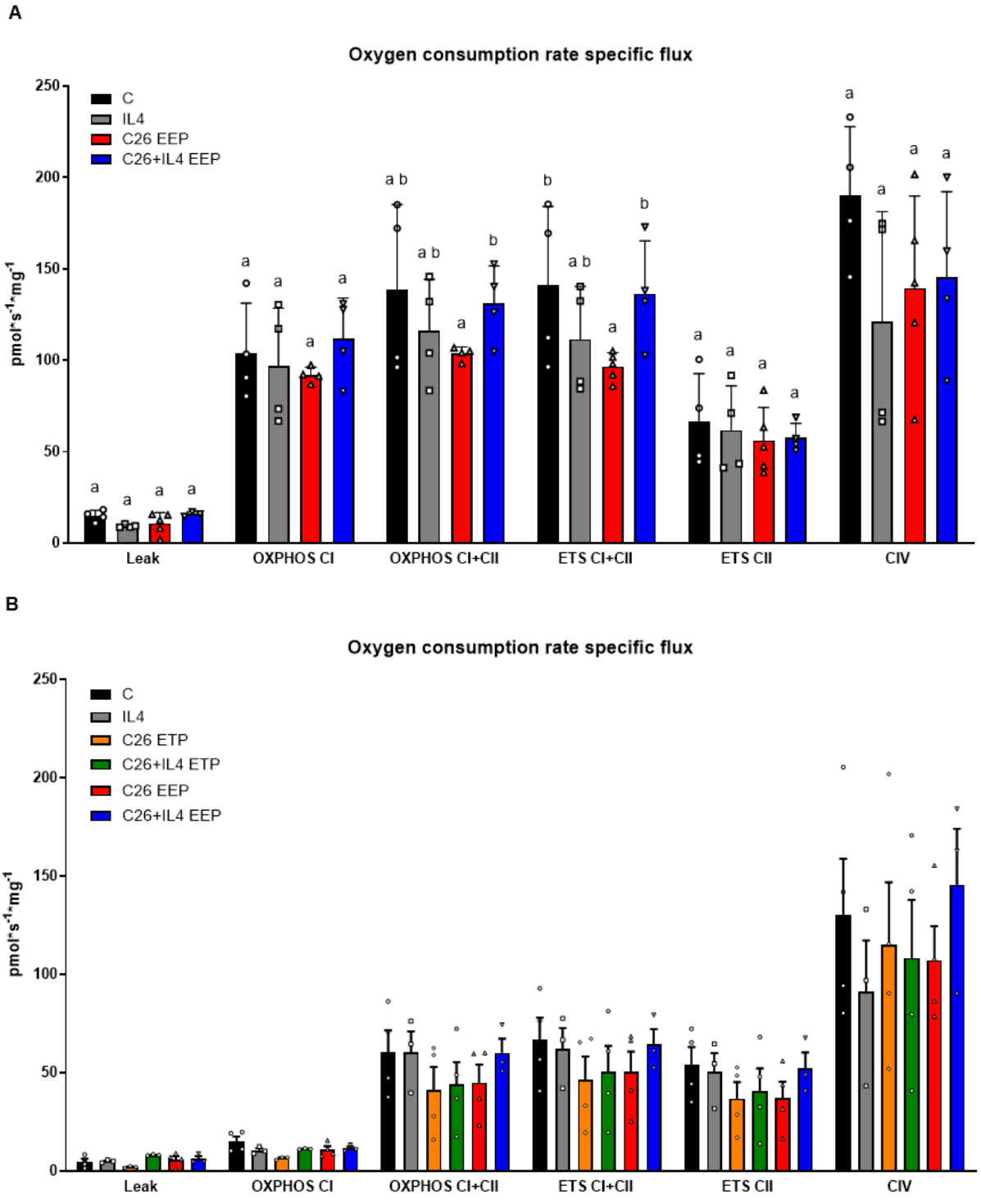

Figure 27. Skeletal muscle mitochondrial oxygen consumption rate (OCR) at different time points. (*A*) OCR specific flux performed on fresh tissue, normalized by tissue weight and expressed in pmol×s^{-1}×mg^{-1}. Experimental groups: control (C; n=4), IL4-treated control (IL4; n=4), C26 tumor-bearing mice sacrificed at EEP (C26 EEP; n=5), IL4-treated C26 tumor-bearing mice sacrificed at EEP (C26+IL4 EEP; n=5). (*B*) OCR specific flux performed on cryopreserved tissue, normalized

by tissue weight and expressed in pmol×s^{-1}×mg^{-1}. Experimental groups: control (C; n=4), IL4-treated control (IL4; n=3), C26 tumor-bearing mice sacrificed at ETP (C26 ETP; n=4), IL4-treated C26 tumor-bearing mice sacrificed at ETP (C26+IL4 ETP; n=4), C26 tumor-bearing mice sacrificed at EEP (C26 EEP; n=4), IL4-treated C26 tumor-bearing mice sacrificed at EEP (C26+IL4 EEP; n=3). Data expressed as mean ± standard deviation. Significant differences ($p < 0.05$) represented by different letters.

5.7. IL4 treatment impinges on C26-induced metabolome and lipidome alterations in the skeletal muscle

Metabolome

At EEP, the skeletal muscle metabolic signature showed a profound dysregulation caused by the tumor and a partial restoration exerted by IL4. The metabolic profile of the C26 tumor-bearing mice was markedly different from that of controls, highlighting the disruption of muscle homeostasis across several pathways. Indeed, the heatmap in Figure 28A shows that the top 50 significantly changed metabolites were clearly differentially modulated in controls and in the C26 hosts. In the C26+IL4 EEP group, a partial reversion of such C26-induced dysregulation could be observed, with many modulated metabolites being restored towards control levels. This broad-spectrum rescue involved the normalization of metabolites central to multiple physiological processes, such as muscle contraction, redox balance, inflammation, and cell death, and metabolic pathways, including energy, amino acid, nucleotide, purine, and polyamine metabolism (Figure 28A). In this general pattern of partial normalization induced by the cytokine, the increase of uric acid, a product of purine catabolism and a marker of xanthine oxidase-driven oxidative stress, occurring in the C26 hosts was unaffected by IL4 administration (Figure 28A).

Notably, many immunometabolites were also significantly modulated. Some of them, such as L-tryptophan, indole, and L-arginine, were accumulated, while glutathione was depleted in both IL4-treated and untreated C26 hosts as compared to controls. On the other side, indolepyruvate, hypoxanthine, sphingosine 1-phosphate, putrescine, and spermidine showed an IL4-dependent effect, being accumulated in the C26 EEP group, while reduced towards control levels in the

C26+IL4 EEP group. Finally, citrulline only showed an IL4-dependent reduction among controls (Figure 28A).

Regarding energy metabolism, many intermediates of glycolysis, tricarboxylic acid (TCA) cycle, and carnitine metabolism were significantly modulated across groups (Figure 28B). In line with the alterations in mitochondrial homeostasis and OCR, a clear signature of TCA flux disruption was observed in the C26 hosts, as evidenced by the unaltered succinic acid levels alongside fumaric and malic acid depletion. This metabolic dysregulation was prevented by IL4, as the levels of those TCA cycle intermediates remained close to control values in the C26+IL4 EEP group (Figure 28C-E). Furthermore, a depletion in acylcarnitines, ranging from octanoylcarnitine to 3-hydroxylinoleoylcarnitine (acyl-C18:2-OH), could be observed in C26 hosts, an effect that was only partially rescued by IL4 treatment. Specifically, the cytokine induced a minor replenishment restricted to a few specific acylcarnitines, including octanoylcarnitine, tetradecenoylcarnitine, hexadecenoylcarnitine, O-octadecenoylcarnitine, and 3-hydroxylinoleoylcarnitine (acyl-C18:2-OH). An opposite effect was observed for tiglylcarnitine (acyl-C5:1), which was significantly accumulated in the C26 EEP group, but reduced towards control levels in the C26+IL4 EEP group (Figure 28B).

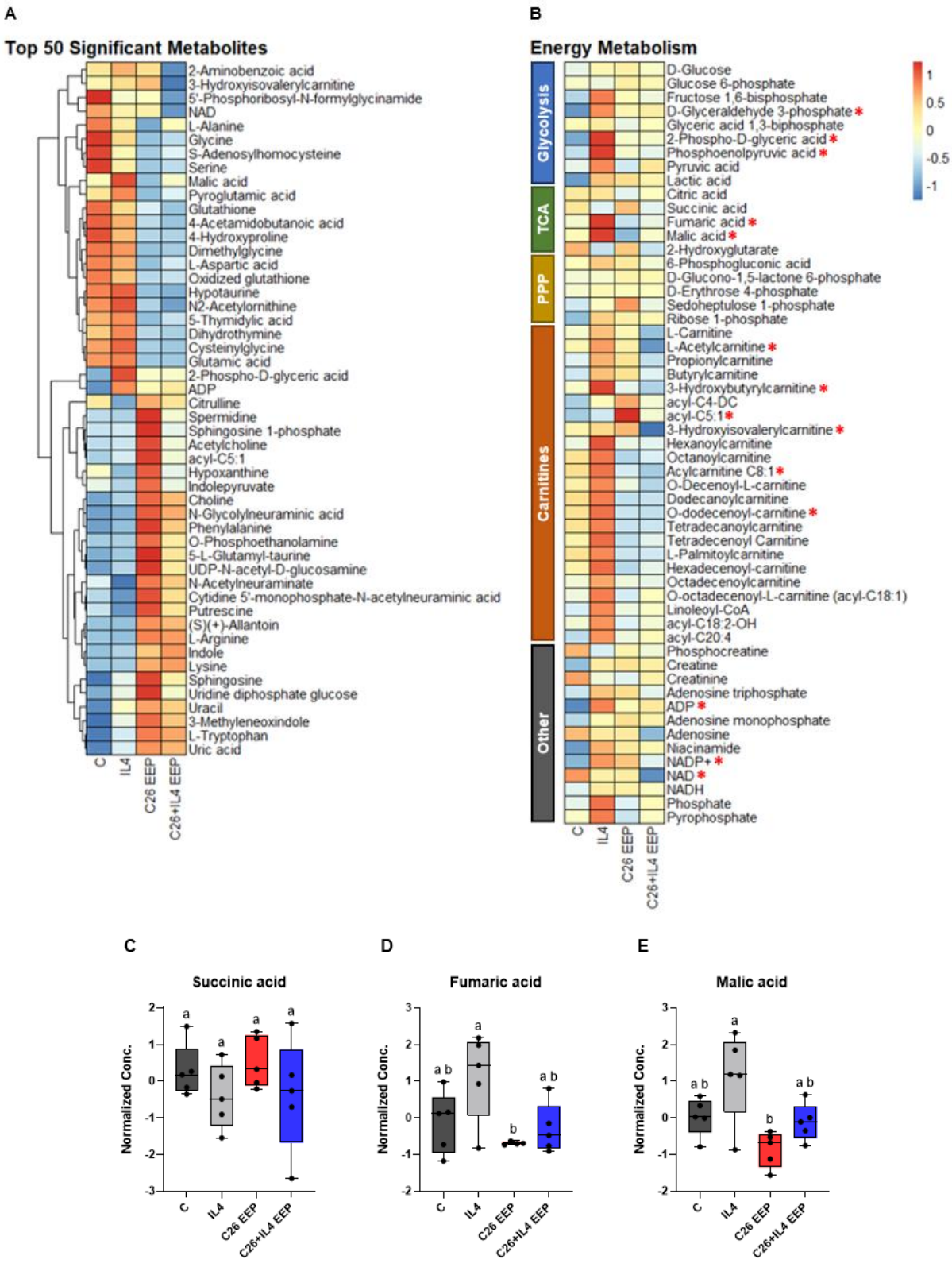

Figure 28. Skeletal muscle metabolomic analysis at endpoint. (*A*) Heatmap of the top 50 significantly modulated metabolites. (*B*) Heatmap of energy-associated metabolites, grouped by pathway; significant metabolites (FDR < 0.1 and p < 0.05) are marked by a red asterisk. (*C-E*) Normalized concentrations of succinic acid (*C*),

fumaric acid (*D*), and malic acid (*E*), represented as boxplots. Experimental groups: control (C; n=5), IL4-treated control (IL4; n=5), C26 tumor-bearing mice sacrificed at EEP (C26 EEP; n=5), IL4-treated C26 tumor-bearing mice sacrificed at EEP (C26+IL4 EEP; n=5). Significant differences ($p < 0.05$) represented by different letters. Abbreviations: pentose phosphate pathway (PPP), tricarboxylic acid cycle (TCA).

Lipidome

The lipidomic profile of the skeletal muscle was deeply changed in the presence of the tumor at EEP. This effect was markedly rescued by IL4 treatment. Accordingly, the heatmap showing the top 50 most significant lipids highlighted a strong separation between control and C26 tumor-bearing mice, with the C26+IL4 EEP group shifting towards the control profile (Figure 29A). A similar pattern emerged when lipids were grouped by class, with IL4 partially reversing cancer-induced lipidome alterations (Figure 29B). In detail, the skeletal muscle of the C26 tumor-bearing mice featured the accumulation of cholesterol, cholesteryl esters, phosphatidylethanolamines, phosphatidylserines, lysophospholipids, ceramides, sphingosines, and sphingosine-1-phosphate, modulations that were partially reversed by IL4. As for triglycerides and diglycerides, however, the significant C26-induced depletion observed was not corrected by IL4. Finally, monoglycerides and fatty acids remained comparable across all groups (Figure 30).

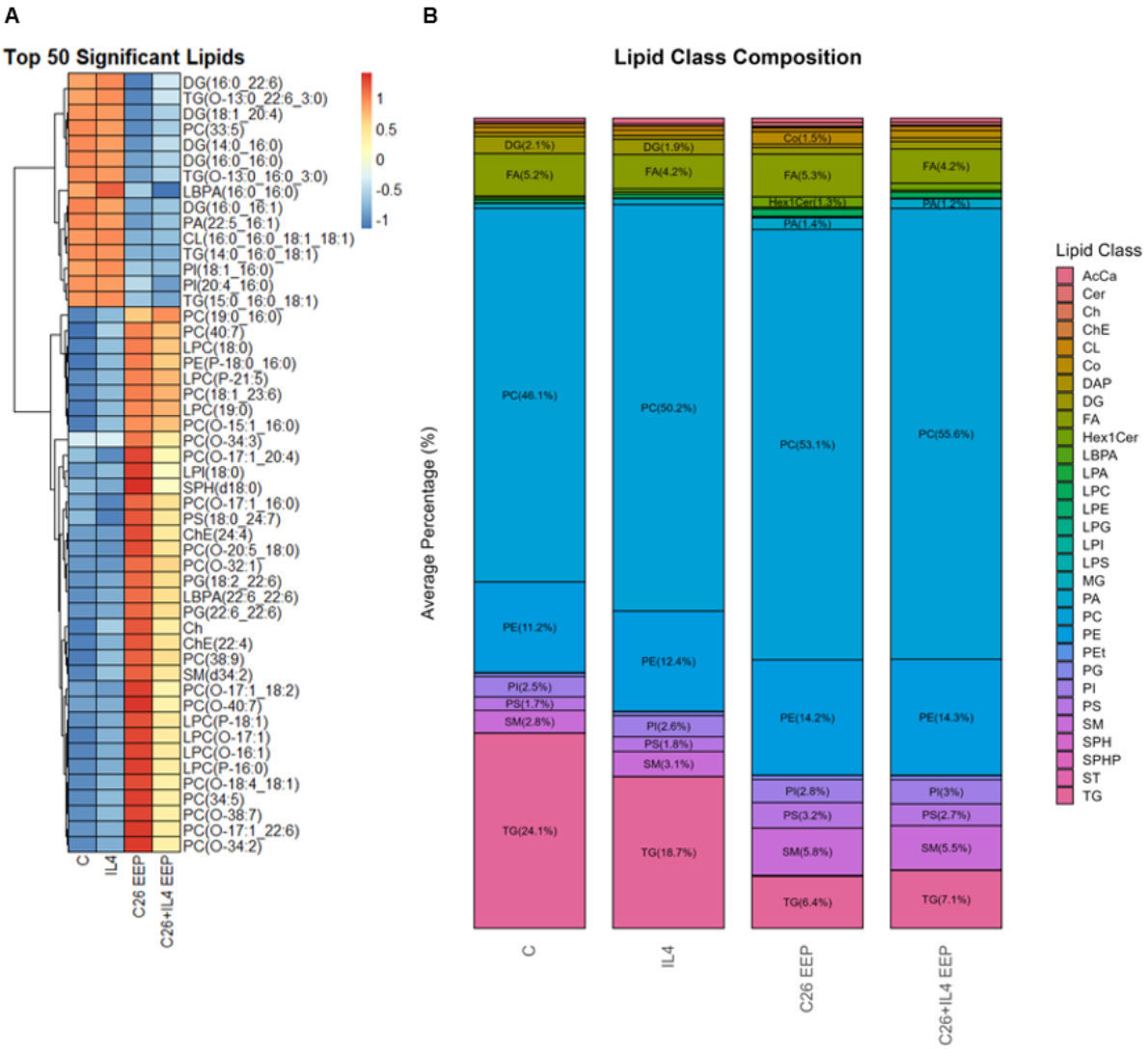

Figure 29. Skeletal muscle lipidomic analysis at endpoint. (*A*) Heatmap of the top 50 significantly modulated lipids. (*B*) Lipid class composition analysis. Lipid classes expressed as percentage of the total lipids identified. Experimental groups: control (C; n=5), IL4-treated control (IL4; n=5), C26 tumor-bearing mice sacrificed at EEP (C26 EEP; n=5), IL4-treated C26 tumor-bearing mice sacrificed at EEP (C26+IL4 EEP; n=5). Abbreviations: acylcarnitine (AcCa), ceramide (Cer), cholesterol (Ch), cholesteryl ester (ChE), cardiolipin (CL), coenzyme (Co), dihydroxyacetone phosphate (DAP), diglyceride (DG), fatty acid (FA), hexosylceramide (Hex1Cer), lysobisphosphatidic acid (LBPA), lysophosphatidic acid (LPA), lysophosphatidylcholine (LPC), lysophosphatidylethanolamine (LPE), lysophosphatidylglycerol (LPG), lysophosphatidylinositol (LPI), lysophosphatidylserine (LPS), monoglyceride (MG), phosphatidic acid (PA), phosphatidylcholine (PC), phosphatidylethanolamine (PE), phosphatidylethanol

(PEt), phosphatidylglycerol (PG), phosphatidylinositol (PI), phosphatidylserine (PS), sphingomyelin (SM), sphingosine (SPH), sphingosine 1-phosphate (SPHP), sterol (ST), triglyceride (TG).

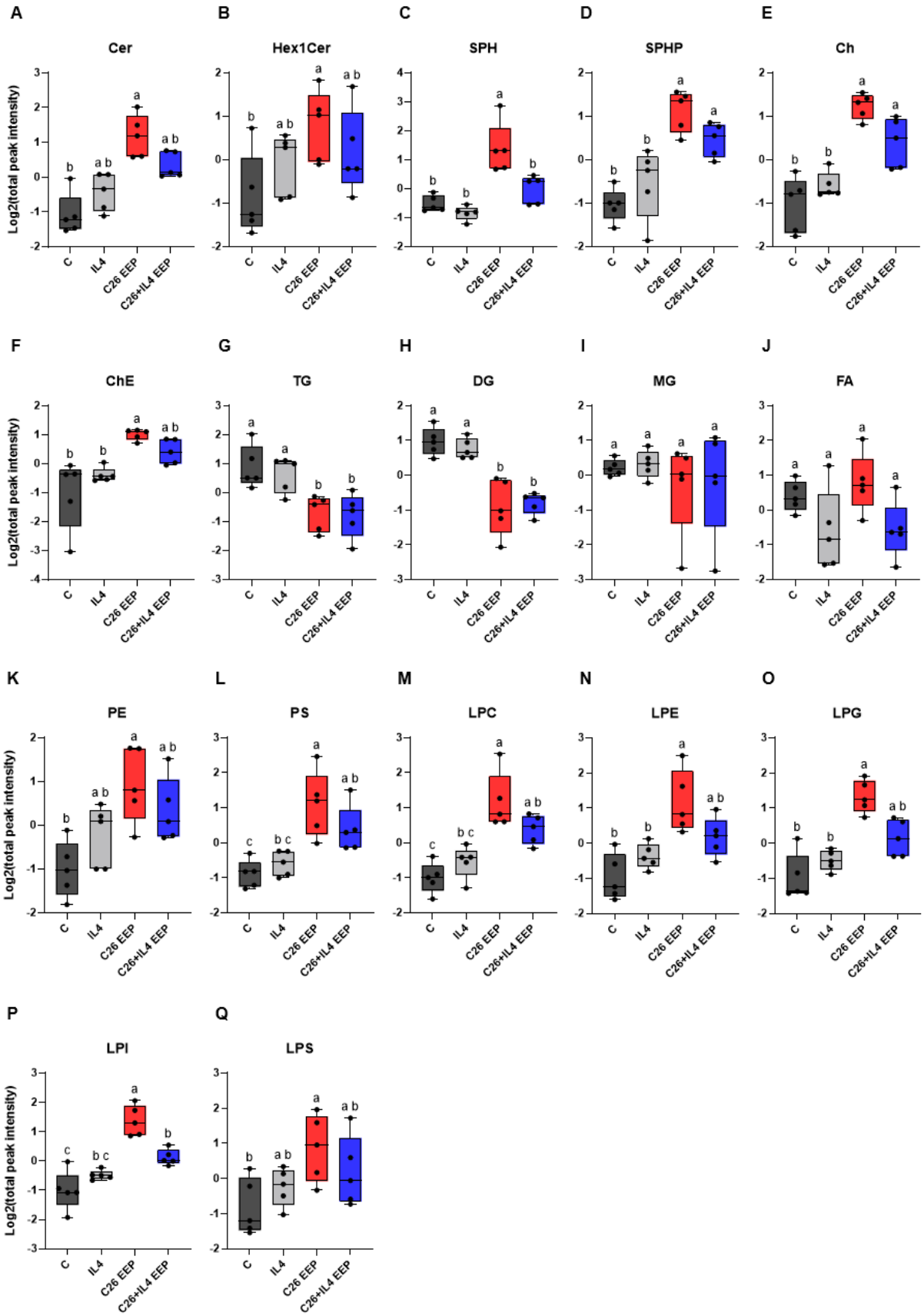

Figure 30. Skeletal muscle lipidomic analysis at endpoint. (*A*-*Q*) Lipid class levels expressed as base 2 logarithm of the total peak intensities and represented as

boxplots. Experimental groups: control (C; n=5), IL4-treated control (IL4; n=5), C26 tumor-bearing mice sacrificed at EEP (C26 EEP; n=5), IL4-treated C26 tumor-bearing mice sacrificed at EEP (C26+IL4 EEP; n=5). Significant differences ($p < 0.05$) represented by different letters. Abbreviations: ceramide (Cer), cholesterol (Ch), cholesteryl ester (ChE), diglyceride (DG), fatty acid (FA), hexosylceramide (Hex1Cer), lysophosphatidylcholine (LPC), lysophosphatidylethanolamine (LPE), lysophosphatidylglycerol (LPG), lysophosphatidylinositol (LPI), lysophosphatidylserine (LPS), monoglyceride (MG), phosphatidylethanolamine (PE), phosphatidylserine (PS), sphingosine (SPH), sphingosine 1-phosphate (SPHP), triglyceride (TG).

5.8. IL4 exerts changes in both metabolomic and lipidomic profile in the liver of the C26 hosts

Metabolome

Alongside the skeletal muscle, at EEP, the liver metabolome in the C26 tumor-bearing mice was strongly affected as well, with IL4 inducing a partial rescue. The heatmap showing the top 50 most significant metabolites highlighted markedly different profiles between the C26 EEP group and controls, with the C26+IL4 EEP group shifting towards the control profile. In particular, intermediates of amino acid, nucleotide, bile acid, sphingolipid, polyamine, neurotransmitter, and vitamin B6 metabolism showed a cancer-induced dysregulation that was partially restored to control levels by IL4 (Figure 31A). Cancer-induced alterations of the hepatic metabolome impacted energy metabolism as well. Indeed, many intermediates of glycolysis, TCA cycle, pentose phosphate pathway and carnitine metabolism were significantly modulated across groups (Figure 31B). Specifically, in both IL4-treated and untreated C26 hosts, a depletion in hepatic glucose, glyceraldehyde 3-phosphate and lactic acid was observed. Conversely, several TCA cycle and pentose phosphate pathway intermediates were found to be markedly accumulated in the C26 hosts, an effect that was partially corrected by IL4 treatment. An opposite pattern was observed for phosphoribosyl pyrophosphate (5-phospho-alpha-D-ribose 1-diphosphate), which was depleted in the C26 EEP group and restored in the C26+IL4 EEP group. Interestingly, an accumulation of medium- and long-chain acylcarnitines was observed in both IL4-treated groups (Figure 31B).

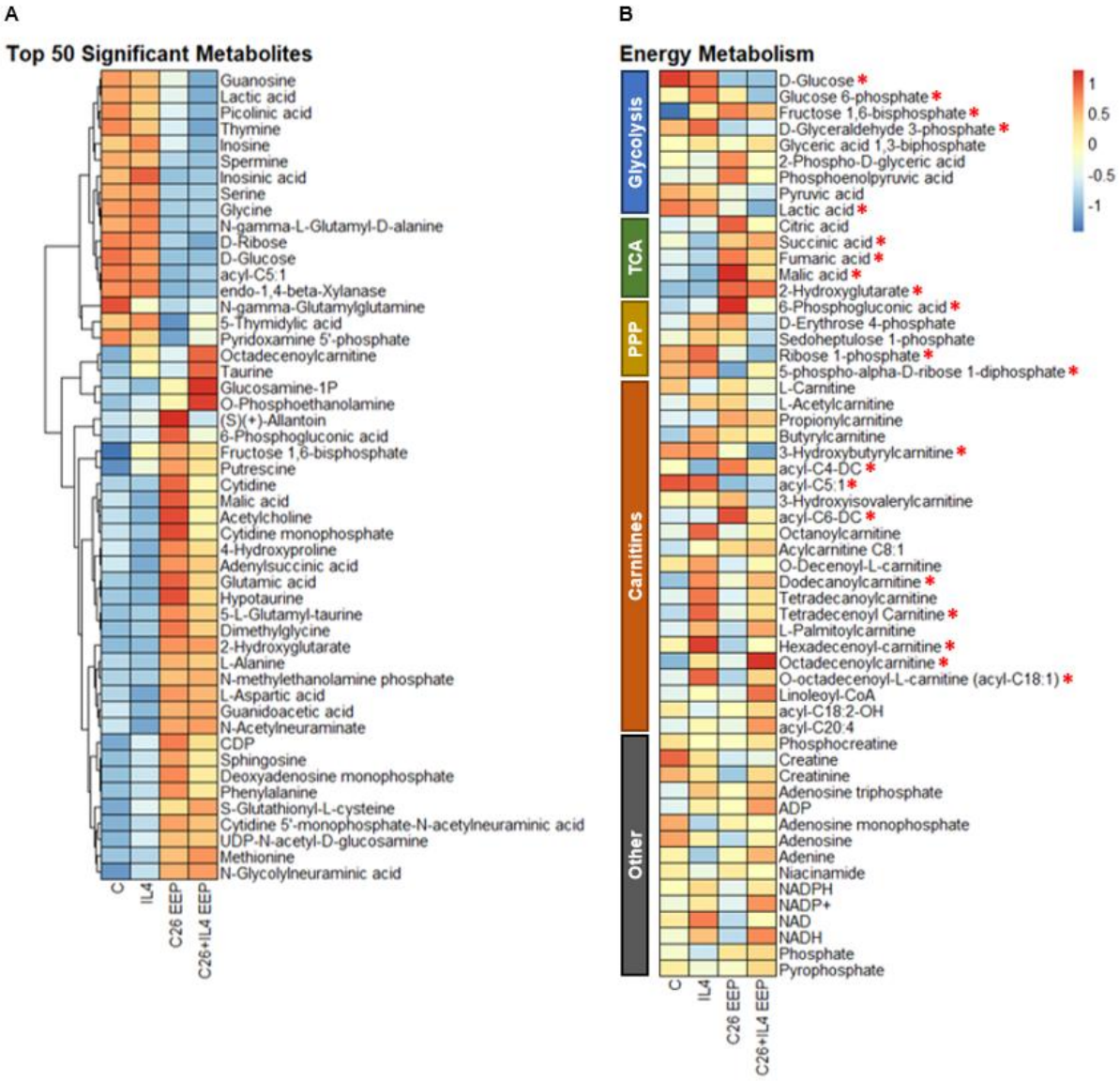

Figure 31. Liver metabolomic analysis at endpoint. (*A*) Heatmap of the top 50 significantly modulated metabolites. (*B*) Heatmap of energy-associated metabolites, grouped by pathway; significant metabolites (FDR < 0.1 and p < 0.05) are marked by a red asterisk. Experimental groups: control (C; n=5), IL4-treated control (IL4; n=5), C26 tumor-bearing mice sacrificed at EEP (C26 EEP; n=5), IL4-treated C26 tumor-bearing mice sacrificed at EEP (C26+IL4 EEP; n=5). Abbreviations: pentose phosphate pathway (PPP), tricarboxylic acid cycle (TCA).

Lipidome

At EEP, marked tumor-driven alterations were also evident in the liver lipidome, as evidenced by the robust separation between controls and C26 hosts in the top 50 significant lipids heatmap (Figure 32A). Although to a lesser extent compared to the skeletal muscle, in the liver, IL4 administration partially restored several dysregulated lipid classes in the C26 hosts to control values (Figure 32B). Specifically, ceramides and lysophosphatidic acid were significantly depleted in the C26 EEP group as compared to controls, but were partially restored by IL4. Conversely, hexosylceramides, sphingosines, sphingosine-1-phosphate, cholesterol, cholesteryl esters, and phosphatidylinositol phosphates showed an opposite pattern, consisting of a C26-induced accumulation followed by a partial reduction induced by IL4. As for energy-associated lipids, triglycerides were significantly depleted in the C26 EEP group, whereas a trend towards increase was observed in the C26+IL4 EEP group. By contrast, monoglycerides were markedly accumulated in both the IL4-treated and untreated C26 tumor-bearing mice. Finally, diglycerides and fatty acids were unchanged across all groups (Figure 33).

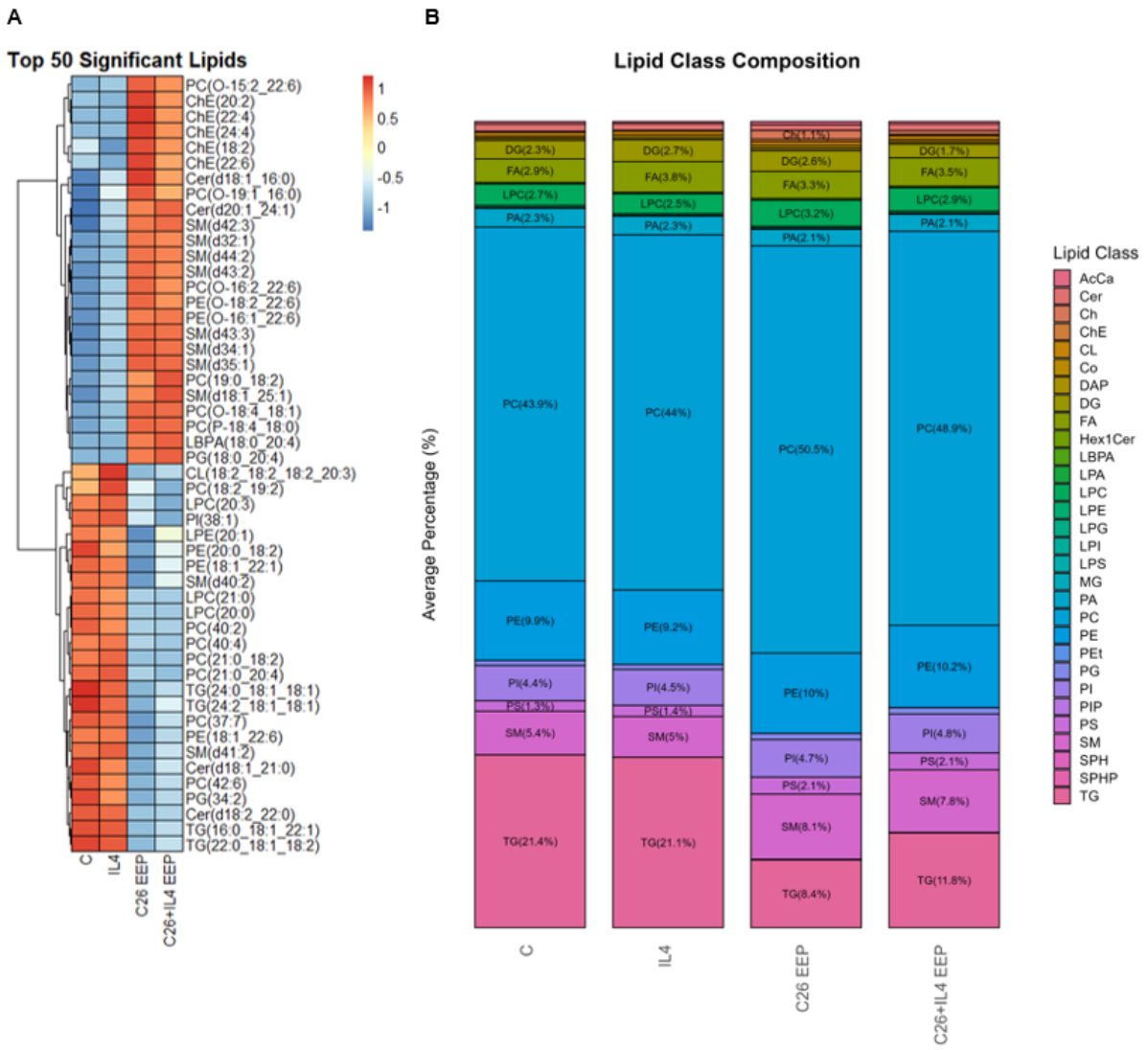

Figure 32. Liver lipidomic analysis at endpoint. (*A*) Heatmap of the top 50 significantly modulated lipids. (*B*) Lipid class composition analysis. Lipid classes expressed as percentage of the total lipids identified. Experimental groups: control (C; n=5), IL4-treated control (IL4; n=5), C26 tumor-bearing mice sacrificed at EEP (C26 EEP; n=5), IL4-treated C26 tumor-bearing mice sacrificed at EEP (C26+IL4 EEP; n=5). Abbreviations: acylcarnitine (AcCa), ceramide (Cer), cholesterol (Ch), cholesteryl ester (ChE), cardiolipin (CL), coenzyme (Co), dihydroxyacetone phosphate (DAP), diglyceride (DG), fatty acid (FA), hexosylceramide (Hex1Cer), lysobisphosphatidic acid (LBPA), lysophosphatidic acid (LPA), lysophosphatidylcholine (LPC), lysophosphatidylethanolamine (LPE), lysophosphatidylglycerol (LPG), lysophosphatidylinositol (LPI), lysophosphatidylserine (LPS), monoglyceride (MG), phosphatidic acid (PA), phosphatidylcholine (PC), phosphatidylethanolamine (PE), phosphatidylethanol

(PEt), phosphatidylglycerol (PG), phosphatidylinositol (PI), phosphatidylinositol phosphate (PIP), phosphatidylserine (PS), sphingomyelin (SM), sphingosine (SPH), sphingosine 1-phosphate (SPHP), triglyceride (TG).

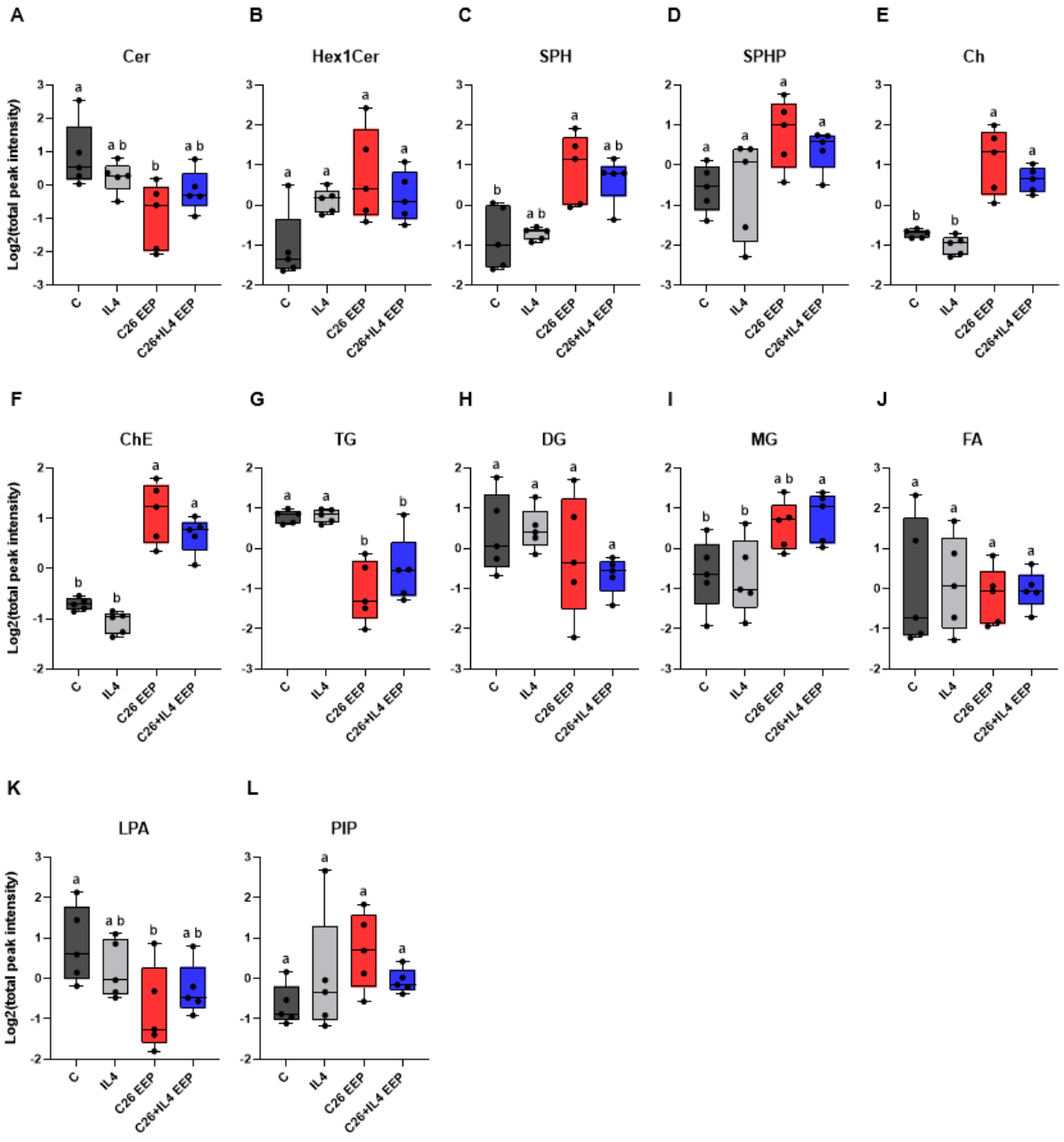

Figure 33. Liver lipidomic analysis at endpoint. (*A*-*L*) Lipid class levels expressed as base 2 logarithm of the total peak intensities and represented as boxplots. Experimental groups: control (C; n=5), IL4-treated control (IL4; n=5), C26 tumor-bearing mice sacrificed at EEP (C26 EEP; n=5), IL4-treated C26 tumor-bearing

mice sacrificed at EEP (C26+IL4 EEP; n=5). Significant differences ($p < 0.05$) represented by different letters. Abbreviations: ceramide (Cer), cholesterol (Ch), cholesteryl ester (ChE), diglyceride (DG), fatty acid (FA), hexosylceramide (Hex1Cer), lysophosphatidic acid (LPA), monoglyceride (MG), phosphatidylinositol phosphate (PIP), sphingosine (SPH), sphingosine 1-phosphate (SPHP), triglyceride (TG).

5.9. Targeting hyperuricemia with febuxostat does not counteract C26-induced cachexia

Since hyperuricemia and xanthine oxidase (XO) activity are established contributors to skeletal muscle inflammation, oxidative stress, and ultimately, muscle wasting[37,96–98], the observation that IL4 treatment failed to correct elevated muscle uric acid levels in the C26 hosts provided a strong rationale for targeting this pathway directly. Although previous studies have tested this strategy, the overall results are inconclusive and none were obtained in the C26 model[45,98–100]. Therefore, C26 tumor-bearing mice were treated with the XO inhibitor febuxostat (FBX), in line with previous work[98]. However, this intervention failed to prevent the significant loss of body weight observed in untreated tumor hosts (Figure 34A, B). Similar trends were observed for food intake, with a comparable reduction in the cumulative calorie intake indicating the onset of anorexia in both FBX-treated and untreated C26 hosts (Figure 34C). Accordingly, both FBX-treated and untreated C26 tumor-bearing mice showed a non-significant trend towards reduced skeletal muscle mass as compared to control, with a slightly more pronounced reduction observed in the C26+FBX group (Figure 34D-F). By contrast, the specific force of the extensor digitorum longus (EDL) muscle was significantly reduced only in the untreated C26 hosts as compared to control, while being preserved in the C26+FBX group (Figure 34G). White adipose tissue mass was reduced in both FBX-treated and untreated C26 tumor-bearing mice as compared to control, although the reduction was statistically significant only in the C26+FBX group (Figure 34H). A significant increase in spleen mass as compared to control was evident in both the C26 and C26+FBX groups, and similar trends were observed for liver mass (Figure 34I, J). Tumor growth was not altered by FBX treatment, as tumor mass was comparable between FBX-treated and untreated C26 hosts (Figure 34K).

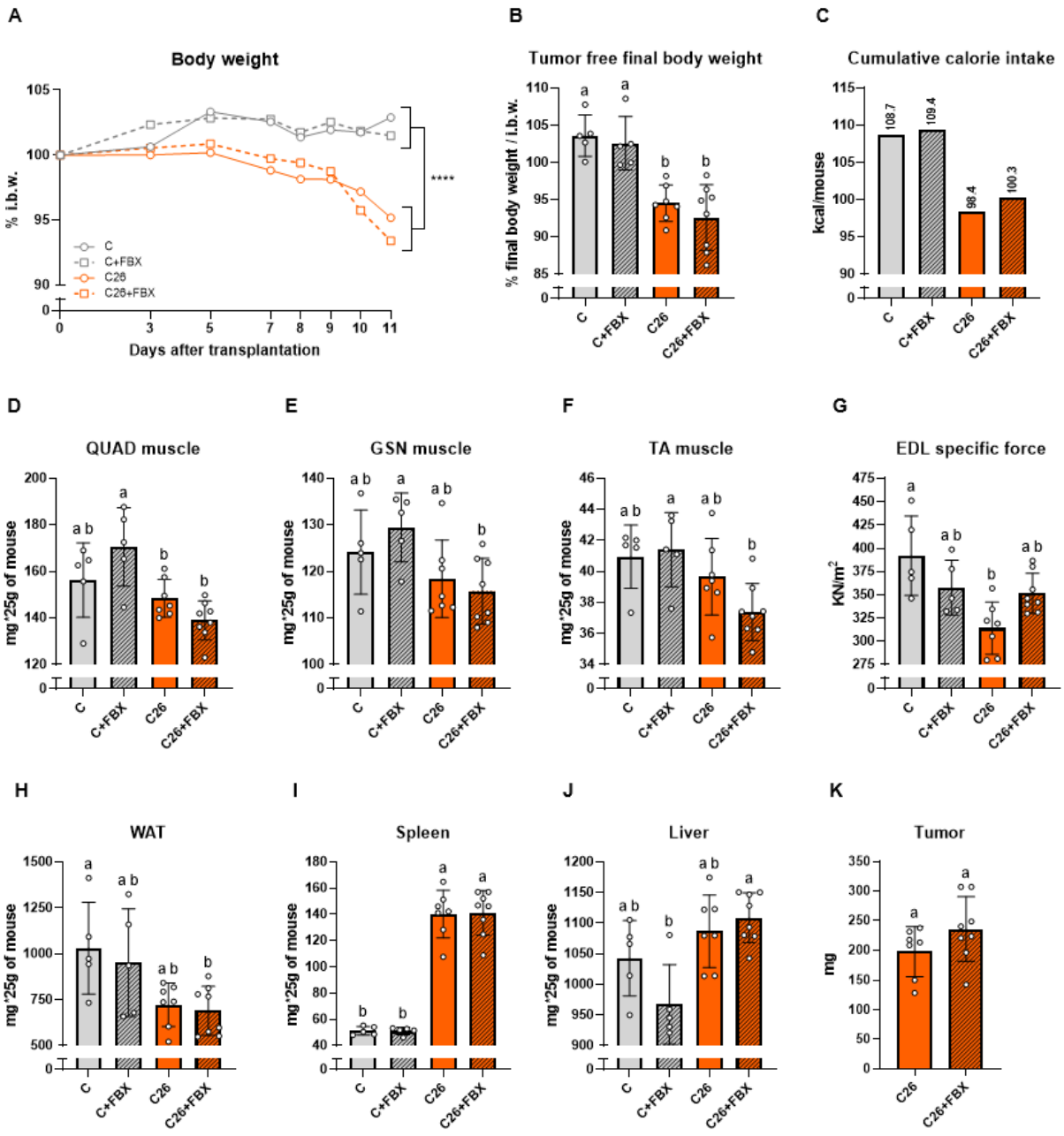

Figure 34. Effects of febuxostat (FBX) treatment on the C26 tumor-bearing mice. (A) Body weight kinetic curve. Body weight expressed as percentage of the initial body weight (i.b.w.). (*B*) Tumor free final body weight expressed as percentage of the i.b.w. (*C*) Cumulative calorie intake measured between day 0 and day 10 after tumor implantation, and expressed in kcal/mouse. (*D-E, H-J*) Quadriceps (QUAD) muscle weight (*D*), gastrocnemius (GSN) muscle weight (*E*), tibialis anterior (TA) muscle weight (*F*), white adipose tissue (WAT) weight (*H*), spleen weight (*I*), and liver weight (*J*), normalized to 25g of mouse body weight and expressed in mg. (*G*) Extensor digitorum longus (EDL) muscle *ex vivo* specific force, measured at 150 Hz and expressed as KN/m^2. (*K*) Tumor weight expressed in mg. Experimental

groups: control (C; n=5), FBX-treated control (C+FBX; n=5), C26 tumor-bearing mice (C26; n=7), FBX-treated C26 tumor-bearing mice (C26+FBX; n=8). Data expressed as mean ± standard deviation, except for food intake. Significant differences ($p < 0.05$) represented by different letters, except for body weight kinetic curve (****$p < 0.0001$).

FBX treatment was effective in reducing XO activity in the skeletal muscle. While XO activity showed a trend to increase in the C26 group as compared to control, FBX treatment significantly reduced it, restoring it to control levels in the C26+FBX group. A significant reduction in XO activity was also evident in FBX-treated versus untreated control mice (Figure 35A). A similar pattern was observed for the circulating uric acid levels. Specifically, a trend to increase was observed in the C26 group compared to control, while trends towards reduction were observed in both FBX-treated control and C26 tumor-bearing mice as compared to their respective untreated counterparts (Figure 35B).

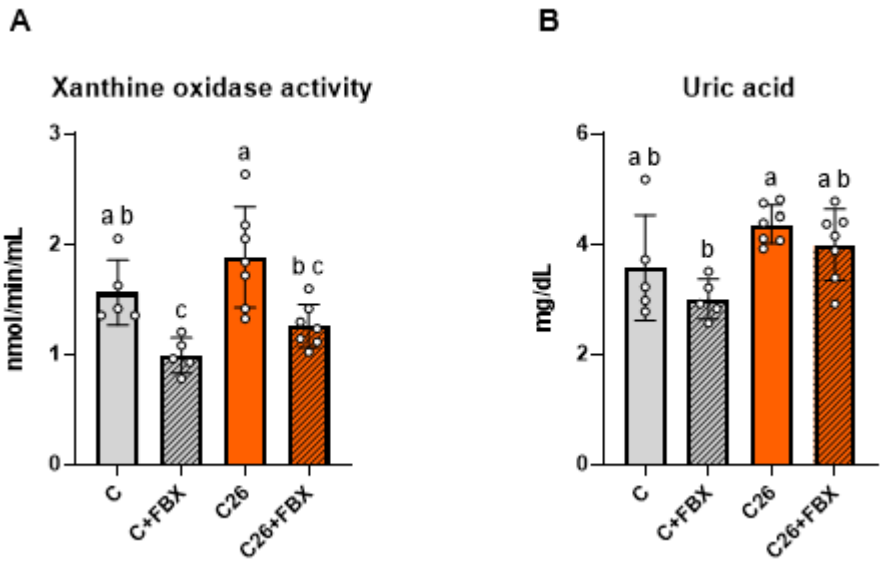

Figure 35. Assessment of febuxostat-dependent xanthine oxidase inhibition. (*A*) Enzymatic activity of xanthine oxidase in the skeletal muscle, expressed in nmol/min/mL. (*B*) Plasma uric acid levels expressed in mg/dL. Experimental groups: control (C; n=5), FBX-treated control (C+FBX; n=5), C26 tumor-bearing mice (C26; n=7), FBX-treated C26 tumor-bearing mice (C26+FBX; n=7). Data

expressed as mean ± standard deviation. Significant differences ($p < 0.05$) represented by different letters.

5.10. Febuxostat modulates inflammatory and proteostasis signaling in the skeletal muscle of C26 hosts

Xanthine oxidase hyperactivity is associated with hyperuricemia and oxidative stress, which can promote inflammation and catabolism in the skeletal muscle. To investigate whether the protective effect of FBX on muscle force was linked to these pathways, markers of inflammation and proteostasis were evaluated at protein level. The ratios of phosphorylated to total NF-κB (p-NF-κB/NF-κB) and STAT3 (p-STAT3/STAT3) were significantly increased in the skeletal muscle of untreated C26 tumor-bearing mice as compared to control. FBX treatment significantly counteracted the tumor-induced increase in both ratios (Figure 36A, B). MuRF-1 protein levels were unaltered across groups, although trends to increase were observed in FBX-treated controls and in both FBX-treated and untreated C26 hosts as compared to untreated control mice (Figure 36C). In parallel, the total ubiquitin signal showed a trend to increase in the C26 group as compared to control. Such an increase was counteracted by FBX treatment, as the levels of ubiquitin were significantly reduced in the C26+FBX group as compared to its untreated counterpart (Figure 36D).

Regarding the anabolic signaling, the p-Akt/Akt ratio did not show significant alterations across groups. However, total Akt protein levels were significantly reduced in the C26 group as compared to control and were partially restored to control level by FBX treatment (Figure 36E, F).

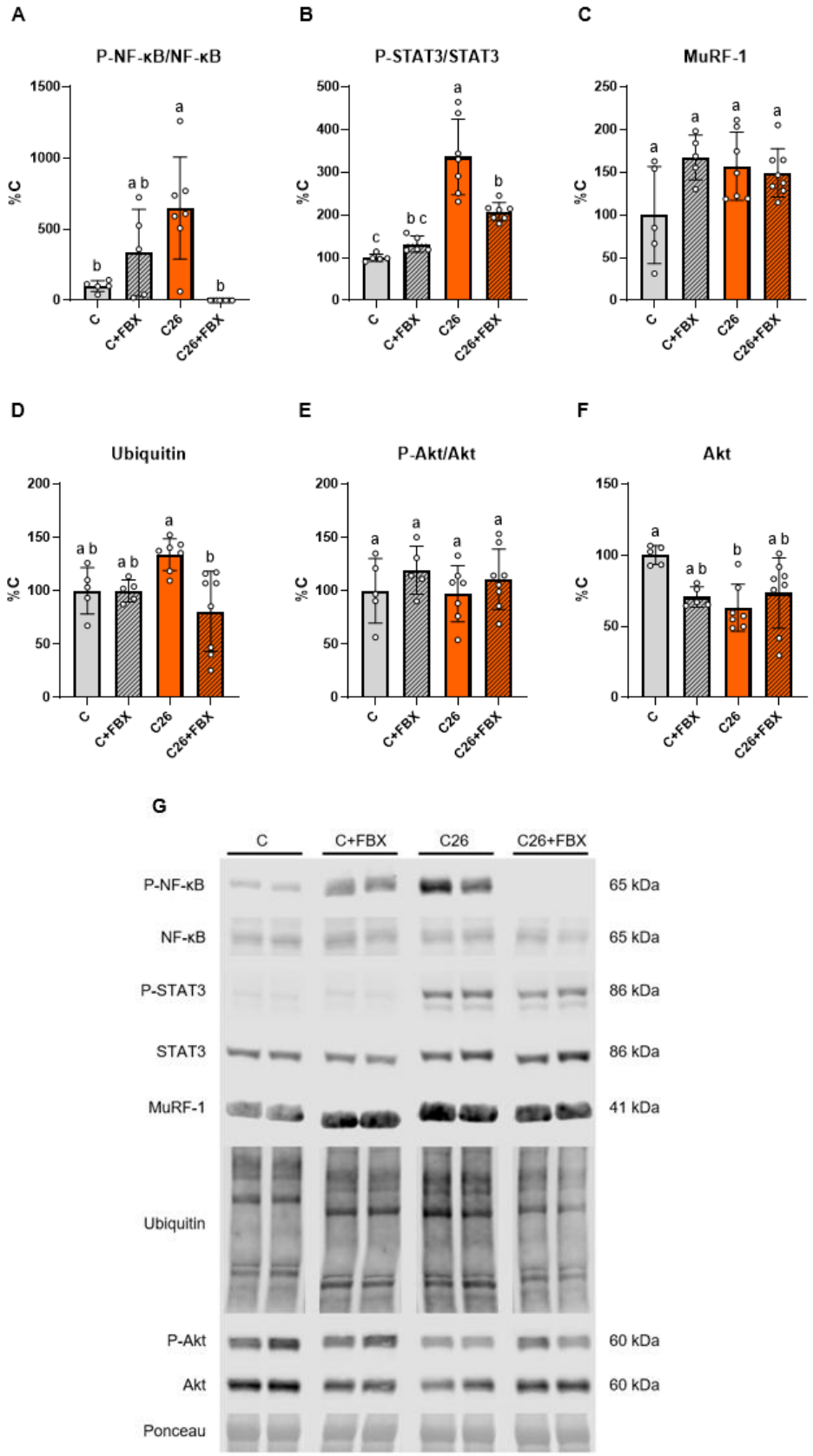

Figure 36. Skeletal muscle protein levels of markers of inflammation and proteostasis. (*A-F*) Protein levels of P-NF-κB/NF-κB (*A*), P-STAT3/STAT3 (*B*),

MuRF-1 (*C*), ubiquitin (*D*), P-Akt/Akt (*E*), and Akt (*F*). (*G*) Representative western blotting bands. Protein levels normalized to Ponceau staining and represented as percentage of control values. Experimental groups: control (C; n=5), FBX-treated control (C+FBX; n=5), C26 tumor-bearing mice (C26; n=7), FBX-treated C26 tumor-bearing mice (C26+FBX; n=8). Data expressed as mean ± standard deviation. Significant differences ($p < 0.05$) represented by different letters. Abbreviations: Protein Kinase B (Akt), muscle ring-finger protein-1 (MuRF-1), nuclear factor kappa-light-chain-enhancer of activated B cells (NF-κB), signal transducer and activator of transcription 3 (STAT3).

5.11. Febuxostat exacerbates tumor-driven mitochondrial alterations in the skeletal muscle of C26 hosts

To determine if the protective effects of FBX on muscle force were related to improved mitochondrial homeostasis, key mitochondrial markers were assessed at protein level. In skeletal muscle, OPA1, MFN2, and Cyt C protein levels were comparable between untreated C26 hosts and control, though significantly reduced in the C26+FBX group as compared to control. Similar trends were found for TOMM20 protein levels (Figure 37A-D). A slightly different pattern was observed for VDAC, as its levels were significantly reduced in both FBX-treated and untreated C26 tumor-bearing mice as compared to control, with a similar trend observed in the FBX-treated controls (Figure 37E).

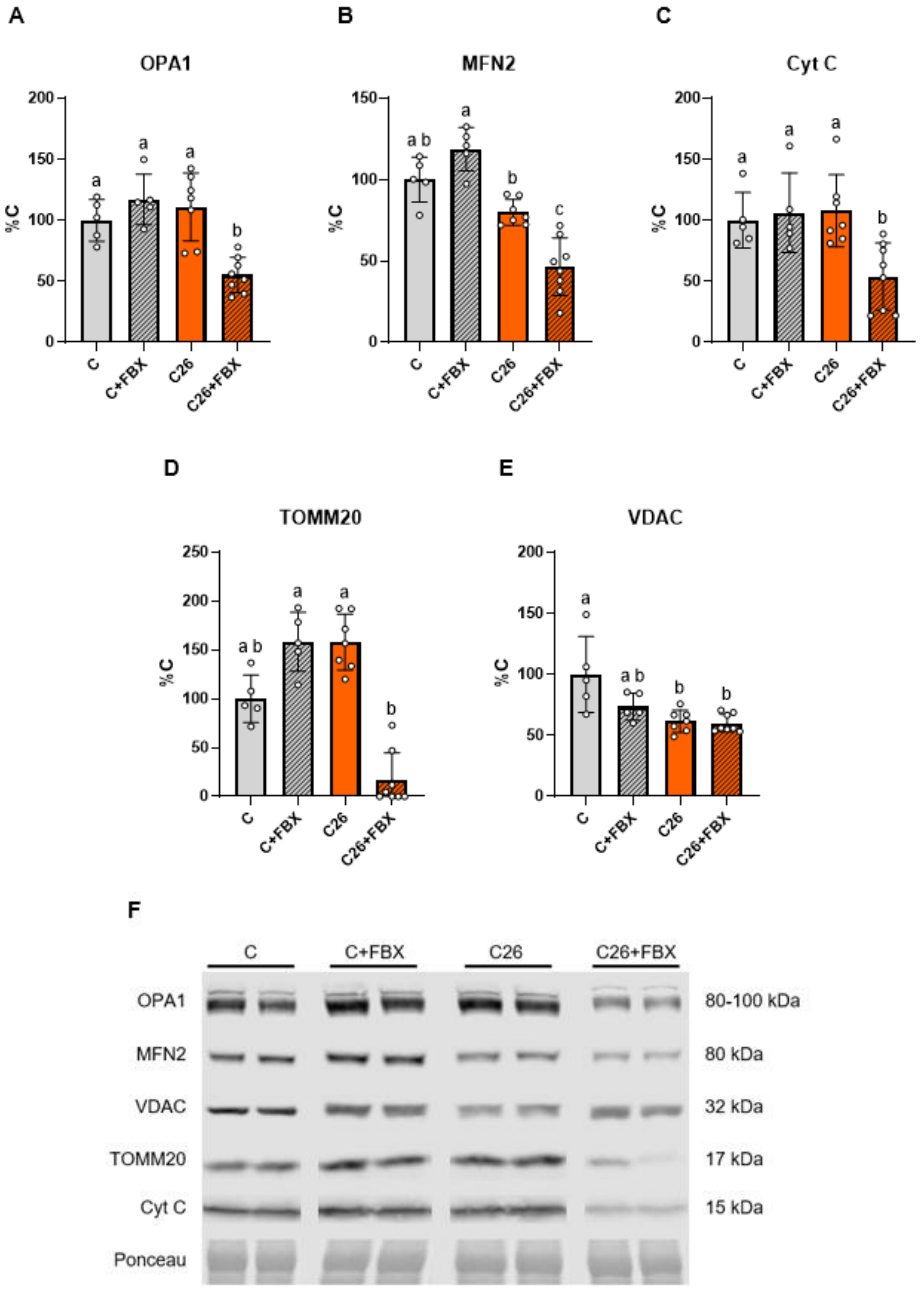

Figure 37. Skeletal muscle protein levels of mitochondrial markers. (*A-E*) Protein levels of OPA1 (A), MFN2 (*B*), Cyt C (*C*), TOMM20 (*D*), and VDAC (*E*). (*F*) Representative western blotting bands. Protein levels normalized to Ponceau staining and represented as percentage of control values. Experimental groups: control (C; n=5), FBX-treated control (C+FBX; n=5), C26 tumor-bearing mice (C26; n=7), FBX-treated C26 tumor-bearing mice (C26+FBX; n=8). Data expressed as mean ± standard deviation. Significant differences ($p < 0.05$) represented by different letters. Abbreviations: cytochrome c (Cyt C), mitofusin 2 (MFN2), OPA1 mitochondrial dynamin like GTPase (OPA1), translocase of outer

mitochondrial membrane 20 (TOMM20), voltage-dependent anion channel (VDAC).

6. DISCUSSION

The present study explores the administration of interleukin-4 (IL4) as an immunomodulatory strategy able to improve the host immune response, while mimicking the effects of exercise by rescuing muscle-specific and systemic metabolism in cancer hosts, overall expanding its previously described efficacy in targeting cancer cachexia by improving muscle mass and function, myogenesis, and survival[61].

The effectiveness of IL4 in preventing cachexia in the C26 hosts was previously reported[61]. This finding is confirmed in the present study, with the additional observation that the loss of body weight, muscle strength, muscle and white adipose tissue mass occurring at the experimental endpoint (EEP) were undetectable at the early time point (ETP). The protective effect exerted by IL4 appears to directly impinge on cachexia-driving mechanisms, as tumor mass was not significantly modulated by the treatment. A relevant observation regarded food intake, as anorexia, a key contributor to negative energy balance in cancer hosts[29], was less pronounced and delayed in IL4-treated C26 hosts as compared to their untreated counterparts. IL4 also exacerbated splenomegaly in the C26 hosts at both ETP and EEP. This finding supports the immunomodulatory/anti-inflammatory activity of IL4, which, consistent with its known role in promoting Th2-type immune responses, likely engages the host immune system in preventing cachexia[35,82].

The anti-inflammatory activity of IL4 was confirmed by the observation that it reduced the high circulating levels of IL6 in tumor-bearing mice. However, such reduction was far from reaching the control levels, suggesting that the IL4 protective action does not merely consist of the abrogation of IL6 signaling, recognized as a primary driver of cachexia in the C26 hosts[101], but rather involves a more complex modulation of the systemic pro-inflammatory environment. Indeed, IL4 promoted a broader restoration of inflammatory homeostasis in the C26 hosts, as suggested by the reduction of the elevated levels of pro- and anti-inflammatory factors such as TNFα and IL10, respectively.

Additionally, IL4 treatment restored the elevated circulating levels of IP-10 and Eotaxin in the C26 hosts to control values. The reduction of IP-10 is particularly relevant, as elevated circulating IP-10 was associated with cachexia and poor prognosis in cancer patients, reflecting inflammation and immune dysregulation[102–105]. IP-10 was also reported to contribute to an immunosuppressive tumor microenvironment (TME) by recruiting regulatory T cells (Tregs),

suggesting that its reduction by IL4 may be linked to systemic immunomodulation[103,104]. Another possible mechanism involved in IL4 effectiveness is represented by the reduction of circulating Eotaxin, a chemokine involved in both systemic inflammation and neuroinflammation[106,107]. Thus, reduced Eotaxin could result in less neuroinflammation, which could possibly explain the attenuated anorexia occurring in the IL4-treated C26 hosts[108], the more so since anorexia was improved despite persistently low circulating leptin levels, suggesting that IL4 might induce a leptin-independent mechanism of appetite regulation.

IL4 also corrected the tumor-induced reduction of circulating Jagged1, while Notch1 remained suppressed in both C26 groups. Despite this persistent Notch1 suppression, the restoration of its ligand, Jagged1, may compensate for reduced receptor availability, providing a potential systemic mechanism for the previously described IL4-induced improvement in myogenesis[61]. Indeed, the Notch1 signaling pathway is critical for muscle stem cell activation and differentiation[109,110]. Thus, the C26-induced reduction of circulating Jagged1 could represent a systemic impairment of the regenerative drive in the muscle, which IL4 treatment effectively restores, thereby linking the systemic immune response to peripheral tissue repair.

The effects of IL4 on the immune response were further investigated by analyzing the cellular composition of the spleen at EEP. The exacerbated splenomegaly in the C26+IL4 group was associated with the modulation of splenic immune cell populations. Consistent with the known function of IL4 in suppressing Th1 responses[111], a reduction in both splenic Th1 and Cytotoxic T Lymphocyte (CTL) populations was observed in the C26+IL4 group as compared to controls. The most striking finding, however, was the effect of IL4 on some immunosuppressive cell populations. Indeed, the cytokine revealed able to rescue the marked increase in splenic MDSCs and Tregs occurring in the untreated C26 hosts. Such changes are hallmarks of cancer-associated immunosuppression that contribute to T cell dysfunction and were linked to cachexia progression[56,112]. The rescue achieved by IL4 provides direct evidence that tumor-induced immunosuppression in the host can be effectively reversed. Importantly, this effect appears to play a substantial role in the therapeutic benefit of IL4, as evidenced by the significantly negative correlation observed between the percentages of splenic immunosuppressive cells and some hallmarks of cachexia.

The immunomodulatory activity of IL4 on immune cell populations was also reflected, though more slightly than in the spleen, in the circulation. Indeed, the C26-induced increase in the neutrophil-to-lymphocyte ratio (NLR) was partially attenuated in the C26+IL4 group. This is

noteworthy, as an elevated NLR is associated with systemic inflammation and poor outcomes in cancer patients[113,114].

A crucial question was how IL4 administration could affect the tumor. Previous findings suggested that IL4 increased tumor necrosis[61]. However, the study by Costamagna and collaborators compared tumors collected at different time points (day 13 after tumor implantation for the C26 group versus day 31 for the C26+IL4 group)[61]. By contrast the present study, using a standardized endpoint (day 15), clarified that IL4 treatment did not impinge on tumor necrosis. While this result, combined with unchanged tumor gross mass, might initially suggest that IL4 exerts limited effects on the tumor, these measurements do not account for potential changes in cellular composition. Given the demonstrated systemic immunomodulatory activity of IL4, it is likely that the TME is also affected. Indeed, single nuclei RNA-sequencing analysis performed at EEP revealed a profound remodeling of the TME upon IL4 treatment. Unexpectedly, tumors from IL4-treated mice showed a decrease in total T cell infiltration and an increase in the proportion of malignant cells as compared to the untreated counterparts. The decrease in tumor-infiltrated T cells may seem contradictory considering the reduction in immunosuppressive cells observed in the spleen. However, further analyses are required to characterize the specific T cell subtypes in the tumor, as the reduction in T cells may be attributed to Tregs and exhausted T cells. Similarly, the relative increase in malignant cells upon IL4 treatment, supported by the increase in Ki67 gene expression, is compelling considering that IL4 did not enhance C26 cell proliferation *in vitro* [61]. This may suggest an indirect mechanism by which IL4 promotes cancer cell proliferation in the C26 hosts, likely mediated by the cytokine ability to modulate the TME. Along this line, several studies reported IL4 to promote tumor cell proliferation alongside an immunosuppressive TME[115–117]. Consistently, IL4 treatment shifted the TME from an M1-dominant to an M2-dominant macrophage profile. The preponderance of M2 macrophages is typically associated with both an immunosuppressive TME and tumor progression[118], which aligns with the observed increase in malignant cells. Quite interestingly, this occurred alongside reduced systemic immunosuppression and cachexia severity. All of these observations taken together, while the effect of IL4 on malignant cells and the TME warrants careful consideration, this phenotype where a “pro-tumor” TME coexists with significantly reduced cachexia may represent a unique therapeutic opportunity. Specifically, IL4 could be combined with chemotherapy or immunotherapy to improve the host tolerance to anticancer treatment toxicity.

The previously discussed benefits of IL4 on the systemic immune response, which correlated with muscle preservation, were also reflected at the tissue level, highlighting an immunometabolic role for the cytokine in the skeletal muscle. While MDSCs were abnormally elevated in the spleen of the C26 hosts, they are also known to infiltrate into the skeletal muscle during cachexia and actively contribute to wasting[58]. Indeed, a metabolic signature potentially consistent with MDSC infiltration could take place in the muscle. MDSCs are characterized by high arginase-1 activity, which converts L-arginine to L-ornithine, a precursor for polyamines[119,120]. Accordingly, putrescine and spermidine were markedly accumulated in the muscle of the untreated C26 hosts and reduced towards control levels by IL4 treatment. The dysregulation of polyamine metabolism in the skeletal muscle was reported in different models of muscle atrophy, including starvation, cachexia, amyotrophic lateral sclerosis and immobilization, with putrescine and spermidine accumulation being a common trait[121,122]. In the context of cancer cachexia, the IL4-dependent reduction of these polyamines might suggest that the treatment counteracts the infiltration of MDSCs in the muscle, although muscle L-arginine was not depleted, but elevated in the C26 hosts as compared to controls. Such accumulation, which has been reported in another study as well[123], may result from accelerated protein catabolism, releasing large amounts of L-arginine that could mask the consumption by MDSC arginase-1 activity. Alternatively, the concomitant accumulation of L-arginine, putrescine, and spermidine in the muscle of the C26 hosts could depend on altered conversion to spermine, as suggested by Oyabu and collaborators[121], paralleled by product-dependent inhibition of both arginases and ornithine decarboxylases. The data reported in the present study do not allow to draw conclusions about the mechanisms by which IL4 can modulate polyamine metabolism in the muscle of tumor-bearing mice. The cytokine was reported to improve the downregulation of polyamine metabolism in obesity[124], as well as to induce the activity of ornithine decarboxylase in both smooth muscle cells[125] and alternatively activated macrophages[126]. However, these observations point to IL4 as a stimulator of polyamine biosynthesis, which is counterintuitive in the scenario of the present investigation, paving the way to further studies aimed to unravel the mechanisms by which IL4 impinges on polyamine flux.

Another interesting observation is represented by the pattern of L-tryptophan and its downstream metabolites, such as indolepyruvate[127]. Indeed, while L-tryptophan was accumulated in the muscle of both treated and untreated C26 hosts, indolepyruvate was elevated in the former and reduced towards control levels in the latter. Notably, indolepyruvate is a

ligand and potent proagonist for aryl hydrocarbon receptor (AHR) activation, which was shown to drive immunosuppression in the context of inflammatory diseases and in the tumor microenvironment, behaving as an oncometabolite to support cancer progression[128–131]. The conversion of L-tryptophan to indolepyruvate is performed by IL4I1, a L-amino-acid oxidase that can be induced both by IL4 and a sustained pro-inflammatory environment[127,132] and acts as an immune response inhibitor, impinging on $CD4^+$ T cell differentiation and macrophage polarization[133]. IL4I1 was reported to be overactivated in muscle stem cells exposed to TNFα combined with IFNγ, resulting in an anti-inflammatory/immunomodulating response depending on the AHR-induced TNF-stimulated gene 6[134]. This observation is consistent with the improved muscle regeneration previously shown in the C26 hosts exposed to IL4[61]. In addition, the possibility that IL4I1 activation, whether due to the inflammatory milieu or to IL4 administration, might result in immunoregulation in the skeletal muscle cannot be discarded and requires further investigations.

The hypothesis that IL4 could restore the immunological homeostasis in the skeletal muscle is also supported by sphingosine 1-phosphate (S1P) levels, which are increased in the untreated C26 hosts and restored to control levels by the cytokine. Indeed, S1P gradients are responsible for correct immune cell trafficking and its accumulation is associated with inflammation[135–138]. This finding is also relevant to muscle wasting itself, as S1P signaling was reported to be induced in C2C12 myotube cultures exposed to TNFα. Of interest, the reduction of myotube size as well as the induction of autophagy due to TNFα were counteracted by inhibiting S1P-dependent signaling[136]. Thus, the correction of S1P levels suggests that IL4 is able to protect the muscle in the C26 hosts through distinct, possibly interconnected mechanisms, including both a direct action on protein breakdown and a reshape of the muscle immune microenvironment.

Alongside the modulation of several immunometabolites, IL4 also partially restored the levels of amino acid metabolism components in the skeletal muscle of the C26 hosts. In line with other muscle wasting conditions characterized by increased proteolysis[139,140], the levels of alanine in the skeletal muscle of the C26 hosts were markedly reduced, while those of phenylalanine were increased. In both cases, IL4 treatment restored their levels towards control values, suggesting that, among other mechanisms, the cytokine protects against cancer-induced muscle wasting by correcting protein hypercatabolism.

Despite its broad metabolic rescue, IL4 treatment failed to correct the elevated levels of uric acid observed in the skeletal muscle of the C26 hosts. This finding, coupled with the depletion of glutathione in both C26 groups as compared to controls, suggested that xanthine oxidase (XO)-driven oxidative stress could be relevant to the pathogenesis of muscle wasting in tumor hosts. Hyperuricemia and XO hyperactivity are established contributors to muscle inflammation, oxidative stress, and wasting in various contexts[37,96–98,141]. Indeed, XO inhibition was previously explored as a strategy to prevent cancer-induced muscle wasting, providing positive outcomes[45,98,99]. However, consistently with another study involving a different model, the administration of the XO inhibitor febuxostat (FBX) failed to prevent cachexia in the C26 hosts. The fact that FBX treatment was able to reduce XO activity and markers of the pro-inflammatory signaling suggested that the treatment was effective in reducing XO-dependent oxidative stress in the skeletal muscle of the C26 hosts. Furthermore, it appeared to mildly improve proteostasis, an observation consistent with another study investigating the relevance of XO inhibition to cancer cachexia[45]. Along this line, FBX treatment preserved muscle strength in the C26 hosts. This finding, however, highlighted a paradox. While loss of muscle strength is known to anticipate atrophy[142], here, the ability of FBX to prevent cancer-induced muscle weakness, coupled with modest improvements in proteostasis markers, occurred despite its failure to prevent tissue wasting. Moreover, FBX treatment dramatically exacerbated cancer-induced mitochondrial alterations, highlighting significant concerns about the use of this therapeutic approach for the treatment of cancer cachexia.

In contrast with the data obtained with FBX, IL4 proved able to correct the mitochondrial derangements occurring in the skeletal muscle of tumor-bearing mice at EEP. Indeed, IL4 effectively restored physiological levels of markers of mitochondrial content, biogenesis, and disposal, while enhancing the OXPHOS system and the oxygen consumption rate. This pattern was corroborated by the observation that IL4 treatment, also by preventing the marked cancer-induced loss of hexokinase II activity, corrected the levels of TCA cycle intermediates, supporting the restoration of energy metabolism. Accordingly, the rescue of hexokinase activity has been previously identified as a contributing factor to the amelioration of dexamethasone-induced muscle atrophy achieved by a nutritional intervention[143]. Interestingly, IL4-treated control mice displayed higher levels of pyruvic, fumaric, and malic acid as compared to their untreated counterparts, suggesting that, in healthy mice, the cytokine increases the availability of substrate for the TCA cycle, the entity of which is reduced, though still present, in IL4-treated tumor hosts. The ability of IL4 to modulate energy metabolism in the skeletal muscle of tumor-

bearing mice aligns with previous findings where the cytokine was found to be capable of stimulating OXPHOS activity in alternatively activated macrophages[144]. Moreover, in an *in vitro* model of colon mucosa, IL4 was reported to partially restore the loss of OXPHOS complexes I and IV induced by TNFα alone or combined with IFNγ[145]. Finally, other studies reported that IL4 was able to improve glucose and lipid metabolism in mice with high-fat diet-induced obesity[146] or streptozotocin-induced diabetes[147].

To determine whether, beyond inducing splenomegaly, IL4 at ETP could also modulate energy metabolism, markers of mitochondrial homeostasis and function were analyzed. The results show that the protein levels of the electron transport chain complexes I, II, and IV were significantly higher in the untreated C26 hosts compared to healthy mice, likely reflecting a compensatory mechanism to support the physiological energy balance. However, when OCR was assessed at ETP, a non-significant trend towards reduction in comparison to control values could be observed, anticipating the changes occurring at EEP. Unchanged OCR despite increased protein levels of OXPHOS complexes could result from decreased enzymatic activity, electron transfer defects, or limited substrate availability[148,149]. Along this line, the hypothesis that the mitochondrial system attempts to cope with tumor-induced energy stress appears reasonable, also considering that markers of mitochondrial content, biogenesis, and disposal at ETP remained comparable between tumor hosts and controls, reflecting a strenuous attempt to maintain the energy steady-state, which is eventually lost at EEP. Interestingly, in the IL4-treated C26 tumor-bearing mice, the protein levels of OXPHOS complexes I, II, and IV showed a non-significant trend towards the restoration of control levels, suggesting that IL4 administration could promote the preservation of metabolic stability across both time points, partially preventing the early futile compensatory phase and the subsequent energy collapse.

At EEP, IL4 treatment modulated muscle lipid metabolism primarily in the C26 tumor-bearing mice, as the lipidomic profile remained comparable between treated and untreated controls. Importantly, IL4 partially prevented cancer-induced accumulation of ceramides, which have been previously described as markers of cachexia[150]. This finding aligns with previous studies where interventions that reduced the excess of ceramides in the muscle had a positive impact on both cancer-induced muscle wasting and sarcopenia, also improving muscle function[151,152]. The existence of a link between IL4 and ceramide metabolism is supported by previous work showing that activated T lymphocytes from mice lacking ceramide kinase do not secrete IL4[153]. Furthermore, the fact that *de novo* sphingolipid biosynthesis inhibition was reported to have a positive impact on myogenic differentiation[154] provides another clue explaining the pro-

myogenic effects of IL4[61]. In general, with minor exceptions, IL4 partially restored the physiological levels of most of the significantly dysregulated lipids, including cholesteryl esters, sphingosines, phosphatidylserines, and lysophosphatidylcholines, thereby correcting a lipidomic profile that reflected inflammation, altered membrane integrity, and cell death[152,155–159]. Notably, the modulation of phosphatidylserine levels in the muscle has also been linked to exercise, as these lipids have been reported to be reduced in exercised tumor-bearing rats as compared to their sedentary counterparts[160]. Such an effect was partially mimicked by IL4 administration in the C26 tumor-bearing mice.

As previously suggested[146,147], the ability of IL4 to modulate metabolism goes beyond the skeletal muscle and extends systemically. Specifically, at EEP, IL4 administration modulated the hepatic metabolome and, to a lesser extent, the lipidome in the C26 tumor-bearing mice. Consistent with the findings in the muscle, IL4 partially reversed the cancer-induced increase in phenylalanine levels, supporting an antiproteolytic activity of the cytokine in the liver as well. Interestingly, several glycolysis intermediates were increased in the C26 tumor-bearing mice and were partially reduced by IL4, suggesting that the treatment likely accelerates glycolysis rates, potentially accounting for the slight, though non-significant, increased ATP and NADH levels. Conversely, and in contrast to the pattern observed in the muscle, the hepatic levels of TCA cycle intermediates, such as citric, malic, and fumaric acid, were higher in C26 tumor-bearing mice than in controls and were reduced by IL4. This picture could suggest an accelerated TCA cycle activity, again supported by the increasing trends of both ATP and NADH. The beneficial impact of IL4 on the TCA cycle was further supported by the fact that the levels of several acylcarnitines, crucial molecules for fatty acid import into mitochondria, were significantly increased in the liver of IL4-treated C26 hosts. Along this line, the IL4-dependent increase in liver-derived energy could support muscle mass and function.

The results here reported demonstrate how IL4 effectiveness in preventing muscle wasting relies on the preservation of mitochondrial homeostasis and energy metabolism. The immunomodulatory and anti-inflammatory activity of IL4 likely contributes to such effects, as suggested by the negative correlation between reduced spleen MDCS and Treg levels and muscle mass and strength. The benefits on the muscle are accompanied by a partial correction of cancer-induced systemic metabolic dysregulation, a central feature of cachexia responsible for energy imbalance and body wasting[161,162]. Importantly, IL4 mimics some exercise-induced effects, including the upregulation of PGC-1α, ceramide reduction, phosphatidylcholine and phosphatidylserine accumulation, and TCA cycle improvement in the skeletal muscle.

Furthermore, IL4 induced the accumulation of medium- and long-chain acylcarnitines in the liver, a phenomenon previously described as a physiological metabolic adaptation to exercise[163,164]. In turn, exercise was shown to increase circulating IL4 levels[165] as well as the expression of IL4 and the IL4 receptor in the skeletal muscle[84,166], strongly indicating an interplay between IL4 and muscle function. Consistently, one of the typical features of exercise, namely improved insulin resistance[167], was reported to be induced by IL4 exposure in C2C12 myotube cultures[165] and in the muscle of diabetic mice[168]. Taking all the above into consideration, this work shows that IL4 could reprogram muscle and hepatic metabolism in the C26 tumor-bearing mice, promoting an exercise-like profile, activating a protective mechanism able to compensate for the detrimental metabolic demands of the tumor. An apparent note of care of the data reported in the present study comes from the observation that IL4 also proved able to modulate the TME putting in place a tumor-favoring niche. However, such a pattern takes place in face of a markedly improved body and tissue trophism, suggesting that IL4 could be usefully combined with conventional anticancer approaches to improve the ability of the patient to successfully cope with treatment toxicity.

7. CONCLUSIONS

The present study aimed to investigate novel strategies to counteract cancer cachexia by modulating the immune response and metabolism. The results presented here expand on previous knowledge of the benefits of IL4 in the context of cancer cachexia. While IL4 was previously shown to improve muscle mass and function, myogenesis, and survival in the C26 tumor-bearing mice, the results reported here demonstrate a broader range of activity of the cytokine in the same context.

A crucial finding in this study is that IL4 is able to counteract cancer-induced systemic immunosuppression, a relevant observation given that the severity of immune dysregulation was found to correlate with that of cachexia. This immunomodulatory activity of IL4 appeared to be tissue-specific. Indeed, preliminary evidence of the cytokine ability to improve the local immune response in the skeletal muscle was provided by the modulation of several relevant immunometabolites. IL4 modulated the tumor microenvironment (TME) as well, shifting it to an immunosuppressive, tumor-favoring profile. However, this occurred in parallel with a net improvement of cachexia, suggesting that IL4 could be combined with anticancer treatments to increase their tolerance and overall therapeutic efficacy.

IL4 was shown to be a broad metabolic modulator as well. First, it improved mitochondrial homeostasis and muscle metabolism, including energy metabolism. Second, it improved hepatic metabolism, collectively showing that IL4 modulates systemic metabolism in an exercise-like manner. This adaptation appears to give a metabolic advantage to the host, allowing it to efficiently face the tumor metabolic demands, thereby highlighting the pleiotropic activity of the cytokine.

However, IL4 was unable to totally rescue cancer-induced metabolic dysregulation. For instance, muscle uric acid levels, which increase in the presence of cancer due to xanthine oxidase hyperactivity, were not reduced by IL4. The relevance of this specific pathway was assessed by inhibiting xanthine oxidase via febuxostat administration in C26 tumor-bearing mice. While improving parameters of muscle inflammation and proteostasis, febuxostat exacerbated mitochondrial alterations and ultimately was unable to counteract cachexia. While the intervention could be optimized, as underscored by the limited modulation of the circulating uric acid levels, its failure to prevent cachexia does not support further investigation of this specific therapeutic strategy.

The negative results concerning febuxostat treatment strongly support the principle that anti-cachexia strategies must tackle this multi-factorial and multi-organ syndrome from multiple angles simultaneously, while those targeting a single pathway are unlikely to succeed. Indeed, the multi-target activity of IL4 is central to its effectiveness. While improving the immune response, IL4 also mimics exercise effects, improving muscle-specific and systemic metabolism, thereby successfully counteracting cancer cachexia. Although further studies are needed to fully characterize the effects of IL4 on the muscle-specific immune response and on the TME, the results presented here highlight IL4 as a potential novel strategy for the treatment of cancer cachexia.

8. ACKNOWLEDGMENTS

This work was supported by the Associazione Italiana per la Ricerca sul Cancro (AIRC, IG 25809 to P. Costelli), the National Institutes of Health (NIH, P30CA046934 to the University of Colorado Cancer Center, Aurora, CO, USA), a research grant from the Cancer League of Colorado, Inc. (AWD-242527-AB), the University of Turin (Turin, Italy), the University of Eastern Piedmont (Novara, Italy), and the University of Colorado Anschutz Medical Campus (Aurora, CO, USA), including its Metabolomics Core.

This thesis is part of the project NODES which has received funding from the MUR – M4C2 1.5 of PNRR with grant agreement no. ECS00000036.

9. REFERENCES

1. Frontera WR, Ochala J. Skeletal muscle: a brief review of structure and function. *Calcif Tissue Int*. 2015;96(3):183-195. doi:10.1007/S00223-014-9915-Y

2. Mukund K, Subramaniam S. Skeletal muscle: A review of molecular structure and function, in health and disease. *Wiley Interdiscip Rev Syst Biol Med*. 2020;12(1). doi:10.1002/WSBM.1462

3. Argilés JM, Campos N, Lopez-Pedrosa JM, Rueda R, Rodriguez-Mañas L. Skeletal Muscle Regulates Metabolism via Interorgan Crosstalk: Roles in Health and Disease. *J Am Med Dir Assoc*. 2016;17(9):789-796. doi:10.1016/j.jamda.2016.04.019

4. Xiao J, ed. Muscle Atrophy. 2018;1088. doi:10.1007/978-981-13-1435-3

5. Gao QQ, McNally EM. The Dystrophin Complex: Structure, Function, and Implications for Therapy. *Compr Physiol*. 2015;5(3):1223-1239. doi:10.1002/CPHY.C140048

6. Bonetto A, Bonewald LF. Bone and Muscle. *Basic and Applied Bone Biology*. Published online January 1, 2019:317-332. doi:10.1016/B978-0-12-813259-3.00016-6

7. Tintignac LA, Brenner HR, Rüegg MA. Mechanisms Regulating Neuromuscular Junction Development and Function and Causes of Muscle Wasting. *Physiol Rev*. 2015;95(3):809-852. doi:10.1152/PHYSREV.00033.2014

8. Castets P, Ham DJ, Rüegg MA. The TOR Pathway at the Neuromuscular Junction: More Than a Metabolic Player? *Front Mol Neurosci*. 2020;13. doi:10.3389/FNMOL.2020.00162

9. Kuo IY, Ehrlich BE. Signaling in muscle contraction. *Cold Spring Harb Perspect Biol*. 2015;7(2). doi:10.1101/CSHPERSPECT.A006023

10. Bloemberg D, Quadrilatero J. Rapid determination of myosin heavy chain expression in rat, mouse, and human skeletal muscle using multicolor immunofluorescence analysis. *PLoS One*. 2012;7(4). doi:10.1371/JOURNAL.PONE.0035273

11. Schiaffino S, Reggiani C. Fiber types in mammalian skeletal muscles. *Physiol Rev*. 2011;91(4):1447-1531. doi:10.1152/PHYSREV.00031.2010

12. Wang Y, Pessin JE. Mechanisms for fiber-type specificity of skeletal muscle atrophy. *Curr Opin Clin Nutr Metab Care*. 2013;16(3):243-250. doi:10.1097/MCO.0B013E328360272D

13. Hargreaves M, Spriet LL. Skeletal muscle energy metabolism during exercise. *Nat Metab*. 2020;2(9):817-828. doi:10.1038/S42255-020-0251-4

14. Koopman R, Ly CH, Ryall JG. A metabolic link to skeletal muscle wasting and regeneration. *Front Physiol*. 2014;5. doi:10.3389/FPHYS.2014.00032

15. Gastin PB. Energy system interaction and relative contribution during maximal exercise. *Sports Med*. 2001;31(10):725-741. doi:10.2165/00007256-200131100-00003

16. Roberts DJ, Miyamoto S. Hexokinase II integrates energy metabolism and cellular protection: Akting on mitochondria and TORCing to autophagy. *Cell Death Differ*. 2015;22(2):248-257. doi:10.1038/CDD.2014.173

17. Peterson CM, Johannsen DL, Ravussin E. Skeletal muscle mitochondria and aging: a review. *J Aging Res*. 2012;2012. doi:10.1155/2012/194821

18. Gan Z, Fu T, Kelly DP, Vega RB. Skeletal muscle mitochondrial remodeling in exercise and diseases. *Cell Res*. 2018;28(10):969-980. doi:10.1038/S41422-018-0078-7

19. Hood DA, Memme JM, Oliveira AN, Triolo M. Maintenance of Skeletal Muscle Mitochondria in Health, Exercise, and Aging. *Annu Rev Physiol*. 2019;81:19-41. doi:10.1146/ANNUREV-PHYSIOL-020518-114310

20. Nolfi-Donegan D, Braganza A, Shiva S. Mitochondrial electron transport chain: Oxidative phosphorylation, oxidant production, and methods of measurement. *Redox Biol*. 2020;37. doi:10.1016/j.redox.2020.101674

21. Wu Z, Ho WS, Lu R. Targeting Mitochondrial Oxidative Phosphorylation in Glioblastoma Therapy. *Neuromolecular Med*. 2022;24(1):18-22. doi:10.1007/S12017-021-08678-8

22. Liang H, Ward WF. PGC-1alpha: a key regulator of energy metabolism. *Adv Physiol Educ*. 2006;30(4):145-151. doi:10.1152/ADVAN.00052.2006

23. Tyagi S, Gupta P, Saini A, Kaushal C, Sharma S. The peroxisome proliferator-activated receptor: A family of nuclear receptors role in various diseases. *J Adv Pharm Technol Res*. 2011;2(4):236-240. doi:10.4103/2231-4040.90879

24. Leduc-Gaudet JP, Hussain SNA, Barreiro E, Gouspillou G. Mitochondrial Dynamics and Mitophagy in Skeletal Muscle Health and Aging. *Int J Mol Sci*. 2021;22(15). doi:10.3390/IJMS22158179

25. Onishi M, Yamano K, Sato M, Matsuda N, Okamoto K. Molecular mechanisms and physiological functions of mitophagy. *EMBO J*. 2021;40(3). doi:10.15252/EMBJ.2020104705

26. Ding WX, Yin XM. Mitophagy: mechanisms, pathophysiological roles, and analysis. *Biol Chem*. 2012;393(7):547-564. doi:10.1515/HSZ-2012-0119

27. Li Y, Zheng W, Lu Y, et al. BNIP3L/NIX-mediated mitophagy: molecular mechanisms and implications for human disease. *Cell Death Dis*. 2021;13(1). doi:10.1038/S41419-021-04469-Y

28. Baracos VE, Martin L, Korc M, Guttridge DC, Fearon KCH. Cancer-associated cachexia. *Nat Rev Dis Primers*. 2018;4. doi:10.1038/NRDP.2017.105

29. Garcia-Castillo L, Rubini G, Costelli P. Pharmacotherapeutic options for cancer cachexia: emerging drugs and recent approvals. *Expert Opin Pharmacother*. 2023;24(9):1053-1065. doi:10.1080/14656566.2023.2209316

30. Ballarò R, Beltrà M, De Lucia S, et al. Moderate exercise in mice improves cancer plus chemotherapy-induced muscle wasting and mitochondrial alterations. *FASEB J*. 2019;33(4):5482-5494. doi:10.1096/FJ.201801862R

31. von Haehling S, Anker SD. Prevalence, incidence and clinical impact of cachexia: facts and numbers-update 2014. *J Cachexia Sarcopenia Muscle*. 2014;5(4):261-263. doi:10.1007/S13539-014-0164-8

32. Mariean CR, Tiucă OM, Mariean A, Cotoi OS. Cancer Cachexia: New Insights and Future Directions. *Cancers (Basel)*. 2023;15(23). doi:10.3390/CANCERS15235590

33. Fearon K, Strasser F, Anker SD, et al. Definition and classification of cancer cachexia: An international consensus. *Lancet Oncol*. 2011;12(5):489-495. doi:10.1016/S1470-2045(10)70218-7

34. Evans WJ, Morley JE, Argilés J, et al. Cachexia: A new definition. *Clinical Nutrition*. 2008;27(6):793-799. doi:10.1016/j.clnu.2008.06.013

35. Penna F, Rubini G, Costelli P. Immunomodulation: A new approach to cancer cachexia, potentially suitable for aging. *Mol Aspects Med*. 2024;100. doi:10.1016/j.mam.2024.101318

36. Beltrà M, Pin F, Ballarò R, Costelli P, Penna F. Mitochondrial Dysfunction in Cancer Cachexia: Impact on Muscle Health and Regeneration. *Cells*. 2021;10(11). doi:10.3390/CELLS10113150

37. Abrigo J, Elorza AA, Riedel CA, et al. Role of Oxidative Stress as Key Regulator of Muscle Wasting during Cachexia. *Oxid Med Cell Longev*. 2018;2018. doi:10.1155/2018/2063179

38. Argilés JM, Busquets S, Stemmler B, López-Soriano FJ. Cachexia and sarcopenia: Mechanisms and potential targets for intervention. *Curr Opin Pharmacol*. 2015;22:100-106. doi:10.1016/j.coph.2015.04.003

39. Argilés JM, Busquets S, Stemmler B, López-Soriano FJ. Cancer cachexia: understanding the molecular basis. *Nat Rev Cancer*. 2014;14(11):754-762. doi:10.1038/NRC3829

40. Murphy BT, Mackrill JJ, O'Halloran KD. Impact of cancer cachexia on respiratory muscle function and the therapeutic potential of exercise. *J Physiol*. 2022;600(23):4979-5004. doi:10.1113/JP283569

41. Argilés JM, Fontes-Oliveira CC, Toledo M, López-Soriano FJ, Busquets S. Cachexia: a problem of energetic inefficiency. *J Cachexia Sarcopenia Muscle*. 2014;5(4):279. doi:10.1007/S13539-014-0154-X

42. van der Ende M, Grefte S, Plas R, et al. Mitochondrial dynamics in cancer-induced cachexia. *Biochim Biophys Acta Rev Cancer*. 2018;1870(2):137-150. doi:10.1016/j.bbcan.2018.07.008

43. Vanderveen BN, Fix DK, Carson JA. Disrupted Skeletal Muscle Mitochondrial Dynamics, Mitophagy, and Biogenesis during Cancer Cachexia: A Role for Inflammation. *Oxid Med Cell Longev*. 2017;2017. doi:10.1155/2017/3292087

44. Fornelli C, Beltrà M, Zorzano A, Costelli P, Sebastian D, Penna F. BNIP3 Downregulation Ameliorates Muscle Atrophy in Cancer Cachexia. *Cancers (Basel)*. 2024;16(24). doi:10.3390/CANCERS16244133

45. Springer J, Tschirner A, Hartman K, et al. Inhibition of xanthine oxidase reduces wasting and improves outcome in a rat model of cancer cachexia. *Int J Cancer*. 2012;131(9):2187-2196. doi:10.1002/IJC.27494

46. McClung JM, Judge AR, Powers SK, Yan Z. p38 MAPK links oxidative stress to autophagy-related gene expression in cachectic muscle wasting. *Am J Physiol Cell Physiol*. 2010;298(3):542-549. doi:10.1152/AJPCELL.00192.2009

47. Winfield RD, Delano MJ, Pande K, Scumpia PO, LaFace D, Moldawer LL. Myeloid-derived suppressor cells in cancer cachexia syndrome: a new explanation for an old problem. *JPEN J Parenter Enteral Nutr*. 2008;32(6):651-655. doi:10.1177/0148607108325075

48. Veglia F, Perego M, Gabrilovich D. Myeloid-derived suppressor cells coming of age. *Nat Immunol*. 2018;19(2):108-119. doi:10.1038/S41590-017-0022-X

49. Cao W, Ramakrishnan R, Tuyrin VA, et al. Oxidized lipids block antigen cross-presentation by dendritic cells in cancer. *J Immunol*. 2014;192(6):2920-2931. doi:10.4049/JIMMUNOL.1302801

50. Wu L, Du H, Li Y, Qu P, Yan C. Signal transducer and activator of transcription 3 (Stat3C) promotes myeloid-derived suppressor cell expansion and immune suppression during lung tumorigenesis. *American Journal of Pathology*. 2011;179(4):2131-2141. doi:10.1016/j.ajpath.2011.06.028

51. Vacchelli E, Aranda F, Eggermont A, et al. Trial watch: IDO inhibitors in cancer therapy. *Oncoimmunology*. 2014;3(10):e957994-1-e957994-10. doi:10.4161/21624011.2014.957994

52. Bonetto A, Aydogdu T, Jin X, et al. JAK/STAT3 pathway inhibition blocks skeletal muscle wasting downstream of IL-6 and in experimental cancer cachexia. *Am J Physiol Endocrinol Metab*. 2012;303(3):410-421. doi:10.1152/AJPENDO.00039.2012

53. Huot JR, Novinger LJ, Pin F, Bonetto A. HCT116 colorectal liver metastases exacerbate muscle wasting in a mouse model for the study of colorectal cancer cachexia. *Dis Model Mech*. 2020;13(1). doi:10.1242/DMM.043166

54. Kaiser H, Yu K, Pandya C, et al. Kynurenine, a Tryptophan Metabolite That Increases with Age, Induces Muscle Atrophy and Lipid Peroxidation. *Oxid Med Cell Longev*. 2019;2019. doi:10.1155/2019/9894238

55. Agudelo LZ, Ferreira DMS, Dadvar S, et al. Skeletal muscle PGC-1α1 reroutes kynurenine metabolism to increase energy efficiency and fatigue-resistance. *Nat Commun*. 2019;10(1). doi:10.1038/S41467-019-10712-0

56. Cuenca AG, Cuenca AL, Winfield RD, et al. Novel role for tumor-induced expansion of myeloid-derived cells in cancer cachexia. *J Immunol*. 2014;192(12):6111-6119. doi:10.4049/JIMMUNOL.1302895

57. Deyhle MR, Callaway CS, Neyroud D, D'lugos AC, Judge SM, Judge AR. Depleting Ly6G Positive Myeloid Cells Reduces Pancreatic Cancer-Induced Skeletal Muscle Atrophy. *Cells*. 2022;11(12). doi:10.3390/CELLS11121893

58. Dzierlega K, Chakraborty M, Lee M, et al. Activin A-Expressing Polymorphonuclear Myeloid-Derived Suppressor Cells Infiltrate Skeletal and Cardiac Muscle and Promote Cancer Cachexia. *J Immunol*. 2023;211(3):497-507. doi:10.4049/JIMMUNOL.2200064

59. Ji S, Shi Y, Yin B. Macrophage barrier in the tumor microenvironment and potential clinical applications. *Cell Commun Signal*. 2024;22(1). doi:10.1186/S12964-023-01424-6

60. Baghdadi MB, Tajbakhsh S. Regulation and phylogeny of skeletal muscle regeneration. *Dev Biol*. 2018;433(2):200-209. doi:10.1016/j.ydbio.2017.07.026

61. Costamagna D, Duelen R, Penna F, Neumann D, Costelli P, Sampaolesi M. Interleukin-4 administration improves muscle function, adult myogenesis, and lifespan of colon carcinoma-bearing mice. *J Cachexia Sarcopenia Muscle*. 2020;11(3):783-801. doi:10.1002/JCSM.12539

62. Lu P, Ma Y, Wei S, Liang X. The dual role of complement in cancers, from destroying tumors to promoting tumor development. *Cytokine*. 2021;143. doi:10.1016/j.cyto.2021.155522

63. Han J, Wang Y, Qiu Y, et al. Single-cell sequencing unveils key contributions of immune cell populations in cancer-associated adipose wasting. *Cell Discov*. 2022;8(1). doi:10.1038/S41421-022-00466-3

64. Solheim TS, Laird BJA, Balstad TR, et al. Cancer cachexia: rationale for the MENAC (Multimodal-Exercise, Nutrition and Anti-inflammatory medication for Cachexia) trial. *BMJ Support Palliat Care*. 2018;8(3):258-265. doi:10.1136/BMJSPCARE-2017-001440

65. Prado BL, Qian Y. Anti-cytokines in the treatment of cancer cachexia. *Ann Palliat Med*. 2019;8(1):67-79. doi:10.21037/APM.2018.07.06

66. Argilés JM, López-Soriano FJ, Stemmler B, Busquets S. Therapeutic strategies against cancer cachexia. *Eur J Transl Myol*. 2019;29(1):4-13. doi:10.4081/EJTM.2019.7960

67. Bayliss TJ, Smith JT, Schuster M, Dragnev KH, Rigas JR. A humanized anti-IL-6 antibody (ALD518) in non-small cell lung cancer. *Expert Opin Biol Ther*. 2011;11(12):1663-1668. doi:10.1517/14712598.2011.627850

68. Groarke JD, Crawford J, Collins SM, et al. Ponsegromab for the Treatment of Cancer Cachexia. *N Engl J Med*. 2024;391(24):2291-2303. doi:10.1056/NEJMOA2409515

69. Melero I, Klar K, Leo E. GDF-15 blockade: A multi-directional approach to potentiate cancer immunotherapy and alleviate cancer cachexia. *Clin Transl Med*. 2025;15(4). doi:10.1002/CTM2.70280

70. Hardee JP, Counts BR, Carson JA. Understanding the Role of Exercise in Cancer Cachexia Therapy. *Am J Lifestyle Med*. 2017;13(1):46-60. doi:10.1177/1559827617725283

71. Cento AS, Leigheb M, Caretti G, Penna F. Exercise and Exercise Mimetics for the Treatment of Musculoskeletal Disorders. *Curr Osteoporos Rep*. 2022;20(5):249-259. doi:10.1007/S11914-022-00739-6

72. Màrmol JM, Carlsson M, Raun SH, et al. Insulin resistance in patients with cancer: a systematic review and meta-analysis. *Acta Oncol*. 2023;62(4):364-371. doi:10.1080/0284186X.2023.2197124

73. Khamoui A V., Park BS, Kim DH, et al. Aerobic and resistance training dependent skeletal muscle plasticity in the colon-26 murine model of cancer cachexia. *Metabolism*. 2016;65(5):685-698. doi:10.1016/j.metabol.2016.01.014

74. Gubert C, Hannan AJ. Exercise mimetics: harnessing the therapeutic effects of physical activity. *Nat Rev Drug Discov*. 2021;20(11):862-879. doi:10.1038/S41573-021-00217-1

75. Penna F, Pin F, Ballarò R, Baccino FM, Costelli P. Novel investigational drugs mimicking exercise for the treatment of cachexia. *Expert Opin Investig Drugs*. 2016;25(1):63-72. doi:10.1517/13543784.2016.1117072

76. Mullard A. FDA approves first CAR T therapy. *Nat Rev Drug Discov*. 2017;16(10):669. doi:10.1038/NRD.2017.196

77. Sharma P, Hu-Lieskovan S, Wargo JA, Ribas A. Primary, Adaptive, and Acquired Resistance to Cancer Immunotherapy. *Cell*. 2017;168(4):707-723. doi:10.1016/j.cell.2017.01.017

78. Rejeski K, Cordas dos Santos DM, Parker NH, et al. Influence of Adipose Tissue Distribution, Sarcopenia, and Nutritional Status on Clinical Outcomes After CD19 CAR T-cell Therapy. *Cancer Immunol Res*. 2023;11(6):707-719. doi:10.1158/2326-6066.CIR-22-0487

79. Roy I, Smilnak G, Burkart M, et al. Cachexia is a risk factor for negative clinical and functional outcomes in patients receiving chimeric antigen receptor T-cell therapy for B-cell non-Hodgkin lymphoma. *Br J Haematol*. 2022;197(1):71-75. doi:10.1111/BJH.18054

80. Madeddu C, Busquets S, Donisi C, et al. Effect of Cancer-Related Cachexia and Associated Changes in Nutritional Status, Inflammatory Status, and Muscle Mass on Immunotherapy Efficacy and Survival in Patients with Advanced Non-Small Cell Lung Cancer. *Cancers (Basel)*. 2023;15(4). doi:10.3390/CANCERS15041076

81. Makrakis D, Rounis K, Tsigkas AP, et al. Effect of body tissue composition on the outcome of patients with metastatic non-small cell lung cancer treated with PD-1/PD-L1 inhibitors. *PLoS One*. 2023;18(2). doi:10.1371/JOURNAL.PONE.0277708

82. Zhu J. T helper 2 (Th2) cell differentiation, type 2 innate lymphoid cell (ILC2) development and regulation of interleukin-4 (IL-4) and IL-13 production. *Cytokine*. 2015;75(1):14-24. doi:10.1016/j.cyto.2015.05.010

83. Woodward EA, Prêle CM, Nicholson SE, Kolesnik TB, Hart PH. The anti-inflammatory effects of interleukin-4 are not mediated by suppressor of cytokine signalling-1 (SOCS1). *Immunology*. 2010;131(1):118-127. doi:10.1111/J.1365-2567.2010.03281.X

84. Olga Prokopchuk, Yuefei Liu, Lei Wang, Klaus Wirth, Dietmar Schmidtbleicher, Jürgen M Steinacker. Skeletal muscle IL-4, IL-4Ralpha, IL-13 and IL-13Ralpha1 expression and response to strength training. *Exerc Immunol Rev*. Published online 2007:67-75.

85. Prokopchuk O, Steinacker JM, Nitsche U, et al. IL-4 mRNA Is Downregulated in the Liver of Pancreatic Cancer Patients Suffering from Cachexia. *Nutr Cancer*. 2017;69(1):84-91. doi:10.1080/01635581.2017.1247885

86. Vignali DAA. Multiplexed particle-based flow cytometric assays. *J Immunol Methods*. 2000;243(1-2):243-255. doi:10.1016/S0022-1759(00)00238-6

87. Guo W, Zhang C, Wang X, Dou D, Chen D, Li J. Resolving the difference between left-sided and right-sided colorectal cancer by single-cell sequencing. *JCI Insight*. 2022;7(1). doi:10.1172/JCI.INSIGHT.152616

88. Doerrier C, Garcia-Souza LF, Krumschnabel G, Wohlfarter Y, Mészáros AT, Gnaiger E. High-Resolution FluoRespirometry and OXPHOS Protocols for Human Cells, Permeabilized Fibers from Small Biopsies of Muscle, and Isolated Mitochondria. *Methods Mol Biol*. 2018;1782:31-70. doi:10.1007/978-1-4939-7831-1_3

89. Lemieux H, Blier PU, Gnaiger E. Remodeling pathway control of mitochondrial respiratory capacity by temperature in mouse heart: electron flow through the Q-junction in permeabilized fibers. *Sci Rep*. 2017;7(1). doi:10.1038/S41598-017-02789-8

90. Holmström MH, Iglesias-Gutierrez E, Zierath JR, Garcia-Roves PM. Tissue-specific control of mitochondrial respiration in obesity-related insulin resistance and diabetes. *Am J Physiol Endocrinol Metab*. 2012;302(6):731-739. doi:10.1152/AJPENDO.00159.2011

91. Kuznetsov A V., Kunz WS, Saks V, et al. Cryopreservation of mitochondria and mitochondrial function in cardiac and skeletal muscle fibers. *Anal Biochem*. 2003;319(2):296-303. doi:10.1016/S0003-2697(03)00326-9

92. Nemkov T, Reisz JA, Gehrke S, Hansen KC, D'Alessandro A. High-Throughput Metabolomics: Isocratic and Gradient Mass Spectrometry-Based Methods. *Methods Mol Biol*. 2019;1978:13-26. doi:10.1007/978-1-4939-9236-2_2

93. Reisz JA, Dzieciatkowska M, Stephenson D, Gamboni F, Morton DH, D'Alessandro A. Red Blood Cells from Individuals with Lesch-Nyhan Syndrome: Multi-Omics Insights into a Novel S162N Mutation Causing Hypoxanthine-Guanine Phosphoribosyltransferase Deficiency. *Antioxidants (Basel)*. 2023;12(9). doi:10.3390/ANTIOX12091699

94. Antonio MJ, Zhang C, Le A. Different Tumor Microenvironments Lead to Different Metabolic Phenotypes. *Adv Exp Med Biol*. 2021;1311:137-147. doi:10.1007/978-3-030-65768-0_10

95. Ma S, Lu Y, Sui S, et al. Unraveling the triad of immunotherapy, tumor microenvironment, and skeletal muscle biomechanics in oncology. *Front Immunol*. 2025;16. doi:10.3389/FIMMU.2025.1572821

96. Sautin YY, Johnson RJ. Uric acid: the oxidant-antioxidant paradox. *Nucleosides Nucleotides Nucleic Acids*. 2008;27(6):608-619. doi:10.1080/15257770802138558

97. Derbre F, Ferrando B, Gomez-Cabrera MC, et al. Inhibition of xanthine oxidase by allopurinol prevents skeletal muscle atrophy: role of p38 MAPKinase and E3 ubiquitin ligases. *PLoS One*. 2012;7(10). doi:10.1371/JOURNAL.PONE.0046668

98. Konishi M, Pelgrim L, Tschirner A, et al. Febuxostat improves outcome in a rat model of cancer cachexia. *J Cachexia Sarcopenia Muscle*. 2015;6(2):174-180. doi:10.1002/JCSM.12017

99. Tsukamoto T, Tsujii M, Odake K, et al. Febuxostat reduces muscle wasting in tumor-bearing mice with LM8 osteosarcoma cells via inhibition of reactive oxygen species generation. *Free Radic Res*. 2021;55(7):810-820. doi:10.1080/10715762.2021.1947502

100. Uzu M, Nonaka M, Miyano K, et al. A novel strategy for treatment of cancer cachexia targeting xanthine oxidase in the brain. *J Pharmacol Sci*. 2019;140(1):109-112. doi:10.1016/j.jphs.2019.04.005

101. Bonetto A, Rupert JE, Barreto R, Zimmers TA. The Colon-26 Carcinoma Tumor-bearing Mouse as a Model for the Study of Cancer Cachexia. *J Vis Exp*. 2016;(117). doi:10.3791/54893

102. Kochumon S, Al-Sayyar A, Jacob T, et al. TNF-α Increases IP-10 Expression in MCF-7 Breast Cancer Cells via Activation of the JNK/c-Jun Pathways. *Biomolecules*. 2021;11(9). doi:10.3390/BIOM11091355

103. Lunardi S, Jamieson NB, Lim SY, et al. IP-10/CXCL10 induction in human pancreatic cancer stroma influences lymphocytes recruitment and correlates with poor survival. *Oncotarget*. 2014;5(22):11064-11080. doi:10.18632/ONCOTARGET.2519

104. Xu S, Miura K, Shukuya T, et al. Early Detection of Therapeutic Benefit from PD-1/PD-L1 Blockade in Advanced Lung Cancer by Monitoring Cachexia-Related Circulating Cytokines. *Cancers (Basel)*. 2023;15(4). doi:10.3390/CANCERS15041170

105. Li Y, Wang C, Yin X, Jiang L, Li X, Yang J. Profile and clinical significance of interferon gamma-inducible protein-10 (IP-10) and its receptor in patients with hepatocellular carcinoma. *J Cancer Res Clin Oncol*. 2023;149(16):14879-14888. doi:10.1007/S00432-023-05265-1

106. Zajkowska M, Mroczko B. From Allergy to Cancer-Clinical Usefulness of Eotaxins. *Cancers (Basel)*. 2021;13(1):1-13. doi:10.3390/CANCERS13010128

107. Nazarinia D, Behzadifard M, Gholampour J, Karimi R, Gholampour M. Eotaxin-1 (CCL11) in neuroinflammatory disorders and possible role in COVID-19 neurologic complications. *Acta Neurol Belg*. 2022;122(4):865-869. doi:10.1007/S13760-022-01984-3

108. Ohara S, Inoue KI, Witter MP, Iijima T. Neurobiology of Inflammation-Associated Anorexia. *Front Neurosci*. 2010;3(JAN):59. doi:10.3389/NEURO.23.003.2009

109. Liu L, Charville GW, Cheung TH, et al. Impaired Notch Signaling Leads to a Decrease in p53 Activity and Mitotic Catastrophe in Aged Muscle Stem Cells. *Cell Stem Cell*. 2018;23(4):544-556.e4. doi:10.1016/j.stem.2018.08.019

110. Meng Y, Sanlidag S, Jensen SA, et al. An N-glycan on the C2 domain of JAGGED1 is important for Notch activation. *Sci Signal*. 2022;15(755). doi:10.1126/SCISIGNAL.ABO3507

111. Lazarski CA, Ford J, Katzman SD, Rosenberg AF, Fowell DJ. IL-4 attenuates Th1-associated chemokine expression and Th1 trafficking to inflamed tissues and limits pathogen clearance. *PLoS One*. 2013;8(8). doi:10.1371/JOURNAL.PONE.0071949

112. Haist M, Stege H, Grabbe S, Bros M. The Functional Crosstalk between Myeloid-Derived Suppressor Cells and Regulatory T Cells within the Immunosuppressive Tumor Microenvironment. *Cancers (Basel)*. 2021;13(2):1-34. doi:10.3390/CANCERS13020210

113. Cedrés S, Torrejon D, Martínez A, et al. Neutrophil to lymphocyte ratio (NLR) as an indicator of poor prognosis in stage IV non-small cell lung cancer. *Clin Transl Oncol*. 2012;14(11):864-869. doi:10.1007/S12094-012-0872-5

114. Bowen RC, Little NAB, Harmer JR, et al. Neutrophil-to-lymphocyte ratio as prognostic indicator in gastrointestinal cancers: a systematic review and meta-analysis. *Oncotarget*. 2017;8(19):32171-32189. doi:10.18632/ONCOTARGET.16291

115. Williams D, Hargrove-Wiley E, Bindeman W, et al. Type II Interleukin-4 Receptor Activation in Basal Breast Cancer Cells Promotes Tumor Progression via Metabolic and Epigenetic Modulation. *Int J Mol Sci*. 2024;25(9). doi:10.3390/IJMS25094647

116. Prokopchuk O, Liu Y, Henne-Bruns D, Kornmann M. Interleukin-4 enhances proliferation of human pancreatic cancer cells: evidence for autocrine and paracrine actions. *Br J Cancer*. 2005;92(5):921-928. doi:10.1038/SJ.BJC.6602416

117. Mollaoglu G, Tepper A, Falcomatà C, et al. Ovarian cancer-derived IL-4 promotes immunotherapy resistance. *Cell*. 2024;187(26):7492-7510.e22. doi:10.1016/j.cell.2024.10.006

118. Boutilier AJ, Elsawa SF. Macrophage Polarization States in the Tumor Microenvironment. *Int J Mol Sci*. 2021;22(13). doi:10.3390/IJMS22136995

119. Rodriguez PC, Ernstoff MS, Hernandez C, et al. Arginase I-producing myeloid-derived suppressor cells in renal cell carcinoma are a subpopulation of activated granulocytes. *Cancer Res*. 2009;69(4):1553-1560. doi:10.1158/0008-5472.CAN-08-1921

120. Hu C, Zhen Y, Ma Z, et al. Polyamines from myeloid-derived suppressor cells promote Th17 polarization and disease progression. *Molecular Therapy*. 2023;31(2):569-584. doi:10.1016/j.ymthe.2022.10.013

121. Oyabu M, Sato T, Kawaguchi R, et al. Multi-dimensional metabolomic remodeling under diverse muscle atrophic stimuli in vivo. *Cell Rep*. 2025;44(8). doi:10.1016/j.celrep.2025.116097

122. Ruggieri V, Scaricamazza S, Bracaglia A, et al. Polyamine metabolism dysregulation contributes to muscle fiber vulnerability in ALS. *Cell Rep*. 2025;44(1). doi:10.1016/j.celrep.2024.115123

123. Kunzke T, Buck A, Prade VM, et al. Derangements of amino acids in cachectic skeletal muscle are caused by mitochondrial dysfunction. *J Cachexia Sarcopenia Muscle*. 2020;11(1):226-240. doi:10.1002/JCSM.12498

124. Mund C, Sinha A, Aderhold A, et al. A key role of polyamine metabolism in adipose tissue homeostasis that regulates obesity. *Metabolism*. 2025;172. doi:10.1016/j.metabol.2025.156358

125. Wei LH, Yang Y, Wu G, Ignarro LJ. IL-4 and IL-13 upregulate ornithine decarboxylase expression by PI3K and MAP kinase pathways in vascular smooth muscle cells. *Am J Physiol Cell Physiol*. 2008;294(5):1198-1205. doi:10.1152/AJPCELL.00325.2007

126. Van den Bossche J, Lamers WH, Koehler ES, et al. Pivotal Advance: Arginase-1-independent polyamine production stimulates the expression of IL-4-induced alternatively activated macrophage markers while inhibiting LPS-induced expression of inflammatory genes. *J Leukoc Biol*. 2012;91(5):685-699. doi:10.1189/JLB.0911453

127. Seo SK, Kwon B. Immune regulation through tryptophan metabolism. *Exp Mol Med*. 2023;55(7):1371-1379. doi:10.1038/S12276-023-01028-7

128. Aoki R, Aoki-Yoshida A, Suzuki C, Takayama Y. Indole-3-Pyruvic Acid, an Aryl Hydrocarbon Receptor Activator, Suppresses Experimental Colitis in Mice. *J Immunol*. 2018;201(12):3683-3693. doi:10.4049/JIMMUNOL.1701734

129. Quintana FJ, Basso AS, Iglesias AH, et al. Control of T(reg) and T(H)17 cell differentiation by the aryl hydrocarbon receptor. *Nature*. 2008;453(7191):65-71. doi:10.1038/NATURE06880

130. Vyhlídalová B, Krasulová K, Pečinková P, et al. Gut Microbial Catabolites of Tryptophan Are Ligands and Agonists of the Aryl Hydrocarbon Receptor: A Detailed Characterization. *Int J Mol Sci*. 2020;21(7). doi:10.3390/IJMS21072614

131. Venkateswaran N, Garcia R, Lafita-Navarro MC, et al. Tryptophan fuels MYC-dependent liver tumorigenesis through indole 3-pyruvate synthesis. *Nat Commun*. 2024;15(1). doi:10.1038/S41467-024-47868-3

132. Molinier-Frenkel V, Prévost-Blondel A, Castellano F. The IL4I1 Enzyme: A New Player in the Immunosuppressive Tumor Microenvironment. *Cells*. 2019;8(7). doi:10.3390/CELLS8070757

133. Shen R, Ding Y, Dong Q, et al. IL-4-Induced Gene 1: A Potential Player in Myocardial Infarction. *Rev Cardiovasc Med*. 2024;25(9). doi:10.31083/J.RCM2509337

134. Zuo M, Fang J, Huang P, et al. IL4I1-catalyzed tryptophan metabolites mediate the anti-inflammatory function of cytokine-primed human muscle stem cells. *Cell Death Discov*. 2023;9(1). doi:10.1038/S41420-023-01568-X

135. Chi H. Sphingosine-1-phosphate and immune regulation: Trafficking and beyond. *Trends Pharmacol Sci*. 2011;32(1):16-24. doi:10.1016/j.tips.2010.11.002

136. Bernacchioni C, Ghini V, Squecco R, et al. Role of Sphingosine 1-Phosphate Signalling Axis in Muscle Atrophy Induced by TNFα in C2C12 Myotubes. *Int J Mol Sci*. 2021;22(3):1-19. doi:10.3390/IJMS22031280

137. Obinata H, Hla T. Sphingosine 1-phosphate and inflammation. *Int Immunol*. 2019;31(9):617-625. doi:10.1093/INTIMM/DXZ037

138. Jaigirdar SA, Benson RA, Elmesmari A, et al. Sphingosine-1-Phosphate Promotes the Persistence of Activated CD4 T Cells in Inflamed Sites. *Front Immunol*. 2017;8(NOV). doi:10.3389/FIMMU.2017.01627

139. Wu W, Zhang L, Chen Y, Huang C, Yang L, Lin D. Exercise Attenuates Skeletal Muscle Atrophy in Senescent SAMP8 Mice: Metabolic Insights from NMR-Based Metabolomics. *Molecules*. 2025;30(9). doi:10.3390/MOLECULES30092003

140. Holeček M, Vodeničarovová M. Muscle wasting and branched-chain amino acid, alpha-ketoglutarate, and ATP depletion in a rat model of liver cirrhosis. *Int J Exp Pathol*. 2018;99(6):274-281. doi:10.1111/IEP.12299

141. Zhang H, Qi G, Wang K, et al. Oxidative stress: Roles in skeletal muscle atrophy. *Biochem Pharmacol*. 2023;214. doi:10.1016/j.bcp.2023.115664

142. Delfinis LJ, Bellissimo CA, Gandhi S, et al. Muscle weakness precedes atrophy during cancer cachexia and is linked to muscle-specific mitochondrial stress. *JCI Insight*. 2022;7(24). doi:10.1172/JCI.INSIGHT.155147

143. Guan K, Liu X, Liu R, et al. Targeted energy metabolomics analysis-based mitochondrial restoration: Nutritional intervention of dairy-derived MFG-E8 synergistic with egg yolk phosphatidylcholine in skeletal muscle regeneration. *Int J Biol Macromol*. 2025;323(Pt 2). doi:10.1016/j.ijbiomac.2025.147215

144. Lundahl MLE, Mitermite M, Ryan DG, et al. Macrophage innate training induced by IL-4 and IL-13 activation enhances OXPHOS driven anti-mycobacterial responses. *Elife*. 2022;11. doi:10.7554/ELIFE.74690

145. Maiti AK, Sharba S, Navabi N, Forsman H, Fernandez HR, Linden SK. IL-4 Protects the Mitochondria Against TNFα and IFNγ Induced Insult During Clearance of Infection with Citrobacter rodentium and Escherichia coli. *Sci Rep*. 2015;5. doi:10.1038/SREP15434

146. Lin SY, Yang CP, Wang YY, et al. Interleukin-4 Improves Metabolic Abnormalities in Leptin-Deficient and High-Fat Diet Mice. *Int J Mol Sci*. 2020;21(12):1-19. doi:10.3390/IJMS21124451

147. Chang YH, Ho KT, Lu SH, Huang CN, Shiau MY. Regulation of glucose/lipid metabolism and insulin sensitivity by interleukin-4. *International Journal of Obesity 2012 36:7*. 2011;36(7):993-998. doi:10.1038/ijo.2011.168

148. van der Stel W, Yang H, le Dévédec SE, van de Water B, Beltman JB, Danen EHJ. High-content high-throughput imaging reveals distinct connections between mitochondrial morphology and functionality for OXPHOS complex I, III, and V inhibitors. *Cell Biol Toxicol*. 2023;39(2):415-433. doi:10.1007/S10565-022-09712-6

149. Zhao W, Kelly AC, Luna-Ramirez RI, Bidwell CA, Anderson MJ, Limesand SW. Decreased Pyruvate but Not Fatty Acid Driven Mitochondrial Respiration in Skeletal Muscle of Growth Restricted Fetal Sheep. *Int J Mol Sci*. 2023;24(21). doi:10.3390/IJMS242115760

150. Morigny P, Zuber J, Haid M, et al. High levels of modified ceramides are a defining feature of murine and human cancer cachexia. *J Cachexia Sarcopenia Muscle*. 2020;11(6):1459-1475. doi:10.1002/JCSM.12626

151. Lima TI, Laurila PP, Wohlwend M, et al. Inhibiting de novo ceramide synthesis restores mitochondrial and protein homeostasis in muscle aging. *Sci Transl Med*. 2023;15(696). doi:10.1126/SCITRANSLMED.ADE6509

152. Laurila PP, Wohlwend M, Imamura de Lima T, et al. Sphingolipids accumulate in aged muscle, and their reduction counteracts sarcopenia. *Nat Aging*. 2022;2(12):1159-1175. doi:10.1038/S43587-022-00309-6

153. Niwa S, Urtz N, Baumruker T, Billich A, Bornancin F. Ovalbumin-induced plasma interleukin-4 levels are reduced in ceramide kinase-deficient DO11.10 RAG1-/- mice. *Lipids Health Dis*. 2010;9. doi:10.1186/1476-511X-9-1

154. Mebarek S, Komati H, Naro F, et al. Inhibition of de novo ceramide synthesis upregulates phospholipase D and enhances myogenic differentiation. *J Cell Sci*. 2007;120(Pt 3):407-416. doi:10.1242/JCS.03331

155. Tan-Chen S, Guitton J, Bourron O, Le Stunff H, Hajduch E. Sphingolipid Metabolism and Signaling in Skeletal Muscle: From Physiology to Physiopathology. *Front Endocrinol (Lausanne)*. 2020;11. doi:10.3389/FENDO.2020.00491

156. Middel V, Zhou L, Takamiya M, et al. Dysferlin-mediated phosphatidylserine sorting engages macrophages in sarcolemma repair. *Nat Commun*. 2016;7. doi:10.1038/NCOMMS12875

157. Selathurai A, Kowalski GM, Mason SA, et al. Phosphatidylserine decarboxylase is critical for the maintenance of skeletal muscle mitochondrial integrity and muscle mass. *Mol Metab*. 2019;27:33-46. doi:10.1016/j.molmet.2019.06.020

158. Taha TA, Mullen TD, Obeid LM. A house divided: Ceramide, sphingosine, and sphingosine-1-phosphate in programmed cell death. *Biochim Biophys Acta Biomembr*. 2006;1758(12):2027-2036. doi:10.1016/j.bbamem.2006.10.018

159. Aiyar N, Disa J, Ao Z, et al. Lysophosphatidylcholine induces inflammatory activation of human coronary artery smooth muscle cells. *Mol Cell Biochem*. 2007;295(1-2):113-120. doi:10.1007/S11010-006-9280-X

160. Montero-Bullon JF, Melo T, Ferreira R, et al. Exercise training counteracts urothelial carcinoma-induced alterations in skeletal muscle mitochondria phospholipidome in an animal model. *Sci Rep*. 2019;9(1). doi:10.1038/S41598-019-49010-6

161. Rohm M, Zeigerer A, Machado J, Herzig S. Energy metabolism in cachexia. *EMBO Rep*. 2019;20(4). doi:10.15252/EMBR.201847258

162. Petruzzelli M, Wagner EF. Mechanisms of metabolic dysfunction in cancer-associated cachexia. *Genes Dev*. 2016;30(5):489-501. doi:10.1101/GAD.276733.115

163. Hoene M, Li J, Li Y, et al. Muscle and liver-specific alterations in lipid and acylcarnitine metabolism after a single bout of exercise in mice. *Sci Rep*. 2016;6. doi:10.1038/SREP22218

164. Hernández-Saavedra D, Hinkley JM, Baer LA, et al. Chronic exercise improves hepatic acylcarnitine handling. *iScience*. 2024;27(3). doi:10.1016/j.isci.2024.109083

165. Chen Z, Qin X, Zhang X, Liu B, Chen M. Upregulation of IL-4 signaling contributes to aerobic exercise-induced insulin sensitivity. *Biochem Biophys Res Commun*. 2020;525(3):662-667. doi:10.1016/j.bbrc.2020.02.103

166. Della Gatta PA, Garnham AP, Peake JM, Cameron-Smith D. Effect of exercise training on skeletal muscle cytokine expression in the elderly. *Brain Behav Immun*. 2014;39:80-86. doi:10.1016/j.bbi.2014.01.006

167. Samadian Z, Samadian L, Arabzadeh E. Exercise training enhances myokine release and reduces brain insulin resistance: insights into muscle-CNS metabolic cross-talk. *Metab Brain Dis*. 2025;40(7). doi:10.1007/S11011-025-01710-X

168. Chang YH, Tsai JN, Chen TL, et al. Interleukin-4 Promotes Myogenesis and Boosts Myocyte Insulin Efficacy. *Mediators Inflamm*. 2019;2019. doi:10.1155/2019/4182015